Hybrid energy harvesting towards a sustainable energy system

Yuljae Cho

Exeter College, University of Oxford

A thesis submitted in fulfilment of requirement for the degree of

DPhil in Engineering Science at the University of Oxford

Trinity Term 2017

Hybrid energy harvesting towards a sustainable energy system

Yuljae Cho, Exeter College, University of Oxford

Abstract

Soaring energy demands are inevitable because of the continual increase in the global population as well as the greater reliance on electronic technologies. Current energy generation systems are highly dependent upon fossil fuels, for which the imminent risks and limitations are well known. First of all, we are confronting an energy crisis due to the depletion of these fossil fuels. However, current sustainable and renewable energy sources are not in a position to fully replace them as of yet. In fact, less than 10% of energy that is generated is from renewable energy sources, such as from hydroelectric power and solar power. Secondly, the emission of carbon dioxide (CO_2) and greenhouse gases (GhGs) from fossil fuels is currently at a serious level. As a result, today we are facing and experiencing abnormal climate changes.

In order to mitigate and potentially resolve the energy crisis, energy generation systems are now shifting from fossil fuels to sustainable and renewable energy sources. Developments in energy harvesting technologies are considered to be a practical and promising way to deal with this crisis. Energy harvesting is a process that involves the generation of electrical energy by harnessing ambient environmental energy that is otherwise wasted. Generally, energy harvesting refers to a small amount of power for technologies such as portable electronic devices and wireless sensor networks. However, going forward, energy harvesting technologies beyond these would enable a bottom-up approach from ‘the cell’ scale to ‘a large farm’ scale.

My DPhil thesis deals with energy harvesting technologies that involve harnessing different environmental energy sources, such as solar and mechanical energy, using quantum dots for solar cells and polyvinylidene fluoride (PVDF)-based polymers for mechanical energy harvesting applications. Via novel approaches, such as the fabrication of a multi-junction quantum dot solar cell (QDSC) and the development of a room temperature polymer crystallisation method (solvent annealing), a significant enhancement in energy harvesting performance has been achieved. In addition, I have demonstrated more advanced energy harvesting devices by combining two alternative technologies together. Initially, a high efficiency QDSC is presented using the ferroelectric and piezoelectric coupling effect in PVDF-based polymer. Secondly, the integration of a QDSC with a mechanical energy harvester is demonstrated, which showed a combined enhancement by generating higher power beyond that observed from the individual components. Lastly, the thesis concludes with a demonstration of an application of these hybrid devices to self-powered electronics, which shows promise for future sustainable energy systems using energy harvesting technology.

“He who has dreamed for long resembles his dream”

Andre Malraux

Acknowledgements

I would like to thank my supervisors, Dr. Junginn Sohn, Prof. Stephen M. Morris, Prof. SeungNam Cha, and Prof. Jong Min Kim, for their unwavering patience, guidance and support. This work could not have been completed without their enthusiasm and support. I also thank them for the exceptional work atmosphere they have fostered in the group.

I would like to thank our current group members, Dr. Young-Woo Lee, Dr. A-Rang Jang, Dr. Bo Hou, Dr. Sanghyo Lee, John Hong, Paul Giraud, and Sangyeon Pak, as well as previous group members, Dr. Jong Bae Park, Dr. Byung-Sung Kim, and Prof. Tae-Lim Choi, for enjoyable discussions and invaluable advice about my work. In particular, I would like to thank Juwon Lee for going through hardships together with me during our DPhil studies and Dr. Hyunchae Chun for helping me from before arriving in Oxford to throughout the DPhil course. Thank you also to Dr. Jongchul Lim, Dr. Sungho Nam, Prof. Henry J. Snaith, and Prof. Jae Eun Jang for their help with the material analysis and device-related work.

In addition, I would like thank Exeter College for the additional funding to allow me to present my work at international conferences. I also thank the Department of Engineering Science for accepting me on to the program and providing me with this great opportunity.

Finally, I would like to thank my parents, Hyun Choon Cho, Namsook Cho, my sister, A Jin Cho, and above all else my fiance, Xi Liu. Without your love, support, and belief in me, I would never have been able to pursue all of the incredible opportunities that life has offered so far.

Table of Contents

List of Tables

List of Figures

List of Abbreviations

AM: Air mass

EBL: Electron blocking layer

EDT: 1,2-ethanedithiol

EQE: External quantum efficiency

ETL: Electron transport layer

FF: Fill factor

IEH: Integrated energy harvester

IoT: Internet of things

MEG: Multiple exciton generation

MEH: Mechanical energy harvester

NIR: Near-infrared

OA: Oleic acid

PCE: Power conversion efficiency

P(VDF-TrFE): Poly(vinylidenefluoride-trifluoroethylene)

P(VDF-TrFE-CTFE): Poly(vinylidenefluoride-trifluoroethylene-chlorotrifluoroethylene)

QD: Quantum dot

QDSC: Quantum dot solar cell

SA: Solvent annealing

SCLS: Space charge-limited current

SEG: SA-treated energy generator

TA: Thermal annealing

TBAI: Tetrabutylammonium iodide

TEG: TA-treated energy generator

ZnO: Zinc Oxide

Publications

1. **Yuljae Cho**, Jong Bae Park, Byung-Sung Kim, Juwon Lee, Woong-Ki Hong, Il-Kyu Park, Jae Eun Jang, Jung Inn Sohn, SeungNam Cha, and Jong Min Kim, "*Enhanced energy harvesting based on surface morphology engineering of P(VDF-TrFE) film*", ***Nano Energy*** (2015) 16, 524-532.

2. **Yuljae Cho**, Docheon Ahn, Jong Bae Park, Sangyeon Pak, Sanghyo Lee, Byoung Ok Jun, John Hong, Su Yong Lee, Jae Eun Jang, Jinpyo Hong, Stephen M. Morris, Jung Inn Sohn, SeungNam Cha, and Jong Min Kim, "*Enhanced ferroelectric property of P(VDF-TrFE-CTFE) film using room temperature crystallization for high performance ferroelectric device applications*", ***Advanced Electronic Materials*** (2016), 2, 1600225 ***(Front Cover)***.

3. **Yuljae Cho**, Paul Giraud, Bo Hou, Young-Woo Lee, John Hong, Sanghyo Lee, Sangyeon Pak, Juwon Lee, Jae Eun Jang, Stephen M. Morris, Jung Inn Sohn, SeungNam Cha, and Jong Min Kim, "*Charge Transport Modulation of a Flexible Quantum Dot Solar Cell using a Piezoelectric Effect*", ***Advanced Energy Materials*** (2018), 8, 1700809 ***(Inside Front Cover)***.

4. **Yuljae Cho**, Bo Hou, Jongchul Lim, Sanghyo Lee, Sangyeon Pak, John Hong, Paul Giraud, A-Rang Jang, Young-Woo Lee, Juwon Lee, Jae Eun Jang, Henry J. Snaith, Stephen M. Morris, Jung Inn Sohn, SeungNam Cha, and Jong Min Kim, *"Balancing Charge Carrier Transport in a Quantum Dot P-N Junction toward Hysteresis-Free High Performance Solar Cells"*, ***ACS Energy Letters*** (2018) 3, 1036-1043.

5. Bo Hou, **Yuljae Cho**, Byung Sung Kim, John Hong, Jong Bae Park, Se Jin Ahn, Jung Inn Sohn, SeungNam Cha, and Jong Min Kim, "*Highly monodispersed PbS quantum dots for outstanding cascaded-junction solar cells*", ***ACS Energy Letters*** (2016), 1, 834–839.

6. Bo Hou, **Yuljae Cho**, Jong Bae Park, Docheon Ahn, Sanghyo Lee, Byung Sung Kim, John Hong, Stephen M. Morris, Jung Inn Sohn, SeungNam Cha and Jong Min Kim, "*Red Green Blue Emissive Lead Sulfide Quantum Dots: Heterogeneous Synthesis and Applications*", ***Journal of Material Chemistry C***, 5 (2017), 3692-3698 (***Back Cover***).

7. Byung-Sung Kim, Darren C. J. Neo, Bo Hou, Jong Bae Park, **Yuljae Cho**, Nanlin Zhang, John Hong, Sangyeon Pak, Sanghyo Lee, Jung Inn Sohn, Hazel E. Assender, Andrew A. R. Watt, SeungNam Cha, and Jong Min Kim "*High Performance PbS Quantum Dot/Graphene Hybrid Solar Cell with Efficient Charge Extraction*", ***ACS Applied Materials & Interfaces*** (2016), 8, 13902–13908.

8. Byung-Sung Kim, John Hong, Bo Hou, **Yuljae Cho**, Jung Inn Sohn, SeungNam Cha and Jong Min Kim, "*Inorganic-ligand exchanging time effect in PbS quantum dot solar cell*", ***Applied Physics Letters*** (2016) 109, 063901.

9. John Hong, Bo Hou, Jongchul Lim, Sangyeon Pak, Byung-Sung Kim, **Yuljae Cho**, Juwon Lee, Young-Woo Lee, Paul Giraud, Sanghyo Lee, Jong Bae Park, Stephen M. Morris, Henry J. Snaith, Jung Inn Sohn, SeungNam Cha, and Jong Min Kim, "*Enhanced charge carrier transport properties in colloidal quantum dots solar cells via organic and inorganic hybrid surface passivation*", ***Journal of Material Chemistry A*** (2016), 4, 18769–18775.

10. Young-Woo Lee, Geon-Hyoung An, Byung-Sung Kim, John Hong, Sangyeon Pak, Eun-Hwan Lee, **Yuljae Cho**, Juwon Lee, Paul Giraud, Seung Nam Cha, Hyo-Jin Ahn, Jung Inn Sohn, and Jong Min Kim "*Synergistic Effects of a Multi-Functional Graphene Based Interlayer on Electrochemical Behavior and Structural Stability*", ***ACS Applied Materials & Interfaces*** (2016), 8, 17651–17658.

11. Juwon Lee, Sangyeon Pak, Young-Woo Lee, **Yuljae Cho**, John Hong, Paul Giraud, Stephen M. Morris, Jung Inn Sohn, SeungNam Cha and Jong Min Kim, "*Monolayer*

optical memory cells based on artificial trap-mediated charge storage and release", ***Nature Communications*** 8 (2017), 14734.

12. Akbar I. Inamdara, Jongmin Kim, Yongcheol Jo, Hyeonseok Woo, Sangeun Cho, Sambhaji M. Pawar, **Yuljae Cho**, Bo Hou, SeungNam Cha, Jungwon Kwak, Hyungsang Kim, and Hyunsik Im, "*Highly Efficient Electro-optically Tunable Smart-supercapacitors Using an Oxygen-excess Nanograin Tungsten Oxide Thin Film*", ***Solar Energy Materials and Solar Cells*** (2017), 166, 78–85.

13. John Hong, Young-Woo Lee, Docheon Ahn, Sangyeon Pak, Juwon Lee, A-Rang Jang, Sang-Hyo Lee, Bo Hou, **Yuljae Cho**, Geon-Hyoung An, Stephen M. Morris, Hyo-Jin Ahn, Hyeon Suk Shin, SeungNam Cha, Jung Inn Sohn, and Jong Min Kim, "*Highly Stable 3D Porous Heterostructures with Hierarchically-Coordinated Octahedral Transition Metals for Enhanced Performance Supercapacitors*", ***Nano Energy*** (2017), 39, 337-345.

14. Juwon Lee, Sangyeon Pak, Paul Giraud, Young-Woo Lee, **Yuljae Cho**, John Hong, A-Rang Jang, Hee-Suk Chung, Hu Young Jeong, Hyun Suk Shin, Luigi G. Occhipinti, Stephen M. Morris, SeungNam Cha, Jung Inn Sohn, and Jong Min Kim "*Thermodynamically stable synthesis of large-scale and highly-crystalline transition metal dichalcogenide monolayers and their unipolar n-n heterojunction devices*", ***Advanced Materials*** (2017), 29, 1702206 (***Front Cover***).

15. Sangyeon Pak, Juwon Lee, Young-Woo Lee, A-Rang Jang, Seongjoon Ahn, Kyung Yeol Ma, **Yuljae Cho**, John Hong, Sanghyo Lee, Hu Young Jeong, Hyunsik Im, Hyeon Suk Shin, Stephen M. Morris, SeungNam Cha, Jung Inn Sohn, and Jong Min Kim, "*Strain-mediated interlayer coupling effects on the excitonic behaviors in an epitaxially-grown MoS2/WS2 van der Waals heterobilayer*", ***Nano Letters*** (2017), 17, 5634-5640.

Manuscripts in preparation/submitted

1. Toward sustainable sensor network system powered by all solution processable hybridized green energy harvester, *in preparation.*

1. Introduction

1.1 What is energy harvesting?

Electrical energy harvesting or energy scavenging, is an energy conversion process from ambient energy to an electrical form using a variety of phenomena, such as photovoltaic, piezoelectric, and thermoelectric effects as defined by the Institute of Physics (IOP).[1,2] Conventionally, energy harvesting technologies refer to the scavenging of power for small and independent electronic devices, such as portable electronic devices and wireless sensors, which is in contrast to large-scale renewable energy sources and technology. In addition, current energy harvesting technologies are expanding further from the cell scale to a larger farm scale due to growing interests in developing of sustainable global societies, which suggests that energy harvesting is becoming more important.[3-8]

1.2 Why energy harvesting?

1.2.1 Energy consumption and imminent risks

The world-wide energy consumption in 2012 was reported to be 549 quadrillion British thermal units (quad BTU), where 1 quad BTU corresponds to 293 TWh.[9] The tremendous amount of energy consumed is the result of many factors. Firstly, the global population has grown from 700 million people at the beginning of the industrial revolution to around 7 billion at present, which inevitably incurs a greater demand on energy consumption.[10] In addition, it is estimated that the world population will grow further to a value of 10 billion by 2100, which means that the constant demands on energy supply and consumption will continue to increase.[11] Secondly, the development of modern electronic equipment, such as house-hold appliances, equipment in factories, hospitals, and communication hubs, as well as portable electronic devices, has also

triggered a continual demand on energy both day and night, although it can be argued that modern electronics technologies enhance the quality of life of a human being.[12] Moreover, as we now live in an age of a smart-life, we are approaching a more and more electronics-dependent society, which will result in more prominent energy consumption than ever before. As a result, soaring energy demands will be inevitable in the future and we are thus now confronting imminent risks if we cannot shift from fossil fuel dependent energy systems to sustainable and renewable ones.

First of all, currently available sources for energy generation, in particular fossil fuels that account for 60 ~ 70% of the entire energy generation, are finite.[10] It is estimated that fossil fuels will last no more than 120 years as listed in Table 1.1.[13] In spite of the reassurance that other kinds of natural resources that can replace fossil fuels are currently being unearthed, such as flammable ice,[14] it is still disappointing that environmentally-abundant energy sources cannot meet our energy requirements. Specifically, approximately 4% or less, depending on the reports in the literature, of all the energy generated is from renewable energy sources, such as from hydroelectric and solar power.[10,15,16] Considering that locations that are suitable for hydroelectric power plants are limited and also building hydroelectric power plants is not readily compatible with the natural environment, the possibility of sustainable energy sources for replacing fossil fuels in the near future is still rather slim.[4,10]

Table 1.1: Estimated reserves of fossil fuels.

Fuel	Reserves	Years left
Oil	1,386 billion barrels	46.2
Gas	187.1 trillion cubic meters	58.6
Coal	860,938 million tons	118

Secondly, carbon dioxide (CO_2) and greenhouse gas (GhGs) emission are currently at the border of serious emission levels. In addition, the amount of environmentally-hazardous pollutants that result from burning fossil fuels, such as sulfuric oxides (SO_x), nitric oxide (NO_x), and particulate matters (PM), have risen significantly.[9] As a result, today we are facing and experiencing an unprecedented change in climate , for example extreme heat waves and torrential rainfalls. Because the Earth's climate is a complex system it is hard to predict future risks if the emission of CO_2 and GHGs continues at the current pace. However, it is understood that the reverse process of a climate change takes longer than the time it took to cause the change, due to the huge thermal inertia of the deep oceans.[17] This means that even if we can stop the emission of CO_2 and GHGs tomorrow, it might take several centuries to repair the damages caused and reach a new equilibrium.[9]

In 2015, the Paris climate agreement was signed by 195 countries worldwide (signatories: 195 and parties 160 countries), which is aimed at mitigating global warming by pursuing efforts to limit the increase in temperature.[18] The Paris agreement shows an awareness of the imminent risks that we are confronting now and the efforts worldwide to resolve them.

1.2.2 The status quo and the goal of an energy harvesting technology

A major goal of energy harvesting is the realisation of an independent and sustainable energy system, i.e. a battery-free system, for powering modern electronics, such as communications, personal health care, and environmental monitoring devices. Notably, there are two representative energy harvesting devices that are the most widely and actively researched; the photovoltaic cell (more commonly known as a solar cell), and a mechanical energy harvester.[2,19]

First of all, a solar cell is arguably a long-standing topic from the point of view of energy harvesting, which started in the late 19th century.[20] The solar power that is incident on the Earth is approximately 174,000 TW as reported by governmental institutions of the United States of America, whereas humans typically consume only a fraction of this power (15 TW).[3,8,21,22] In spite of the loss of solar energy due to atmospheric absorption and scattering, as well as regional dependency due to stochastic variations, such as climate effects, the average global solar irradiance is still approximately 200 Wm^{-2}, which makes solar power one of the most desirable renewable energy sources.[3,23,24] Hence, commercialised solar cells and also solar power stations have already been developed, which contributed 31 GW to the total power generated in 2012.[25]

Current commercialised solar cells and panels are based on expensive materials and complex fabrication processes and thus it is highly desirable to develop a process which is affordable and cost-effective for mass-production. In this regard, research on a 3rd generation of solar cell technology that be solution-processed and cost-effective is one of the goals of current solar cell research. Recently, a ground-breaking demonstration of 22.13 ± 0.69 % power conversion efficiency (PCE) using a solution process was reported.[26] Also, it is noteworthy that the author reported a PCE of 19.7% for a large-scale device (~ 1 cm^2) with high stability, maintaining 90% of its original performances for up to 400 days, which showed considerable promise for future high power and stable solar panel using 3rd generation solar cells.[26] Progress in the solar cell area is summarised in Figure 1.1 which was obtained from the National Renewable Energy Laboratory (NREL) database.[27] Also, the performances of quantum dot solar cells (QDSCs) that have previously broken the world record are illustrated in Table 1.2. It is worth noting

that although the best research cells show high efficiencies in the research lab scale, there might be scaling-up issues, which results in a decrease in the solar cell performance. The decrease in performance mainly results from uniformity and defects of films over a large scale as well as an edge effect. This latter exhibits a higher efficiency than its real efficiency, which becomes stronger in a small-scale cell. In addition, due to growing interest in smart building management, harvesting indoor light has also attracted enormous interest recently.[28,29]

Table 1.2. Summary of best research-based quantum dot solar cell efficiencies reported in Figure 1.1.

References	V_{OC} (V)	I_{SC} (A)	FF	PCE (%)	Active Area (cm^2)
Nat. Nanotechnol. 7, 577–582 **(2012)**	0.6050 ± 0.071	0.00091 ± 0.00001	58.0 ± 2.1	7.0 ± 0.2	0.0453 ± 0.0001
Nat. Mater. 13, 796–801 **(2014)**	0.5546 ± 0.0055	0.00033 ± 0.00001	63.8 ± 1.3	8.55 ± 0.18	0.0137 ± 0.0000
Adv. Mater. 28, 299–304 **(2016)**	0.6353 ± 0.0063	0.001039 ± 0.000019	71.9 ± 1.5	9.88 0.21	0.0481 ± 0.0001
Nano Lett. 16, 4630–4634 **(2016)**	0.6119 ± 0.0085	0.001173 ± 0.000021	71.2 ± 1.1	10.59 ± 0.23	0.0483 ± 0.0001
Nat. Mater. 16, 258–263 **(2017)**	0.6113 ± 0.0085	0.001356 ± 0.000025	67.8 ± 1	11.28 ± 0.25	0.0498 ± 0.0002

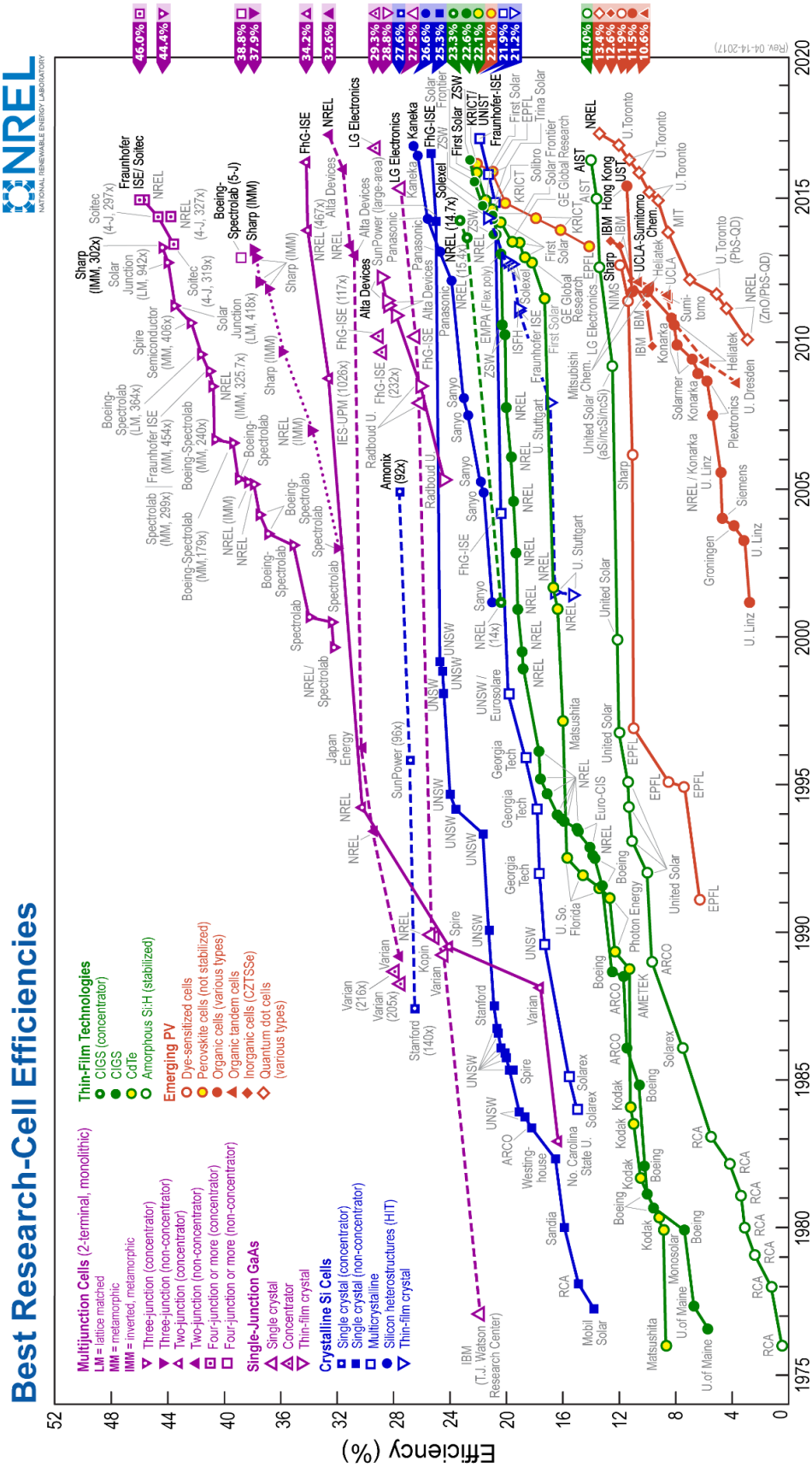

Figure 1.1: Best Research-Cell efficiencies that were presented by NREL on 14th Sept. 2017.[23]

Secondly, a mechanical energy harvester using piezoelectric, ferroelectric, and triboelectric effects has also attracted interest since mechanical energy sources are abundant in a variety of different forms. In contrast to solar energy, mechanical energy sources are not dependent on the region, climate, time, and seasons, which enables the generation and provision of a stable power supply to devices. Various types of mechanical energy harvesting devices have been demonstrated depending upon the desired application, such as wearable, flexible, implantable medical devices.[30-33] In addition, we are approaching an era of smart-life where internet of things (IoT), which autonomously performs sensing and communication with one another, is an indispensable technology. In this regard, the development of self-powered sensors and sensor networks by using energy harvesting devices is of particular importance in realizing IoT technology. Up to now, energy harvesting devices using a triboelectric effect have shown power densities as large as 500 Wm^{-2}, and an instantaneous conversion efficiency of ~ 70%, which suggests that the realisation of sustainable power sources or self-powered electronics is not too far away in the distant future.[34]

Due to the intermittence of environmental energy sources, which is typically beyond our control, there are still concerns about the realisation of a battery-free system or sustainable power source using only one type of energy harvesting devices. Moreover, energy harvesters typically show a stark contrast in the current and voltages that are generated. For example, a high current but low voltage from a solar cell whereas low current, but high voltage from a mechanical energy harvester, which makes it hard to meet the required power for a device using either one of these energy harvesters on their own.[32,35,36] In this regard, the development of hybridised energy harvesters to overcome the limits of individual harvesters and, in turn, realise a sustainable power source would

be highly desirable.[36-42] Therefore, all-in-one energy harvesting and storage devices have been introduced, such as the integration of a solar cell with a mechanical energy harvester, a pyroelectric energy harvester with a mechanical energy harvester, and even a mechanical energy harvester with a storage device.[39-44]

Lastly, energy harvesting technologies, which conventionally refers to the generation of small amounts of power for low-power electronics, are expanding towards further scaling up energy generation.[3-8] A typical example is a photovoltaic panel for a streetlight or a household, which we often see in our daily life. Not just solar power but also the oceans are considered to be a huge medium for energy generation. Recently, harnessing energy from the ocean, such as tidal energy, has been proposed for larger-scale energy generation using a mechanical energy harvester.[4,5]

1.3 Aim of the Thesis

Current energy harvesting technology has been mainly focused on the realisation of an energy harvester than can harvest only one kind of energy source, specifically, solar or mechanical energy. In spite of significant progress made in individual energy harvesting performances, there still remain a number of challenges in the development of energy harvesting devices. First of all, how do we further enhance the performance of a device so that the device can be widely used in practical applications. Secondly, how might we combine two different physical effects so as to enhance the overall performance. Finally, how might we improve the reliability and stability of an energy harvesting device so that it provides a constant power output even in the presence of an intermittent environmental energy source.

In the thesis, I attempt to provide some answers to these questions and consider the tasks that have to be resolved for moving current energy harvesting technologies to be used in practical applications.

1.4 Layout of the Thesis

In light of the future risks to energy supply and research efforts to mitigate global energy issues, which have motivated me, my DPhil thesis deals with energy harvesting technologies by harnessing environmental energy sources, such as photons and mechanical vibrations.

To begin with, a research on individual energy harvesting devices was explored to improve their performance by employing novel and functional quantum dots for application in solar cells in Chapter 2. By developing a novel approach, such as the unique structure of a multi-junction quantum dot solar cell (QDSC), an enhancement of the power conversion efficiency (PCE) was demonstrated in the solar cell. Following this, a research on current 'cell' scale energy harvesting technologies was further expanded to explore large scale energy generation. From the simulation studies, it was demonstrated that cell-scale research can be applied to larger scale energy generation systems, which suggests that energy harvesting technologies could be suitable as a sustainable power source for not only low power electronics but also large-scale power generation.

In Chapter 3, the study on polyvinylidene fluoride (PVDF)-based polymers are studied for an application in a mechanical energy harvester. Via a room temperature polymer crystallisation method (solvent annealing), a significant enhancement in the energy harvesting performance in a mechanical energy harvesting device was achieved.

The mechanical energy harvester was then used to demonstrate the generation of an optical signal using light emitting diodes by harnessing mechanical vibrations.

Studies on the basic mechanism of individual energy harvesting devices were then applied so as to fabricate more advanced energy harvesting devices. To begin with, a high efficiency QDSC using the ferroelectric and piezoelectric effect in a PVDF-based polymer is presented in Chapter 4. This is followed by the integration of a QDSC with a mechanical energy harvester so as to realise an all-in-one energy harvesting device in Chapter 5. Both hybridised energy harvesters showed significant improvements when combined into a single device. In addition, an application to self-powered electronics, such as an infrared (IR) motion sensor so as to realise IoT technology in the future, was demonstrated by using a hybridised energy harvester, which is particularly promising for future sustainable energy systems using energy harvesting technology. Further, it could also be applied to larger scale energy generation requirements in the future, which may help to contribute to the resolution of the energy crisis and the imminent risks that we are confronting in terms of the supply and demand of energy.

2. Solar energy

2.1 Introduction

2.1.1 Photovoltaic effect and the solar cell

Research on the photovoltaic effect dates back to the early 19th century, which was discovered by the French physicist, Alexandre Edmond Becquerel. Using this effect, the first solar cell was invented by Charles Fritts in 1883 and then a half of a century later, Bell Labs produced the first commercialised solar cell using silicon (Si) in 1954.[20,45,46] Presently, it is becoming more and more important to develop sustainable energy systems. There are currently lots of different materials for solar cell applications, such as bulk Si (used in the first generation of a solar cell), thin-film cadmium telluride (CdTe) (for the second generation of a solar cell), and polymers, nanocrystals (quantum dots) and so on (for the third generation of a solar cell). Although solar cells can be loosely categorised into three different generations, all solar cells employ a p-n junction as the fundamental structure used to generate and dissociate excitons by absorbing incident photons.

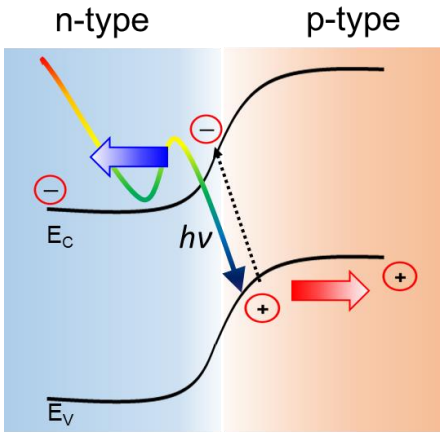

Figure 2.1: A p-n junction band diagram and an illustration of the photovoltaic effect. E_c and E_v refer to conduction band and valence band energy levels of both n- and p-type materials.

As shown in Figure 2.1, incident light generates an electron-hole pair, i.e. an exciton, via the photovoltaic effect.[47,48] The generated electron-hole pair then needs to be collected at each electrode to generate photocurrent. As a result, an electric field is required to dissociate the electron-hole pair. By forming a p-n junction using n-type and p-type semiconducting photo-active materials, a space charge region is formed where an internal electric field is induced. The induced field dissociates the generated excitons prior to recombination so that each negative and positive charge can be transported and collected at each electrode. Consequently, the key factors for attaining a high efficiency solar cell are associated with the formation of a p-n junction and its properties, such as the energy difference between the n- and p-type material, the exciton lifetime, and mobility.

As explained above, the photo-generated electron and hole (dissociated exciton) upon light excitation are collected at the electrodes, which results in the generation of a current flow. Current (I) generated by a solar cell can be described by the following equation, where I_s is the dark saturation current, and V_a and V_t indicate the applied bias and the thermal voltage (typically kT/q), respectively.[48]

$$I = I_s\left(e^{V_a/V_t} - 1\right) - I_{ph} \tag{2.1}$$

At zero voltage bias, the current I is equal to I_{ph}, which means the generated current in a solar cell results from only the photo-generated charges and the current I is called the short circuit current (I_{sc}). In contrast, the open circuit voltage of a solar cell occurs when the current is zero. Using equation 2.1, an equation for V_{oc} of a solar cell can be derived.[48]

$$\begin{cases} \mathrm{I} = 0 \text{ and thus } I_S\left(e^{V_a/V_t} - 1\right) - I_{ph} = 0 \\ V_a = V_t \ln\left(\frac{I_{ph}}{I_s} + 1\right) = V_{oc} \end{cases} \tag{2.2}$$

It is worth noting that the maximum V_{oc} that can be attained is dependent on the electronic bandgap of the photo-active material and is determined by the potential difference between the quasi-Fermi levels, E_{fn} and E_{fp}. Also, the output power of a solar cell can be calculated from the product of the current and voltage as given in the following equation (2.3).[48]

$$P = I \times V_a = I_s V_a \left(e^{v_a/v_t} - 1\right) - I_{ph} V_a \qquad .3)$$

The first-order differential of the output power with respect to the applied voltage (V_a) provides an expression for the maximum power (P_{max}) that can be delivered by a solar cell. We can then obtain the current and voltage at the maximum point, which are denoted as I_{mpp} and V_{mpp}, respectively. The fill factor (FF) gives information about the ratio between the maximum power and the theoretical power ($P_t = I_{sc} \times V_{oc}$), which determines the power conversion efficiency (PCE) of a solar cell. As shown in Figure 2.2, a high fill factor can lead to higher power as the maximum power increases (2.4).

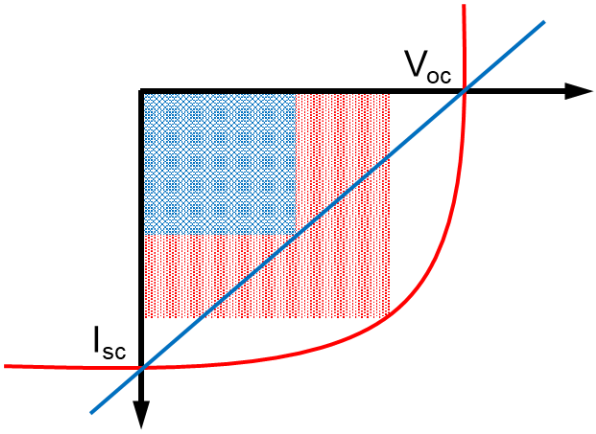

Figure 2.2: An illustration of high (Red) and low (Blue) FF for the same I_{sc} and V_{oc} conditions, which indicates that the FF is one of the performance-determining factors.[48]

$$FF = \frac{P_{max}}{P_t} = \frac{I_{max} V_{max}}{I_{sc} V_{oc}} \qquad (2.4)$$

Finally, the PCE of a solar cell can be determined by using the parameters that we obtained above where P_{in} is the incident light power (2.5).[48]

$$\mathrm{PCE} = \frac{P_{out}}{P_{in}} = FF\,\frac{I_{sc}V_{oc}}{P_{in}} \tag{2.5}$$

According to this equation, I_{sc}, V_{oc} and FF are parameters that can be controlled experimentally so as to maximise the PCE of a solar cell as the input power is fixed by the Air Mass (AM) 1.5G, i.e. 1 sun, (100 mWcm^{-2}). As the parameters are not independent of each other, but rather exhibit a trade-off relationship (I_{sc}↔V_{oc}), this makes it hard to attain a high efficiency solar cell. Because every material has its own merits as a solar cell application, I will deal only with quantum dots as one of the promising solar cell materials with respect to maximising I_{sc}, V_{oc} and FF.

2.1.2 Quantum dots as a solar cell material

Quantum dots (QDs) have attracted great interest as solar cell materials due to their fascinating properties such as quantum confinement, bandgap tuning and multiple exciton generation (MEG). Details on the physical properties of QDs will be discussed in the following section. In this section, I will focus on the merits of QDs as a solar cell material with respect to properties such as I_{sc}, V_{oc}, and FF.

First, QDs are known to have a large absorption coefficient for light, which is beneficial for enhancing the I_{sc} of a solar cell.[49,50] Fundamentally, a solar cell converts photon energy into an electrical form by absorbing sun-light and thus light absorption is an essential requirement in the generation of electrons and holes. This means that the high absorption coefficient of QDs makes them viable for generating high photocurrent, and thus current densities of more than 30 mAcm^{-2} have been reported.[51,52] In addition, due to the tunability of the bandgaps, QDs with a variety of bandgaps can be readily synthesised. By forming a multi-junction using QDs of different sizes, it is possible to absorb a wider portion of the solar spectrum so as to generate more excitons. Moreover,

an MEG was also observed in QDs with a small bandgap. An absorption of photons with high energy can generate more than two excitons, which can also contribute to the generation of large photocurrent in a solar cell system.[53,54]

Theoretically, the maximum attainable V_{oc} is dependent on the bandgap of the material and thus ideally a higher bandgap generates a larger V_{oc} in the solar cell system. Due to the effect of quantum confinement, the bandgap of QDs increases as the size of the QDs decreases, which results in a facile tuning of the bandgap. Using this phenomenon, the V_{oc} of a solar cell can also be readily modified so as to attain a high PCE.[55-57] A high surface to volume ratio of QDs makes them easy to react with many different kinds of ligands that have high mobility with less defects. Up to now, the highest FF reported using QDs is approaching 70%, which is comparable to other promising 3rd generation solar cell materials.[58,59]

2.1.3 Current Challenges

Quantum dot solar cells (QDSC) have been intensively researched for the past decade and have shown rapid progress in terms of improvements from less than 1% to more than 10% PCE recently, which is comparable to that of their organic counterparts.[60-62] However, the PCE of a QDSC is still below the theoretical value, known as the Shockley-Queisser limit.[63] This largely stems from two factors; one being material-related and the other being related to the device architecture.[64] For example, the synthesis of monodispersed QDs is of prime importance. Because QDs are extremely small, a non-uniform size distribution can result in a large number of defects sites and also a potential drop due to the non-uniform interdot distance and the formation of voids. In addition, a poor junction structure causes severe charge loss by forming a Schottky contact and

consequently an energy barrier. Judicious structural designs, such as a quantum junction and an inverted structure have been introduced and a significant enhancement in the solar cell performance has been observed.[65-67] However, these structures are not able to fully exploit the remarkable properties of QDs as solar cell materials.

In this Chapter, a new QD synthesis method is introduced that is slightly different from the conventional time-dependent QD synthetic approach. The drawback with a time-dependent synthesis process is that it leads to less consistent results because the time-scale required to control the QD size is generally of the order of a few seconds during the crystal growth stage. In order to obtain QDs with a narrow size distribution, a reagent-limiting engineering method is introduced by controlling the amount of precursor at the loading stage. In doing so, QDs with a narrow size distribution were obtained, which ensures uniform optical properties and efficient charge carriers transport. Attributed to the uniform distribution in the sizes of the QDs, it was possible to fabricate a multi-junction QDSC using three different sizes of QDs. This multi-junction enables the QDSC to absorb a wider range of the solar spectrum, which resulted in the generation of high photocurrent. A concomitant enhancement in the PCE in a single cell was observed, which led to the generation of higher power in a solar panel application (in 10 cells connected in series and 10 cells connected in parallel).

2.2 Quantum Dots

2.2.1 Fundamental properties of QDs

Typically, the properties of QDs can be categorised into three separated characteristics: quantum confinement, bandgap tunability, multiple exciton generation.

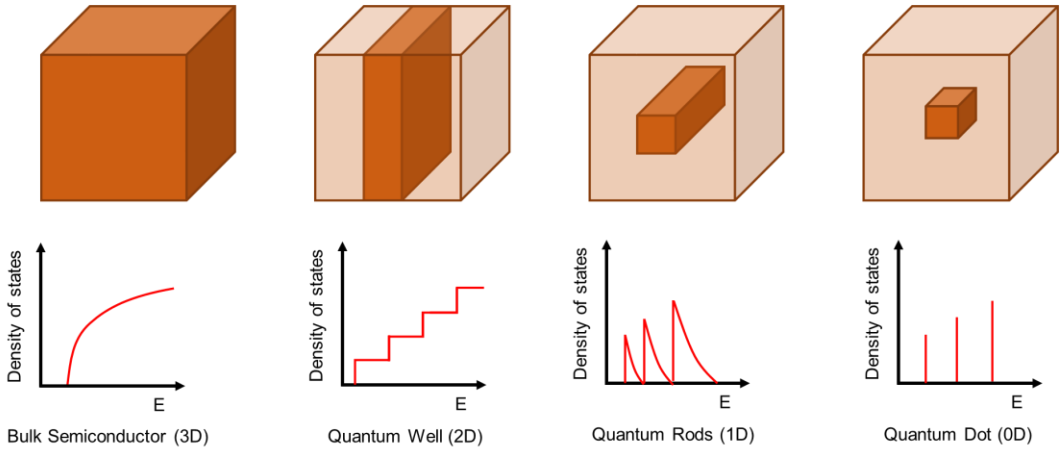

Figure 2.3: Illustration of the density of states (DOS) with respect to the dimensionality of the quantum confinement. For the three-dimensional confinement of a QD, the DOS becomes quantised and discrete.[50]

A quantum dot (QD) is generally known as a zero-dimensional material which confines the electron motion in three dimensions due to its extremely small size. The confinement leads to the formation of discrete and quantised energy states as shown in Figure 2.3. As a result of the quantised energy states, the electronic and optical properties of a QD are subject to change with respect to the size of the QD. This phenomenon is known as quantum confinement and can be observed by measuring the UV-Vis spectrum for different QD sizes (Section 2.3.2). Generally, quantum confinement is approximated by using a particle-in–a-box model and by solving the time-independent Schrodinger's equation. The magnitude of the quantum confinement effect is described using equation (2.6), where *a* is the radius of the QD.[50]

$$E_{confinement} = \frac{\hbar^2\pi^2}{2a^2}\left(\frac{1}{m_e} + \frac{1}{m_h}\right) = \frac{\hbar^2\pi^2}{2\mu a^2} \qquad (2.6)$$

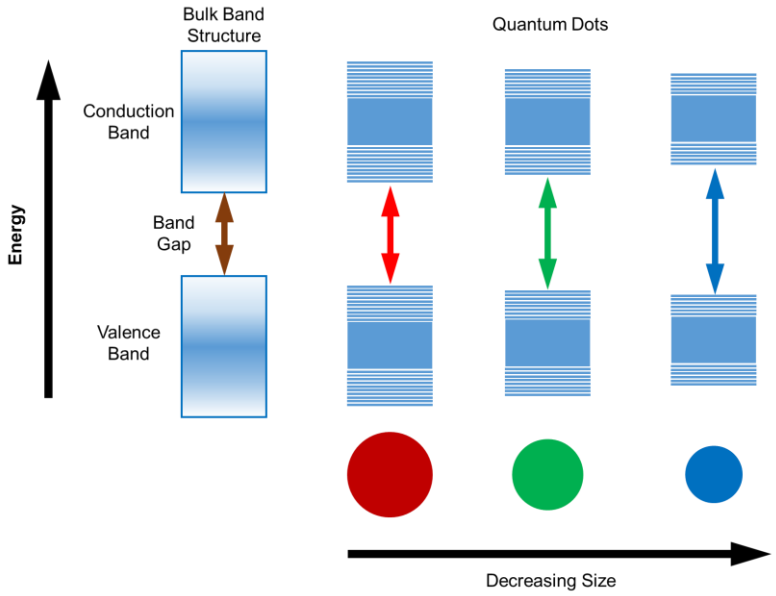

Figure 2.4: Quantum confinement leads to a splitting of the energy levels in a quantum dot. The electronic bandgap of a QD increases with a decrease in the size of the QD.[68]

Due to quantum confinement, the bandgap of a QD is dependent upon the confinement regime. For example, when the size of the QD becomes smaller the bandgap increases, i.e. the size of the QD is smaller than the exciton Bohr radius, which represents the most probable distance between the electron and hole pairs. Tuning of the electronic bandgap can be approximated by the following equation (2.7).[50]

$$E^{QD} = E_g^{bulk} + \frac{\hbar^2\pi^2}{2a^2}\left(\frac{1}{m_e} + \frac{1}{m_h}\right) - \frac{1.8e^2}{4\pi\varepsilon\varepsilon_0 a} \qquad (2.7)$$

Theoretically, multi-exciton generation can occur, in bulk materials as well as nanocrystals, such as QDs. Due to the relatively short lifetime of the excitons generated through MEG compared with that of a single exciton, however, the enhancement of the solar cell efficiency using this process was found to be negligible in bulk materials. Therefore, it was reported that a bandgap below 1.0 eV is required to have a measurable enhancement in the solar cell efficiency.[53]

2.2.2 Lead Chalcogenide QDs

Colloidal quantum dots (CQDs), which are synthesised and suspended in a solution phase, have attracted considerable interest as one of the most promising solar cell materials because of the facile and cost-effective synthesis process as well as the wide tunability of the bandgap, which is the result of quantum confinement.[69,70] Amongst the various CQDs that have been developed, lead-based quantum dots (QDs) such as lead sulfide (PbS) have been considered as the most attractive QDs for solar energy conversion devices as they can be synthesised from earth-abundant elements and exhibit a large Bohr radius (20nm) as well as wide tuning range of the band gap (0.4 to 3.0 eV).[71,72] In addition, PbS-based solar cells can be fabricated in ambient conditions by an all-solution process and they absorb sun-light above near-infrared (NIR) wavelengths, providing a high photocurrent compared to that of their organic counterparts.

2.3 QD Synthesis and characterisation

2.3.1 QD synthesis

One of the most widely and frequently used methods for CQD synthesis is the hot-injection method, which consists of three stages; mixing, nucleation, and the growth stage.[49] First, a Pb precursor, which is a mixture of lead oxide (PbO), oleic acid (OA), and octadecene (ODE), is loaded into a two-neck flask and heated to T = 100 °C in a vacuum for one to two hours. When the solution becomes clear, a sulfur precursor, hexamethyldisilathiane, or bis(trimethylsilyl) sulphide (TMS) dissolved in ODE, is injected. Upon the injection of the sulfur precursor, the nucleation stage is initiated. The size of the QDs is generally dependent on the reaction time during the growth stage. However, this causes inconsistent results as the reaction time for the growth of the QDs occurs within an extremely short time frame. To obtain QDs with a narrow size

distribution, therefore, a reagent-limiting hot-injection method has been introduced by controlling the lead precursor at the mixing stage. Instead of using a fixed PbO to OA ratio, different ratios of PbO to OA were loaded so as to synthesise and tune QDs with different bandgaps as summarised in Table 2.1.

Table 2.1: PbO to OA ratio to synthesise different sizes of bandgaps

Bandgap (eV)	PbO to OA ratio
0.84	1:17
0.91	1:14
1.03	1:11
1.14	1:8
1.23	1:5
1.30	1:3
1.37	1:2

2.3.2 Characterisation

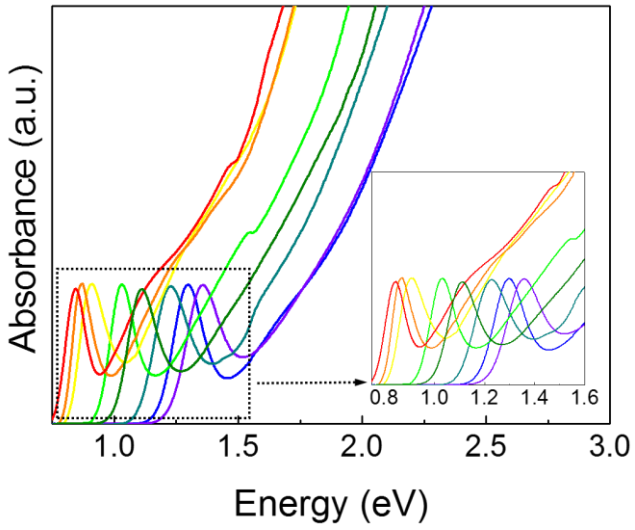

Figure 2.5: Optical absorption spectra for PbS QDs of a range of different sizes, which revealed that the optical bandgaps ranged from 0.84 to 1.37 eV.

The QDs synthesised with this new method were characterised by UV-Vis spectroscopy in order to identify the energies of the bandgaps. As shown in Figure 2.5, the QDs that were synthesised exhibited bandgap energies ranging from 0.84 to 1.37 eV, which indicates that the reagent-limiting synthesis method was effective at controlling the QD size as determined from the bandgap.

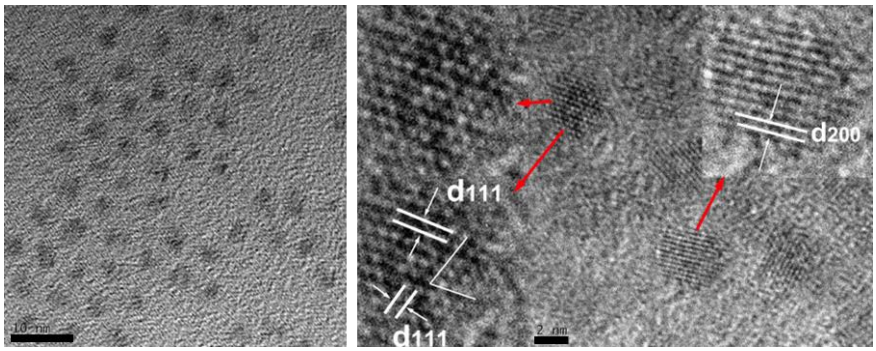

Figure 2.6: High resolution TEM (HRTEM) images of PbS QDs with a bandgap of 1.23 eV (scale bar: 10 nm for left image and 2nm for right image). Indices (200) and (111) show a typical rock-salt characteristic of PbS QDs. These HRTEM images were obtained by Dr. Hou in the Department of Engineering Science at the University of Oxford.

Crystallographic analysis using high-resolution TEM (HRTEM) was carried out on the QDs and Figure 2.6 shows TEM images of a 1.23 eV QD as a typical example. The HRTEM images revealed the typical rock-salt characteristics of QDs crystal, which showed indices corresponding to the (111) and (200) planes. The average value of the lattice constant of 1.23 eV PbS QDs calculated from each diffraction is $a = 5.62 \pm 0.02$ Å.[73]

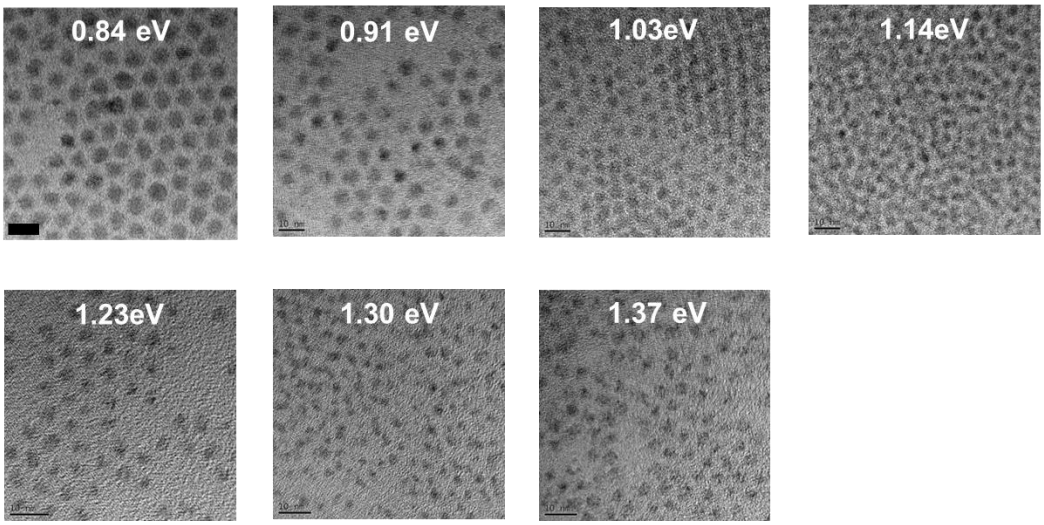

Figure 2.7: TEM images of the synthesised QDs with band-gaps ranging from 0.84 eV to 1.37 eV (Scale bar: 10 nm). Dr. Hou obtained the TEM images using the resources available in the Materials Department at the University of Oxford.

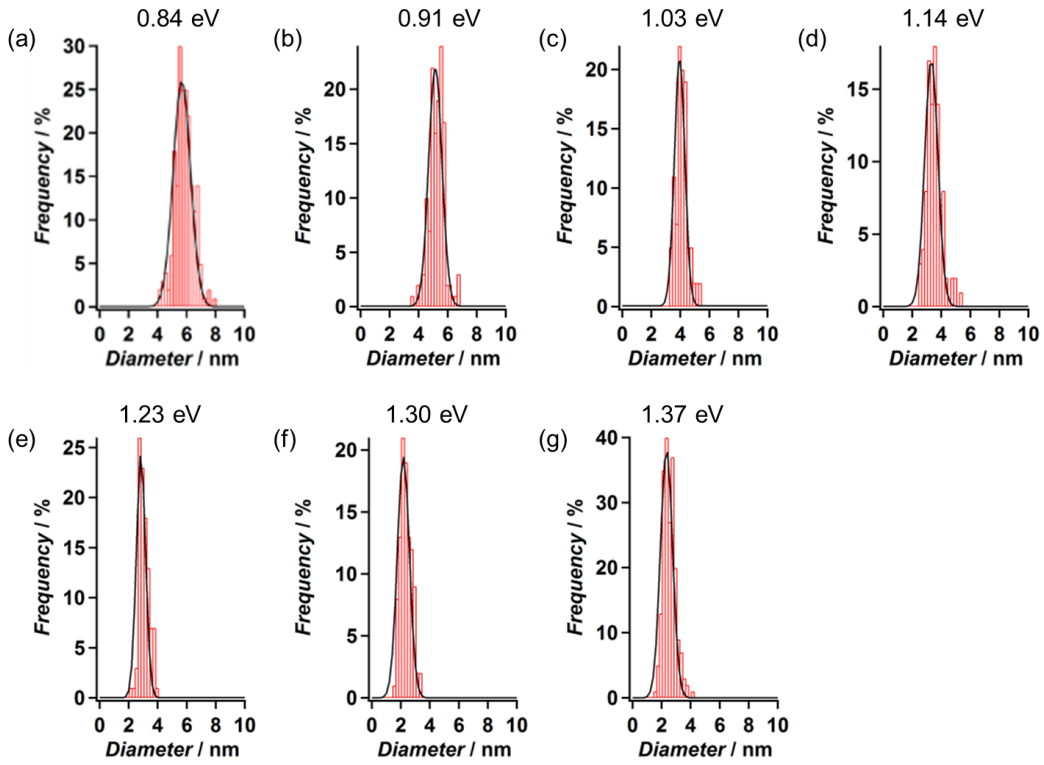

Figure 2.8: Histogram analysis using a Gaussian fitting plot of the as-prepared PbS QDs with bandgaps of (a) 0.84, (b) 0.91, (c) 1.03, (d) 1.14, (e) 1.23, (f) 1.30 and (g) 1.37 eV, respectively.

The synthesised QDs obtained using the new method were investigated by considering the standard deviation in the distribution in sizes as determined from TEM analysis (Figure 2.7). Statistical calculations of the size distribution revealed that a standard deviation for all the synthesised QDs was below 0.65 nm, which indicates that the reagent-limiting QD synthesis method can produce QDs towards monodispersity regardless of the bandgap of the QDs as shown in Figure 2.8.

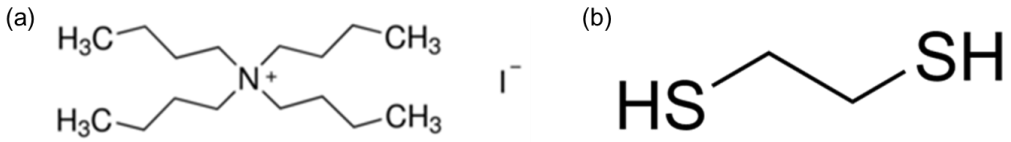

Figure 2.9: Molecular structure of the (a) TBAI and (b) EDT ligands.

Because the QDs are capped with a surfactant that consists of a long carbon chain (tail) and a polar head, such as oleic acid (OA) and oleylamine (OLA), the as-synthesised QDs behave as insulators. Therefore, the functionalisation of the QDs and the QD film is essential for changing the insulating nature to one that is semiconducting by performing a ligand exchange process. There are lots of different ligands that can be used for QD electronic applications. However, in this work, I have focused on a typical n-type ligand, Tetrabutylammonium iodide (TBAI), and a typical p-type ligand, 1,2-ethanedithiol (EDT). These ligands are commonly used in QDSC applications.[52,59,62,74] The molecular structures of TBAI and EDT are shown in Figure 2.9.

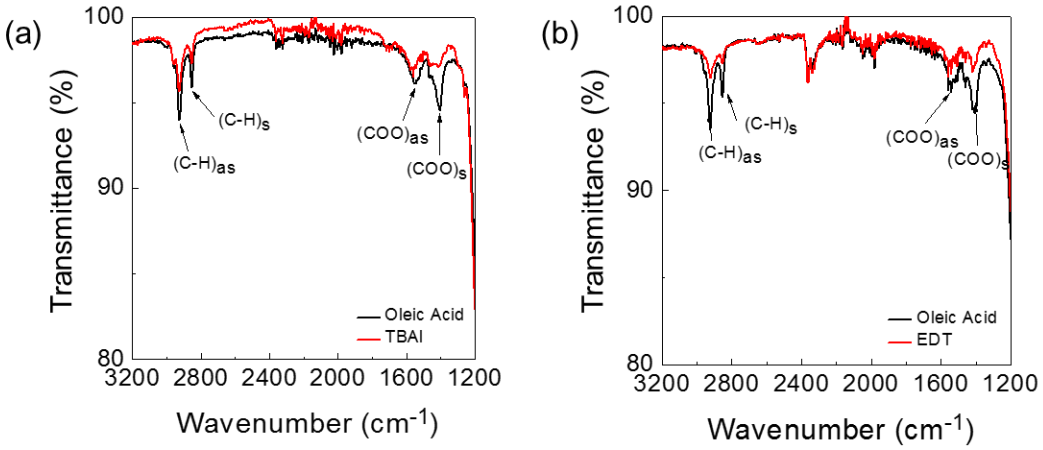

Figure 2.10: FTIR spectra of a QD film after (a) TBAI treatment and after (b) EDT treatment (red lines). For comparison, the spectra obtained for a QD film before the ligand exchange process (i.e. with oleic acid) is also shown (black lines).

After performing a ligand exchange method, the removal of OA was investigated using Fourier-transform infrared spectroscopy (FTIR). As the surfactant, OA, contains carbon-hydrogen (C-H) bonding and carboxyl groups (COOH) both along and at the end of the carbon chains, analysing the molecular vibration is a powerful tool to examine a removal of OA. The black curves in Figure 2.10 show the typical double molecular vibrations attributed to the C-H bonding and COO groups in the molecules of the OA ligand where the subscripts ‘s’ and ‘as’ indicate symmetric and asymmetric, respectively. After treatment with the TBAI and EDT ligands, a significant decrease in the C-H and COO molecular vibrations was observed, which indicates the significant removal of the OA attached to the QDs. However, it is observed that a small amount of OA still remained on the QD films, which is due partly to the OA ligands that were not washed off the surface of the QD films and also due to a contribution of the C-H bond in the TBAI ligand.[75]

It is worth noting that a ligand exchange process in QD electronic applications is essential in order to make the QD films conductive. Because colloidal QDs are normally

capped by organic ligands with long carbon chains, these chains form insulating barriers between the QDs that block the efficient transport of charge carriers.[76] By performing ligand exchange using relatively short inorganic or organic ligands, the spacing between QDs can be significantly reduced. As a result, charges are transported between QDs through hopping mechanisms.[77-80]

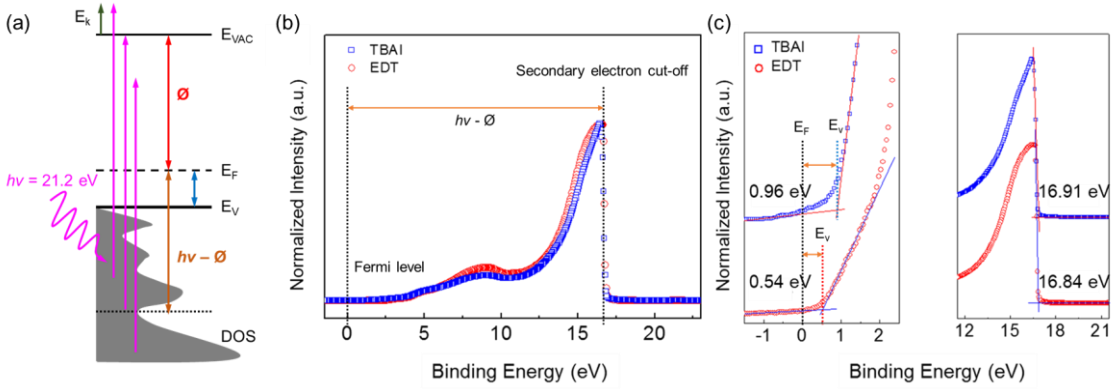

Figure 2.11: (a) Illustration of the energy diagram where the term DOS indicates the density of states. UPS of PbS QDs with a 1.25 eV bandgap that were prepared on ITO electrodes. The PbS QDs were ligand exchanged using TBAI (Blue) and EDT (Red); (b) full spectrum of the UPS analysis and (c) fitting to the measured TBAI and EDT-treated QD films. The UPS measurements were carried out by Dr. Yun at the Korea Basic Science Institute, Daejeon, Republic of Korea.

Successful ligand exchange from OA to TBAI or EDT ligands means that a QD film becomes a semiconductor. Ultraviolet photoelectron spectroscopy (UPS) analysis, which measures the kinetic energy spectra of emitted photoelectrons upon excitation of ultraviolet photons, was performed on a QD film that was treated with TBAI and EDT, respectively, so as to identify the semiconducting nature of each film. A Helium (He) source with a photon energy of 21.2 eV was used. From equation (2.8) and values of the insertion shown in Figure 2.11, I could calculate the energy levels of each QD film.

$$\Delta(\text{Secondary electron cutoff} - E_F) = h\nu - \emptyset$$

$$\emptyset = E_{VAC} - E_F \tag{2.8}$$

$$E_F - E_V = \text{energy difference from the figure}$$

For a fixed incident photon energy of 21.2 eV, the secondary electron cut-off (high binding energy edge) represents photoelectrons with zero kinetic energy (E_k) and the work function, for example in the case of TBAI, is Φ = 21.2 – 16.91 = 4.29 eV. As a result, the Fermi level is –4.29 eV with respect to E_{VAC}. Then, E_V of the TBAI is calculated by deducting the insertion that was measured by the UPS plot, which is found to be –5.25 eV. Finally, a conduction level is obtained by adding the bandgap of the material to the valence level, for example for TBAI E_C = –5.25 + 1.25 = –4 eV. Energy levels for the EDT-treated QD film were also calculated as described above. Table 2.2 summarises the energy levels of each TBAI- and EDT-treated QD film, which revealed that TBAI- and EDT-treated QD film was either n-type or p-type semiconductor, respectively.

Table 2.2: Band edge of each of the TBAI- and EDT-treated QD films that were analysed by UPS.

Ligand	E_V (eV)	E_F (eV)	E_C (eV)
TBAI	–5.25	–4.29	–4
EDT	–4.9	–4.36	–3.65

*bandgap of QD was 1.25 eV

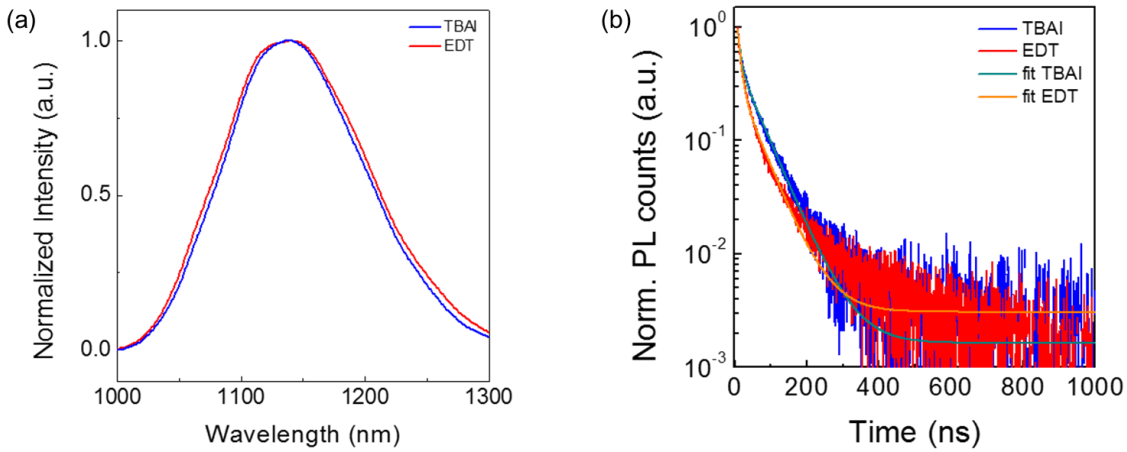

Figure 2.12: (a) PL curves and (b) TRPL curves of the TBAI- and EDT-passivated PbS QDs films. Dr. Lim performed the PL and TRPL in the Physics Department at the University of Oxford.

The time-resolved photoluminescence (TRPL) was measured in order to investigate the exciton lifetime of each TBAI- and EDT-treated QD film. Prior to TRPL measurements, the PL properties of each TBAI- and EDT-treated films were characterised to determine the wavelength at which the PL intensity was maximum as shown in Figure 2.12(a). Afterwards, the TRPL measurements were carried out using a nano-second pulsed laser with a wavelength that corresponds to the maximum in the PL intensity. As shown in Figure 2.12(b), TRPL decay curves were fitted using a biexponential decay function, which is characterised by two decay times of τ_1 = 8.02 ± 0.13 and τ_2 = 57.64 ± 0.38 ns for a TBAI-treated QD film, and τ_1 = 8.99 ± 0.09 and τ_2 = 54.86 ± 0.49 ns for a EDT-treated QD film.[81] The relatively short lifetime of the first exponent (τ_1) in both cases is due to the high rate of interparticle charge and energy transfer, which causes a rapid dissociation of excitons resulting in the suppression of the band gap emission whereas the longer decay time (τ_2) is attributed to carrier recombination.[82]

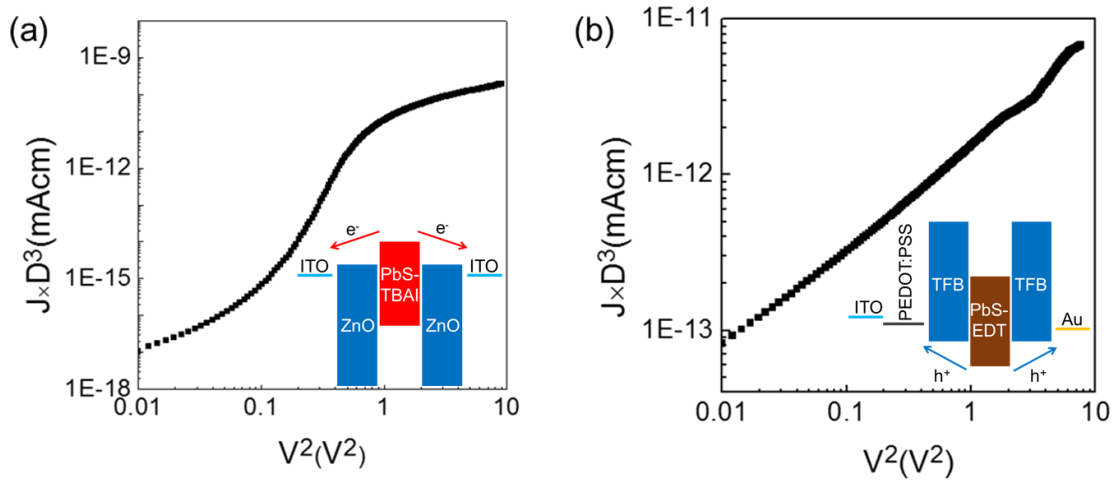

Figure 2.13: (a) An electron-only device for the TBAI-ligand QDs. (b) Hole-only device for QDs with an EDT ligand where insets show the structure of each electron and hole only device, respectively. It is assumed that the devices are space-charge limited.

Characterisation of the mobility of each QD film was further performed using space charge-limited current (SCLC) measurements as the mobility gives information on the transport of charge carriers together with the charge carrier lifetime. It is worth noting that the devices are assumed to be space-charge limited. For an electron-only device, it was fabricated with the structure (an inset) of ITO/ZnO/TBAI-QDs/ZnO/Al whereas a device of ITO/ PEDOT:PSS/TFB/EDT-QDs/TFB/Au structure was fabricated for the hole-only device where TFB is an abbreviation for poly(9,9-dioctylfluorene-alt-N-(4-sec-butylphenyl)-diphenylamine). The measured SCLC curves (Figure 2.13) were fitted using the Mott-Gurney law described below in equation (2.9).[83]

$$J_D = \frac{9\varepsilon\varepsilon_0\mu V_b^2}{8D^3} \tag{2.9}$$

where V_b is the applied bias, D is the total thickness of the device and ε is the dielectric constant of the QDs which is 21.2.[84] The electron mobility of the TBAI- and the hole mobility of the EDT-treated QD films were found to be μ_e = 3.508 x 10^{-2} $cm^2v^{-1}s^{-1}$ and μ_h = 4.384 x 10^{-2} $cm^2v^{-1}s^{-1}$, respectively, which are comparable to one another.

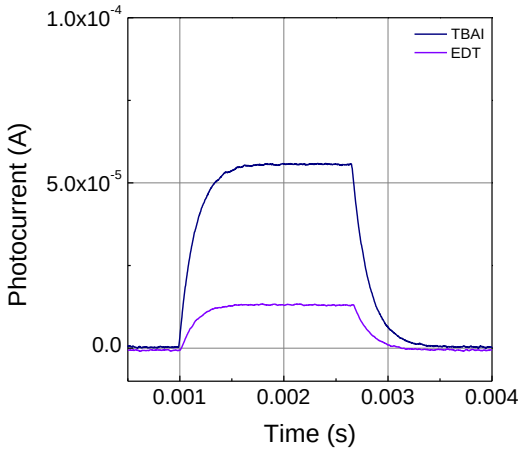

Figure 2.14: Photo-response of the TBAI- and EDT-treated QD films at 1 V bias condition using a 450 nm laser with an incident power density of 4.5 mW cm^{-2}.

Lastly, relative information on the number of defects and sub-bandgap states of each QD film was obtained by analysing the rise and fall times of photo-response of a two-terminal QD device.[85,86] For the photo-response measurement, a blue laser (λ = 450 nm) with an incident power density of 4.5 mW cm^{-2} at an input frequency of f = 300 Hz was employed. Figure 2.14 shows the photocurrent of each device upon excitation. Rise and fall times were found to be 3.34×10^{-4} sec and 3.42×10^{-4} sec, respectively, for the TBAI-treated device. In contrast, both the rise and fall times for the EDT-treated device were faster than those of the TBAI-treated device, which were 2.82×10^{-4} sec and 3.30×10^{-4} sec, respectively, suggesting that the EDT-treated film has less defects and sub-bandgap states than the TBAI-treated QD films. However, the lower photocurrent observed for the EDT-QD film in comparison to that of the TBAI-QD film indicates that light absorbance is not as good as that of the TBAI-QD film, considering that the electron mobility of TBAI-QD and electron mobility of EDT-QD are comparable. A similar phenomenon was also observed in the corresponding QDSCs that will be discussed in Section 2.5.

2.4 Quantum dot photovoltaics

2.4.1 A solar cell structure

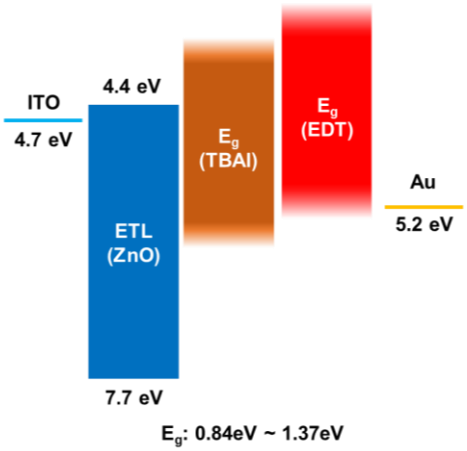

Figure 2.15: A schematic of the energy levels of a QDSC that consists of an ITO electrode, a ZnO ETL, a TBAI-treated QD layer, an EDT-treated QD layer, and an Au electrode.

Figure 2.15 shows a schematic of the QDSC based upon an inverted structure: in this case, electrons are collected at the ITO electrode whereas the holes are collected at the Au electrode. The light absorbing layer consists of TBAI-treated QD layers (250 ~ 280 nm) and thin EDT-treated QD layers (50 nm), which acts as an electron blocking layer.[67] Throughout Chapter 2, I have explored both the simulations and the experiments with the structure, unless otherwise stated.

2.4.2 Simulation results using SCAPS

Simulation studies were performed by using SCAPS, which was developed at the Department of Electronics and Information Systems at the University of Gent, Belgium, for one dimensional solar cell simulations. Currently, the SCAPS simulation program is widely used amongst researchers working on the subject of photovoltaics.[87-89] Tables 2.3, 2.4, and 2.5 summarise the parameters used in the simulation studies.

Table 2.3: Parameters for the physical properties of each layer.

Parameters	ZnO	TBAI – PbS QDs (Gradient)		EDT – PbS QDs
Thickness (nm)	50	250*		50
Relative permittivity (ε)	66	20		20
Band Gap (eV)	3.3	1.3*		1.3*
Electron Affinity (eV)	4.3	4.2	3.9	3.9
Effective Density of states, Conduction band (cm^{-3})	1.00E+19	1.00E+19		1.00E+19
Effective Density of states, Valence band (cm^{-3})	1.00E+19	1.00E+19		1.00E+19
Electron Mobility ($cm^2V^{-1}s^{-1}$)	5.00E-02	2.00E-02	2.00E-02	2.00E-04
Hole Mobility ($cm^2V^{-1}s^{-1}$)	5.00E-02	2.00E-02	2.00E-02	2.00E-02
N_D grading dependent	1.00E+17	1.00E+15	1.00E+14	1.00E+14
N_A grading dependent	0	1.00E+15	1.00E+16	1.00E+16

*Unless otherwise stated

Table 2.4: Parameters for the defects in the QD layers.

Parameters	TBAI – PbS QDs	EDT – PbS QDs
Defect type	Neutral	Neutral
Capture cross section electrons (cm^2)	1.2E-13	1.2E-13
Capture cross section holes (cm^2)	1.2E-13	1.2E-13
energetic distribution	Single	Single
Reference for defect energy level E_t	Below E_C	Above E_V
Energy level with respect to Reference (eV)	0.5	0.5

Table 2.5: Parameters for the defects between the TBAI-EDT interfaces.

Parameters	TBAI-EDT interface
Defect type	Neutral
Concentration (cm^{-2})	1E+19
energetic distribution	Single
Reference for defect energy level E_t	Above E_V
Energy level with respect to Reference (eV)	0.6

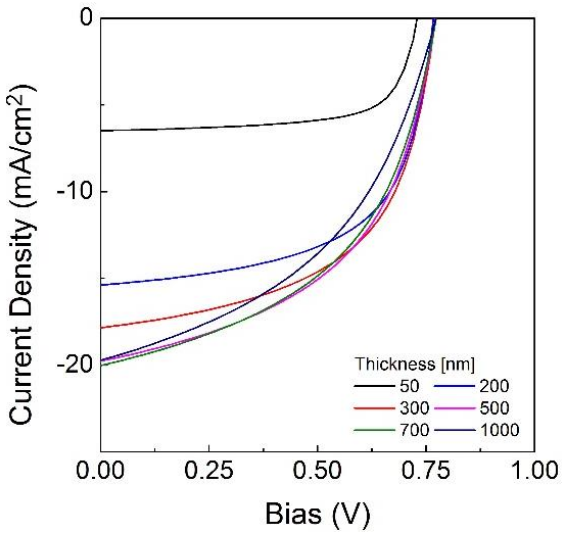

Figure 2.16: Thickness dependence of the QDSC performance obtained using the SCAPS simulation software. Thickness of the light absorbing layers were 50, 200, 300, 500, 700, and 1000 nm.

First, the thickness dependent solar cell performance was studied as it is reported that the thickness of the QD layer needs to be larger than 500 nm in order to completely absorb sunlight.[90] However, because the QD films typically have a relatively short diffusion length in comparison to the desirable thickness for photon harvesting, a trade-off between light absorbance and charge carrier transport needs to be carefully considered. For the simulations, I used only a TBAI-QD layer (a light absorbing material) in order to

investigate the effect of thickness on the device performance. Figure 2.16 presents the performance of a QDSC as a function of several different thicknesses. As the thickness of the QD layer increased, an enhancement in the solar cell performance was observed, which is mainly attributed to an enhanced J_{sc}. However, when the thickness of the QD layer was larger than 500 nm then no further enhancement in the solar cell performance was observed. Instead, a degradation in the solar cell performance was observed for a 700 nm-thick QD layer due to severe charge carrier losses. It is worth noting that the maximum PCE was obtained for a thickness within the 270 nm ~ 320 nm range for the case of an experimentally-fabricated QDSC, which is slightly different from the results obtained from the simulations. This is probably due to the number of assumptions made in the simulations such as the density of defects, the energy levels of the defects and so on.

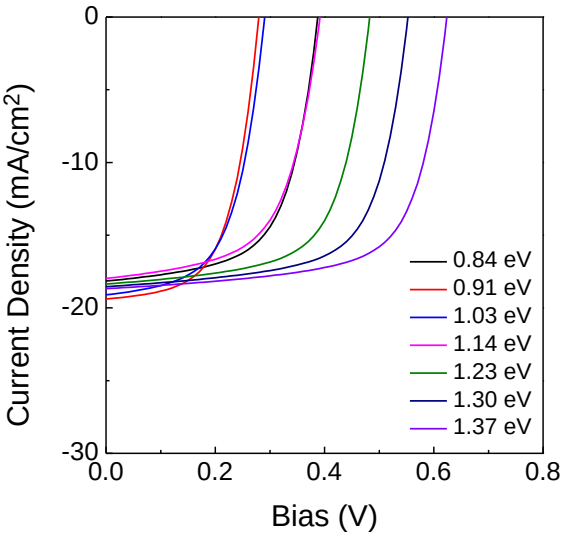

Figure 2.17: Dependence of the QDSC performance on the size of the bandgap as determined from the SCAPS simulation software. The bandgaps of the QDs that were used were 0.84, 0.91, 1.03, 1.14, 1.23, 1.30, and 1.37 eV.

Together with the thickness of the QD layer, another important parameter of the solar cells is the optimum bandgap for solar energy harvesting as the photo-active material cannot absorb photons which have an energy that is lower than the bandgap of the material. However, if the bandgap is too small then the V_{oc} of the solar cell decreases because the V_{oc} is dependent on the bandgap of the material. As the Shockley–Queisser limit describes, it is generally known that a bandgap of 1.2 ~ 1.4 eV is optimum for solar energy harvesting.[63] Figure 2.17 shows that the V_{oc} and PCE were improved when the bandgap of the QD was increased. However, in addition, a decrease in J_{sc} was observed and thus there is a trade-off between the absorption of light over a wider solar spectrum using a small bandgap and a larger potential that is obtained using a large bandgap. Although the simulation results showed a constant enhancement in the PCE up to an electronic bandgap of 1.37 eV, our experimental results revealed that QDs with a bandgap above this value exhibited a degradation in the device performance. This is because a high surface-to-volume ratio can result in the formation of defects and charge trapping sites at the QD interfaces.

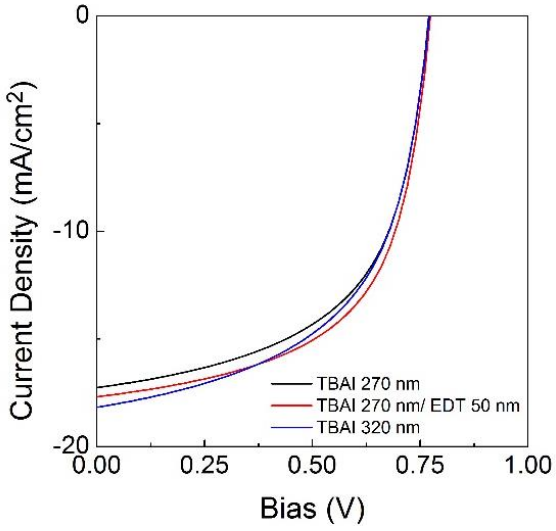

Figure 2.18: The effect of an electron blocking layer (EBL) on the performance of a QDSC. The introduction of an EBL showed enhanced performance when compared to that of a reference cell.

Lastly, the effect of an electron blocking layer (EBL) on the solar cell performance was studied by using an EDT-treated QD layer as the EBL, which was first reported by Chuang *et al.* in Nature Materials in 2014.[67] As shown in Figure 2.18, the deposition of an EDT-QD layer on top of the TBAI layer showed an enhanced efficiency from 7.6% to 8.1%. Also, a control simulation was carried out to further confirm that the enhanced PCE was attributed to the prevention of a backflow of electrons and not due to a thicker QD film. The blue curve in Figure 2.18 shows that the TBAI-QD layer with the same thickness as that of the TBAI-EDT one generated a higher current due to more light absorption. However, it also exhibited a lower FF than that of the TBAI-EDT one, which resulted in only a 0.1% enhanced PCE (7.7%) compared to the reference cell (black curve), which revealed that the enhancement in the PCE was attributed to the introduction of the EBL.

2.4.3 Experimental Results

For the actual QDSC device fabrication, ZnO nanoparticles in a solution phase were spin-coated onto a patterned ITO substrate at 3000 rpm for 30 seconds. QD layers were deposited using a layer-by-layer spin-coating method until the desired thickness was attained. A bandgap of 1.23 ~ 1.28 eV PbS QDs was used for the solar cell fabrication unless otherwise stated. Ligand exchange was performed after the deposition of each QD layer using the TBAI at a concentration of 10 $mgml^{-1}$ in methanol and the EDT at a concentration of 0.02 v% (volume percent) in acetonitrile. This was then followed by twice methanol and acetonitrile washing, respectively. The total thickness of the QDSC was around 430 ~ 500 nm, which comprised of the ZnO ETL (80 ~ 100 nm), a QD layer (300 ~ 320 nm), and an Au electrode (100 nm).

For the solar cell measurements, a solar simulator (LOT-Quantum Design) with an AM 1.5 G filter was used, which had a power density of 100 $mWcm^{-2}$ unless otherwise stated and a source meter (Keithley 4200-SCS). Calibration of the light power was carried out using a standard solar cell (Rera system) before each solar cell measurement. All the solar cells were measured at room temperature in ambient air.

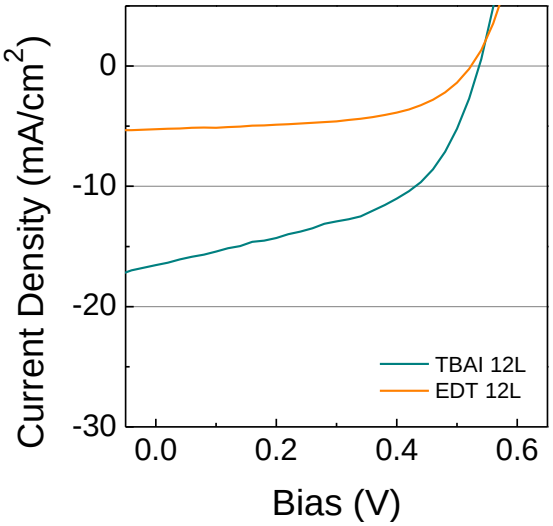

Figure 2.19: The performance (J-V curves) of a QDSC that consists of either 12 layers of TBAI (light green) or 12 layers of EDT (orange).

Figure 2.19 shows the solar cell performance when only one type of ligands was used: TBAI or EDT, each consisting of 12 layers (approximately 300 nm-thick). Also, energy band levels of each layer as well as the aligned band levels with respect to the Fermi level are shown in Figure 2.20 ((a),(b) for a QDSC using TBAI- and (c),(d) for a QDSC using EDT-treated QD layers). Consistent with the photo-response measurements (Section 2.3.2, Figure 2.14) the QDSC treated with TBAI ligands generated higher photocurrent than that of an EDT-treated QDSC, which is due to the different absorption coefficients for each of the TBAI- and EDT-treated QD films as well as the energy level alignments with the ZnO and Au layers. However, both QDSCs showed a relatively poor

device performance, less than 4 %, which is partly due to the absence of an electron blocking layer. More details on the effect of an electron blocking layer are provided shortly. The average values obtained for the solar cell parameters, taken from 15 different devices, are shown in Table 2.6.

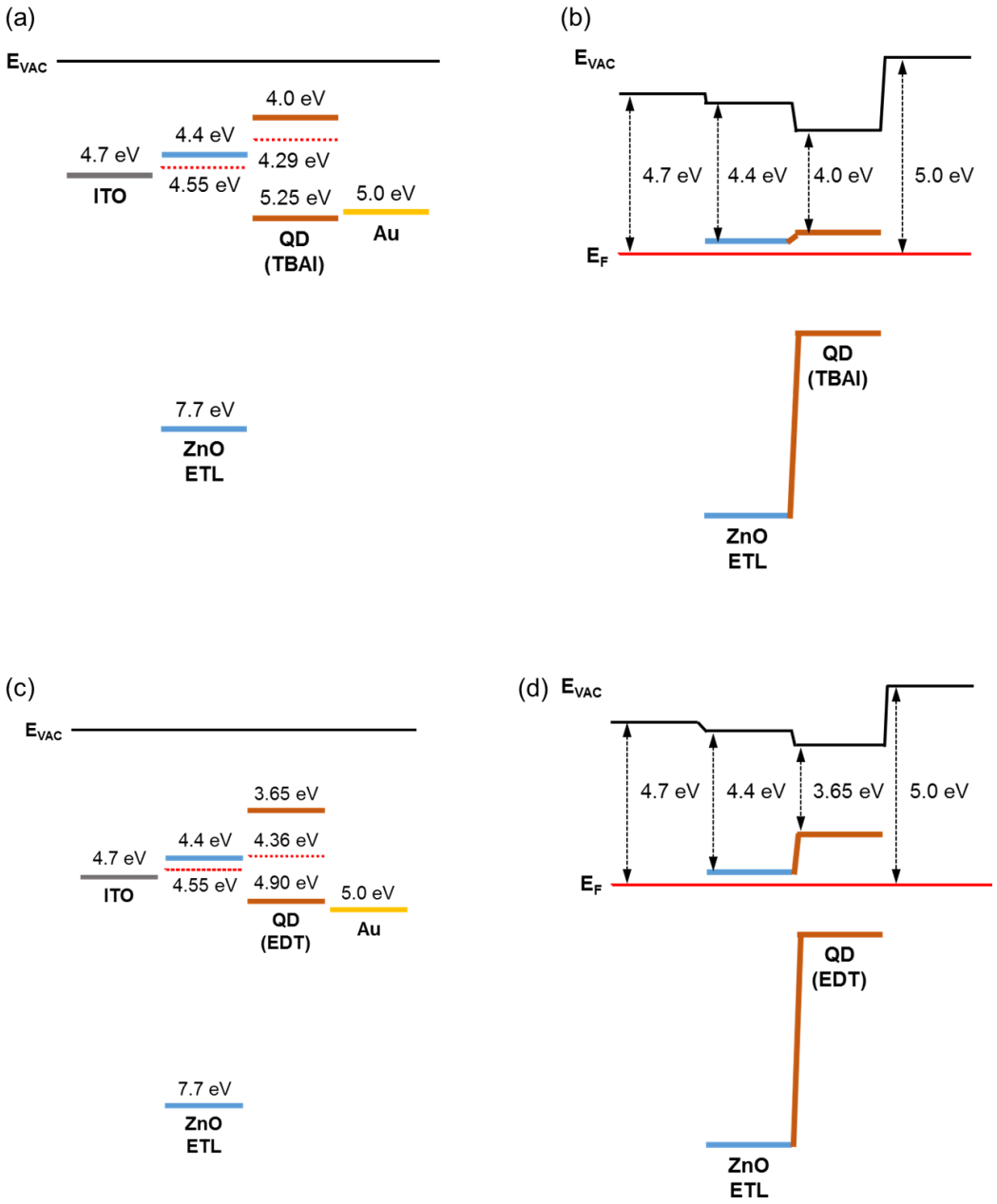

Figure 2.20: Schematics of energy level of each layer before (a), (c) and after alignment (b), (d) in the case of QDSCs using TBAI- and EDT-treated QD film, respectively.

Table 2.6: Performance of QDSCs using 12 layers of either TBAI or EDT.

Sample	V_{oc} (V)	J_{sc} (mA/cm^2)	R_s (Ωcm^2)	R_{sh} (Ωcm^2)	FF	PCE (%)
T 12L	0.532 ± 0.01	14.42 ± 2.41	9.75 ± 2.39	167.88 ± 14.19	0.49 ± 0.01	**3.77 ± 0.58**
E 12L	0.516 ± 0.01	4.96 ± 0.38	1.80 ± 0.47	68.82 ± 4.33	0.56 ± 0.01	**1.42 ± 0.12**

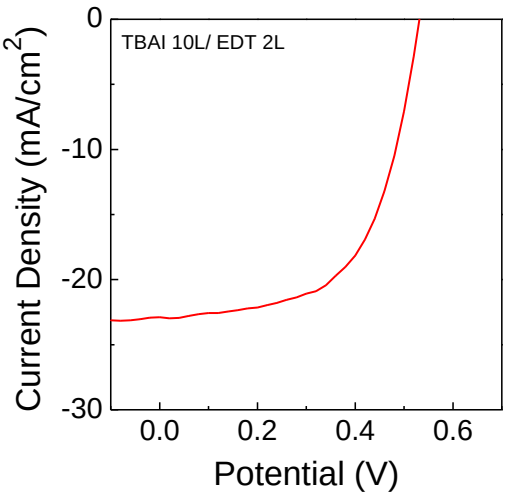

Figure 2.21: The performance of a QDSC with the introduction of an EBL. The QDSC consists of 10 layers of TBAI and 2 layers of EDT.

A significant enhancement in the solar cell performance was observed when an EDT-treated QD layer was introduced on top of the TBAI layers as an EBL, as shown in Figure 2.21. Due to the higher valence and conduction levels of the EDT-treated QD layer compared with those of the TBAI-treated QD layer, a potential barrier between the two layers was formed, which prevented the backflow of electrons.[67] Also, the junction formed between the two layers induced an electric potential, which led to higher exciton dissociation rates and more efficient charge carrier transport. As a result, significant J_{sc}, FF and concomitant PCE enhancements were observed, which were found to be from 14.42 ± 2.41 mAcm^{-2} to 24.48 ± 1.15 mAcm^{-2}, from 0.49 ± 0.01 to 0.54 ± 0.03, and from 3.77 ± 0.58 to 7.56 ± 0.46 %, respectively. Other solar cell parameters are also

summarised in Table 2.7, which represent the average values taken over 15 devices. The results highlight the importance of an EBL in order to obtain a high efficiency solar cell.

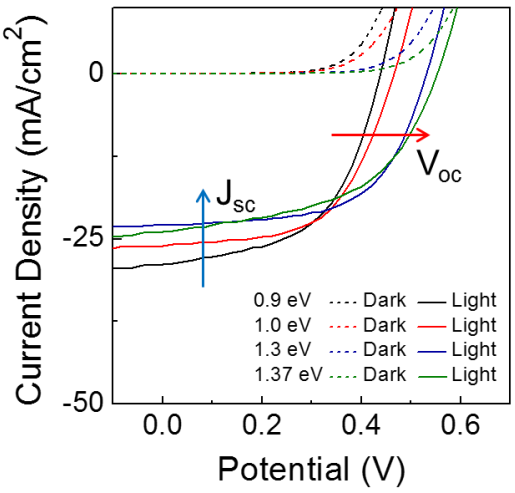

Figure 2.22: Performance of the QDSC with respect to the size of the bandgap of the QDs. QDs with bandgaps of 0.9, 1.0, 1.3, and 1.37 eV are shown in the figure and the remaining sizes are summarised in Table 2.8.

Table 2.7: Parameters for the TBAI-EDT junction structure QDSC.

V_{oc}(V)	J_{sc}(mAcm^{-2})	R_s(Ωcm^2)	R_{sh}(Ωcm^2)	FF	PCE (%)
0.58 ± 0.02	24.48 ± 1.15	5.8 ± 1.73	197.99 ± 19.41	0.54 ± 0.03	7.56 ± 0.46

Followed by the introduction of an electron blocking layer to the QDSC, I fabricated and optimised the QDSCs with different sizes of QDs, i.e. different electronic bandgaps, for a potential application in multiple junction QDSCs that can harvest a wider range of the solar spectrum and also induce a built-in electric field to efficiently extract the photo-generated charges at each junction (more details will be provided in the next section). As shown in Figure 2.22, a trend is observed whereby the V_{oc} increases while the J_{sc}

decreases as the bandgap is increased. This is because as the bandgap of the QDs decreases they are able to absorb more sunlight (absorb photons with energies greater than their bandgap). As a result, the J_{sc} was enhanced whereas the V_{oc} decreased as the maximum V_{oc} cannot be larger than the bandgap of QDs.

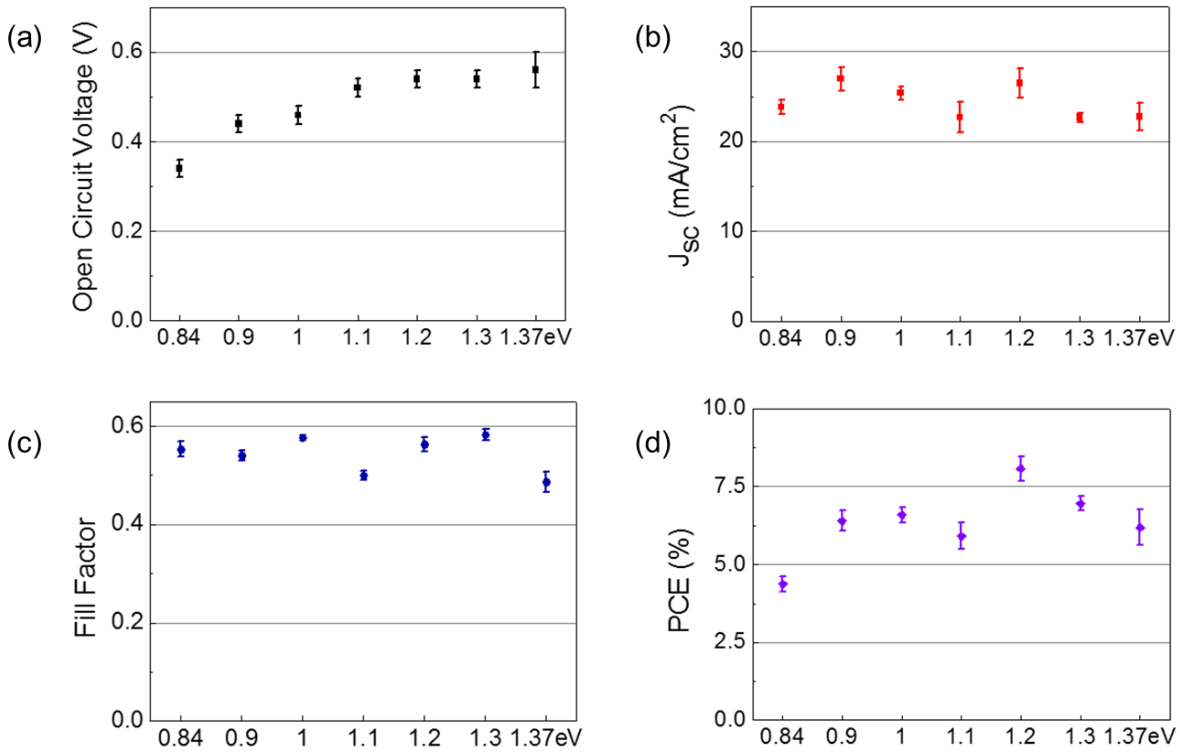

Figure 2.23: Summary of the key factors that affect the PCE of a solar cell with respect to the size of the bandgap of a QD.

Figure 2.23 summarises the solar cell parameters with respect to different bandgap energies. The V_{oc} clearly shows an increasing trend whereas the J_{sc} exhibits a decreasing trend, with some scatter in the data, as the bandgap increases. The highest PCE that was obtained was for the QDs with a bandgap energy of approximately 1.2 eV. The solar cell parameters averaged over 15 different devices are shown in Table 2.8.

Table 2.8: Parameters for the QDSCs with respect to the size of the bandgap of the QD.

Bandgap (eV)	V_{oc} (V)	J_{sc} (mAcm^{-2})	R_s (Ωcm^2)	R_{sh} (Ωcm^2)	FF	PCE (%)
0.84	0.35 ± 0.01	22.66 ± 1.39	4.54 ± 2.79	314.07 ± 32.99	0.57 ± 0.02	**4.54 ± 0.06**
0.91	0.44 ± 0.01	27.58 ± 1.34	8.47 ± 2.86	296.20 ± 23.99	0.54 ± 0.01	**6.59 ± 0.32**
1.03	0.47 ± 0.01	25.46 ± 1.05	3.49 ± 1.84	267.64 ± 20.01	0.59 ± 0.02	**7.01 ± 0.32**
1.14	0.53 ± 0.01	22.70 ± 1.92	8.34 ± 1.94	213.28 ± 24.86	0.50 ± 0.02	**6.07 ± 0.60**
1.23	0.54 ± 0.0	26.77 ± 1.77	5.39 ± 1.55	253.46 ± 30.09	0.56 ± 0.02	**8.03 ± 0.39**
1.30	0.58 ± 0.02	24.48 ± 1.15	5.80 ± 1.73	197.99 ± 19.41	0.54 ± 0.03	**7.56 ± 0.46**
1.37	0.55 ± 0.01	26.06 ± 1.34	9.17 ± 2.24	181.40 ± 33.87	0.49 ± 0.02	**7.13 ± 0.46**

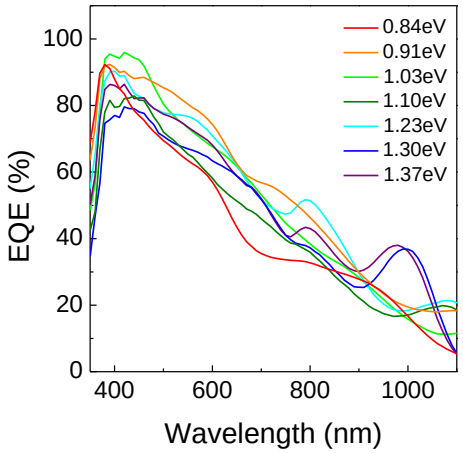

Figure 2.24: EQE spectra of the QDSCs with respect to the bandgap energy of the QD.

External quantum efficiency (EQE) of each QDSC with respect to the bandgap of a QD was measured across the spectral range from 350 nm to 1100 nm, which was calibrated by a silicon reference cell. By integrating over the measured range, we can obtain the $J_{sc\text{-}EQE}$ value as presented in Table 2.8. A slight discrepancy in the $J_{sc\text{-}EQE}$ value

compared to J_{sc} value (Table 2.8) is due to current contribution at wavelength greater than 1100 nm and a change in the photo-active materials under light illumination.[58,91]

Table 2.9: $J_{sc\text{-}EQE}$ of each QDSC using a different bandgap by integrating over the EQE spectra in Figure 2.24.

Bandgap (eV)	0.84	0.91	1.03	1.14	1.23	1.30	1.37
$J_{sc\text{-}EQE}$	18.08 ± 2.50	23.44 ± 3.70	21.64 ± 4.12	20.59 ± 4.12	22.70 ± 7.30	20.81 ± 1.70	22.37 ± 3.70

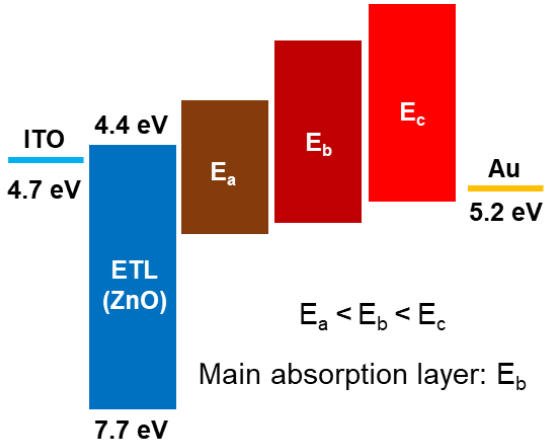

Figure 2.25: A schematic of the multi-junction QDSC structure, where E_a, E_b, E_c denote the bandgaps of the QDs following the sequence, $E_c > E_b > E_a$.

As the Shockley-Queisser limit explains, the maximum PCE that can be obtained using a single bandgap is limited to below 40 %. In this regard, I propose and demonstrate now a multi-junction QDSC so as to further enhance the PCE of the QDSC by using the optimised QDSC reported in the previous section for different bandgap sizes. Figure 2.25 shows the multi-junction QDSC structure where smaller bandgap QDs were deposited first and then the largest ones were deposited at the last stage so as to facilitate efficient electron and hole extraction to the ITO and Au electrodes, respectively. It is worth noting

that the total thickness of the QD layers was fixed at 300 nm ~ 320 nm and the structure of the QD layers consisted of 1 layer of E_a, 9 layers of E_b, and 2 layers of E_c.

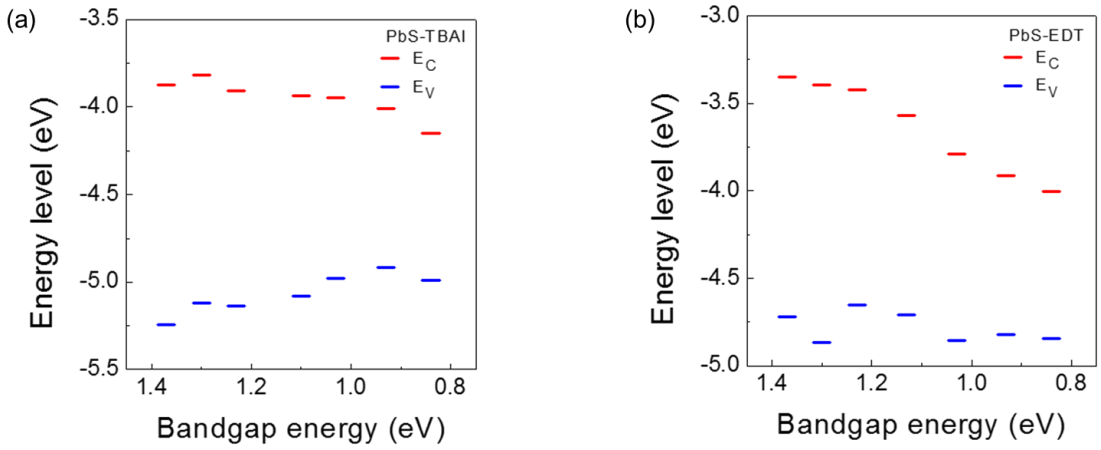

Figure 2.26: Conduction and valence band edges of (a) a TBAI-treated QD layer and (b) an EDT-treated QD layer with respect to the bandgap energy of the QD.

Conduction and valence band edges for different sizes of QDs that were treated with the TBAI and EDT ligands were measured using UPS as shown in Figure 2.26. It is revealed that all sizes of QDs are able to form a Type II junction using the TBAI and EDT ligands. Considering the trade-off between the J_{sc} and the V_{oc}, as well as the coverage of a wider portion of the solar spectrum, it is not desirable to use QDs with bandgaps that are either too small or too large to form the multi-junction. Based upon the measurements for a single junction QDSC presented in Table 2.8, bandgaps of 1.0 eV and 1.23 eV were chosen as they exhibited a good solar cell performance, which were deposited as 1 and 9 layers, respectively. For the electron blocking layer (an EDT-treated QD layer), the highest bandgap (1.37 eV) was employed as these QDs form the largest energy barrier when compared with the other QDs.

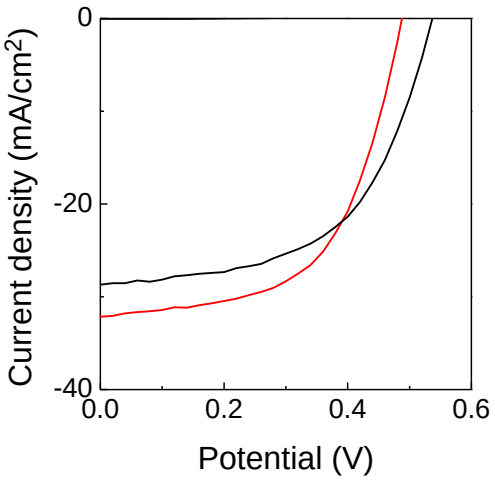

Figure 2.27: Performance (J-V characteristics) of a single junction, 1.23 eV (Black), and a multi-junction solar cell (Red).

Figure 2.27 shows the results for the multi-junction solar cell performance (red curve) compared with a QDSC using QDs with a 1.23 eV bandgap (black curve). As expected, the J_{sc} was significantly enhanced by harvesting more photons, which is attributed to the relatively small bandgap energy of the QDs. At the same time, however, a decrease in the V_{oc} was observed due to the decrease in the potential difference between E_{fn} and E_{fp} through the employment of the small bandgap QDs. The efficiency of the multi-junction QDSC was found to be 9.05 % with V_{oc} = 0.52 V, J_{sc} = 32.51 mAcm^{-2}, and FF = 0.59, which demonstrated an approximately 0.6% enhancement in the PCE value. The average values for the multi-junction solar cell parameters were compared with those of a single junction solar cell (1.23 eV) as shown in Table 2.10, which again confirmed that there was an enhancement in the solar cell performance using a multi-junction structure.

Table 2.10: Summary of the characteristics of a single junction (1.23 eV) QDSC and a multi-junction QDSC.

Bandgap (eV)	V_{oc} (V)	J_{sc} (mAcm^{-2})	R_s (Ωcm^2)	R_{sh} (Ωcm^2)	FF	PCE (%)
1.23	0.54 ± 0.0	26.77 ± 1.77	5.39 ± 1.55	253.46 ± 30.09	0.56 ± 0.02	8.03 ± 0.39
1.03/1.23/1.37	0.50 ± 0.02	31.24 ± 0.92	4.60 ± 1.70	304.35 ± 14.52	0.56 ± 0.03	8.67 ± 0.28

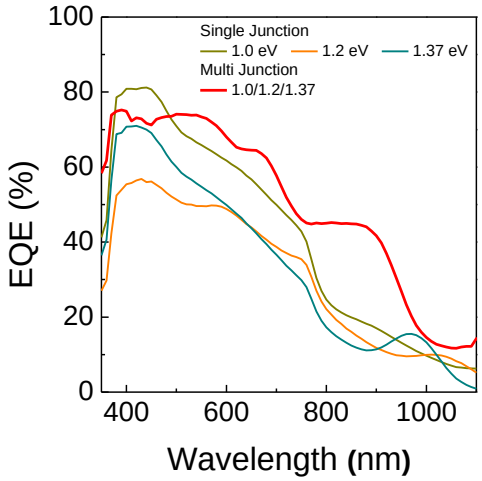

Figure 2.28: EQE spectrum of single junction QDSCs (1.0 eV – dark yellow, 1.2 eV – orange, 1.37 eV – green) and a multi-junction QDSC (Red).

Consistent with the J-V measurements, the EQE curve also showed a significant enhancement over the range of 350 to 1100 nm, except for QDs with a 1.0 eV which exhibited a higher EQE over the range from 350 to 500 nm and is attributed to the effect of MEG resulting from the smaller bandgap QDs. The integrated area (a multi-junction solar cell) over the spectrum was found to be 30.11 mAcm^{-2} (28.01 ± 2.10 mAcm^{-2}). A slight discrepancy in the $J_{sc\text{-}EQE}$ value compared to J_{sc} in Table 2.10 is due to current contribution from wavelength above 1100 nm and a change in the photo-active materials under light illumination.[58,91] The J-V sweep and EQE measurement revealed that a multi-junction solar cell is a promising way to further improve the QDSC performance.

2.5 From solar 'cell' to 'panel'

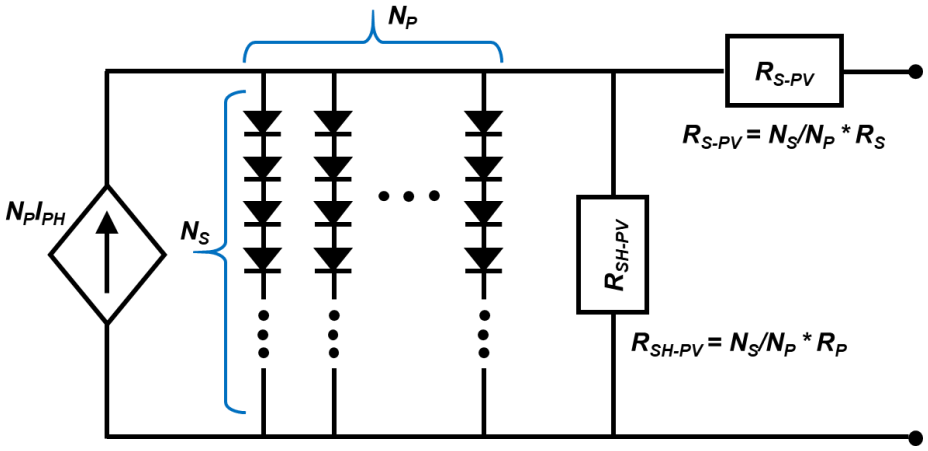

Figure 2.29: The equivalent circuit of a solar panel, where N_s and N_p indicate the number of cells connected in series and in parallel, respectively.

Based on the results shown in Table 2.10, I further demonstrate a QDSC in a solar panel application. Generally, solar panels consist of a set of solar cells connected in series and in parallel in order to enhance both the V_{oc} and J_{sc}, and consequently the output power. Figure 2.29 shows an equivalent circuit of a solar panel where N_s and N_p indicate the number of cells connected in series and parallel, respectively. The simulation was performed using MATLAB/Simulink and the conditions, such as temperature and ideality factor, were fixed for all simulations to 25 ℃ and 1.2, respectively.[92,93]

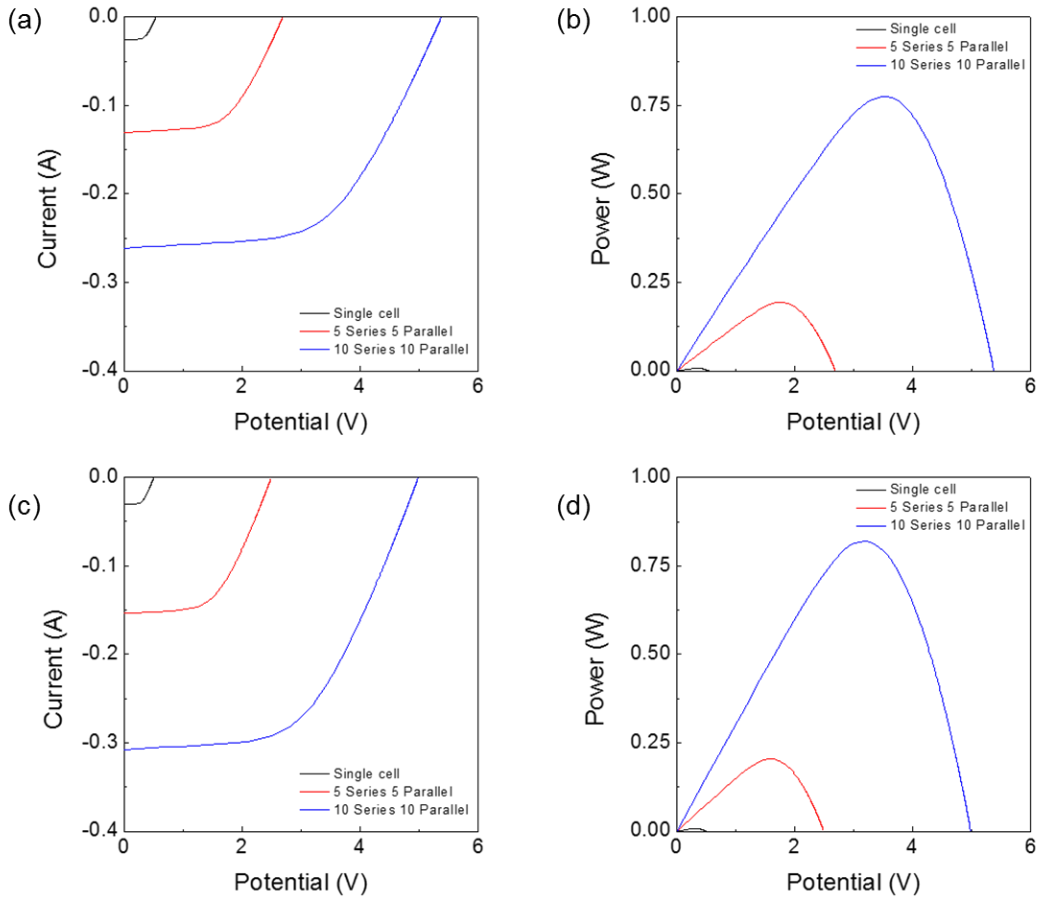

Figure 2.29: Demonstration of a solar panel using a single junction solar cell (a) and (b), and a multi-junction solar cell (c) and (d) where the parameters for the simulations are listed in Table 2.10.

As shown in Figure 2.29, as the number of cells connected in series and parallel increases, the I_{sc} and V_{oc} are improved for both the single junction and multi-junction QDSCs. The slightly higher V_{oc} of the single junction solar cell compared to that of the multi-junction solar cell (Table 2.10) induces a big difference in V_{oc} when 10 solar cells were connected in series, which is the same as for the case of the I_{sc}. As a result, the maximum powers that can be delivered by the solar panel using a single junction solar cell and the solar panel using a multi-junction solar cell were found to be approximately 0.77 W and 0.82 W, respectively. The simulation results highlight that an improvement in a single solar cell is directly related to an enhancement in the solar panel and thus the

proposed strategy for fabricating a high efficiency solar cell using a multi-junction is an effective way of realising a high efficiency solar panel in the future.

2.6 Conclusions

In this chapter, I have reviewed the current PbS-based QDSC technology and the challenges that it is currently facing. In order to address the theoretical limit of a solar cell and the challenges ahead, I have developed a reagent-limiting PbS QD synthesis method. Compared to the conventional time-dependent PbS QD synthesis method, it was shown that highly mono-dispersed QDs with various bandgap energies ranging from 0.84 eV to 1.37 eV could be synthesised using this new method. The synthesis of highly mono-dispersed QDs is of paramount importance for the improvement of solar cell efficiencies. This is because the QDs with a narrow size distribution ensures uniform optical properties and efficient charge transport, which resulted in the reduced recombination caused by defect sites.

Using QDs with a narrow size distribution with various bandgap energies, I have fabricated and characterised a single junction QDSC and its performance through which it was possible to understand the trade-off between the J_{sc} and the V_{oc} in a QDSC. In addition, it was possible to fabricate a multi-junction QDSC using three different sizes of QDs, which was attributed to the uniform distribution in the QD size. Because the multi-junction QDSC was able to absorb a wider range of the solar spectrum, a significantly enhanced J_{sc} was obtained in the multi-junction solar cell, which resulted in a concomitant enhancement in the PCE (Δ7.97%), from 8.0% (the highest PCE attained by a single junction solar cell) to 8.7%. Finally, the simulation results for the application to a solar panel using a multi-junction solar cell confirmed that an improvement in the solar cell efficiency is an effective way to realize a high efficiency solar panel in the future.

3. Mechanical energy

3.1 Mechanical energy harvesting

3.1.1 Introduction

Around us, there are various kinds of mechanical energy sources which occur mainly in the form of vibrations, such as sound, wind, and biologically-driven energy through the movement of our bodies. These mechanical energy sources are abundant and omnipresent in our daily life, but most of them are wasted due to the inability to harvest this energy. Unlike photovoltaics, mechanical energy sources are less dependent upon the time and the region, which is hugely beneficial in terms of a sustainable energy supply.

After the first demonstration of zinc oxide (ZnO) nanowires for mechanical energy harvesting, the area has attracted significant research interest using nanoscale inorganic ferroelectric materials as they exhibit a high sensitivity to small amounts of energy, gentle mechanical vibrations, and a high energy density compared to previous types of energy harvesters using microelectromechanical systems (MEMS).[94-97] However, inorganic materials are not readily suitable for flexible energy harvesting devices as they have a low degree of flexibility and thus are easily breakable.[98,99] As a result, polymers, such as poly(methylmethacrylate) (PMMA), polydimethylsiloxane (PDMS), and PVDF combined with nanostructures have been employed in mechanical energy harvesting applications.[97,100] In particular, PVDF-based polymers have attracted great interest due to the remarkable material properties, such as piezoelectricity, pyroelectricity, and ferroelectricity, which makes it possible to harvest various environmental energy sources simultaneously. For instance, by exploiting pyroelectricity in PVDF films, a temperature difference can be converted into electrical energy whereas mechanical energy can be

harvested through piezoelectricity, both simultaneously.[24,101]

Currently, the reported output performance of a single mechanical energy harvester is approaching 500 Wm^{-2}, or 15 MWm^{-3} in terms of volume power density, with a conversion efficiency of approximately 70%, which is sufficient for not only powering portable electronic devices, but may also be suitable for macro-scale energy generation as well.[34,102] In addition, as PVDF-based polymers are environmentally friendly, non-toxic, and biologically non-hazardous they are also being considered for biomedical and bio-sensor applications whereby a bio-mechanical signal is used as the energy source. [103-106]

3.1.2 The principle of mechanical energy harvesting

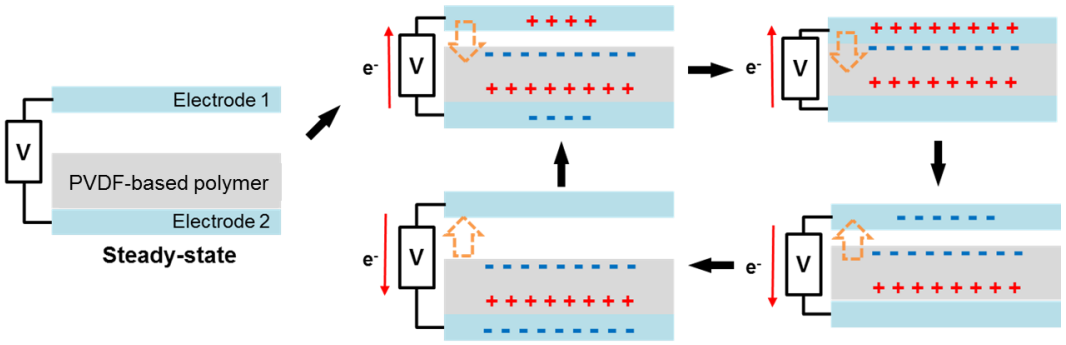

Figure 3.1: An illustration of the operating principle of a mechanical energy harvester.

Strictly speaking, the underlying mechanisms responsible for energy harvesting using piezoelectric, ferroelectric, and triboelectric effects are different from one another in the way that they induce an electrostatic potential/field to the surface of an active material. For a piezoelectric energy harvester, a surface charge is induced by the polarisation of electric dipoles upon the application of a stress/strain. On the other hand,

a ferroelectric effect induces an electrostatic field by the spontaneous polarisation of electric dipoles where as a triboelectric effect uses static charges or charges that are induced by electrification upon the contact of two materials. It is worth noting that the mechanism responsible in a triboelectric energy harvester is the same as that of a ferroelectric energy harvester because both use surface charges, which are invariable and dependent on the intrinsic surface properties of the material.

Figure 3.1 shows an illustration of the mechanical energy harvesting mechanisms. In an equilibrium state, there is no electrostatic potential/field. When pressure is applied, opposite charges are induced on the electrode due to surface charges. When the pressure is released the relative electrostatic potential difference between the active material and the contacting electrode decreases and therefore the top electrode becomes electron rich. As a result, electrons on the top electrode return back to the bottom electrode to nullify the electrostatic potential difference.

For a vertical mode energy harvester, the governing equations (3.1 and 3.2) can be described as

$$\nabla \mathrm{E} = {}^{\rho}/_{\varepsilon}\,,\ \rho = d_{ij}X \text{ for a piezoelectric harvester} \tag{3.1}$$

$$\mathrm{V} = {}^{-\rho d}/_{\varepsilon_0} \text{ for a ferroelectric (triboelectric) harvester} \tag{3.2}$$

where ρ is the charge density, ε is the dielectric permittivity, d_{ij} is the piezoelectric coefficient, X is the applied stress/strain, and d is an interlayer distance.[24] As described by the two equations, it is the charge density (ρ) that dictates the generated potential by the energy harvester. The difference is that, as explained above, the actual mechanism of how the charge is induced on the surface of the active material differs.

3.1.3 Current Challenges

Although PVDF-based polymers possess fascinating properties in terms of mechanical energy harvesting, there are still some key challenges that need to be resolved so as to make further advancement in the harvesting technology. First, PVDF-based polymers exhibit four different phases each possessing different polarisation values. In order to crystallise a polymer film into a β-phase, which has the highest dipole moment, a post-thermal annealing process is required.[107-110] However, the thermal annealing process restricts the employment of various flexible polymer substrates, which countervails one of the biggest merits of PVDF-based polymers for future flexible mechanical energy harvesting devices.

Second, it is known that an additional post-annealing process tends to make the surface rough due to the abrupt vaporization of the solvent trapped inside of the polymer film.[111] The formation of a rough surface is less favourable because the electric dipoles form along the surface normal direction and thus surface roughness results in randomly oriented electric dipoles, which results in poor device performance. Third, a polymer film with a rough surface has a greyish opaque colour, which is due to light scattering from the surface (See Chapter 5). This phenomenon restricts the integration of a mechanical energy harvester with other types of energy harvesters, such as photovoltaics, to enhance the reliability of energy harvesters by overcoming any intermittence in the environmental energy source.

Lastly, poly(vinylidenefluoride-trifluoroethylene) (P(VDF-TrFE)) generally shows a low power density, without an additional electrical poling process, and thus applications to daily life appliances have been limited. The terpolymer poly(vinylidenefluoride-

trifluoroethylene-chlorotrifluoroethylene) (P(VDF-TrFE-CTFE)), on the other hand, is known to possess high electromechanical response and elastic energy density.[112,113] However, due to its unique irreversible phase transition characteristics, the formation of a β-phase film using the P(VDF-TrFE-CTFE) polymer has received very little attention. As a result, in spite of its fascinating material properties the employment of a P(VDF-TrFE-CTFE) polymer as a promising energy harvesting material has been restricted.

In this chapter, a new method, referred to as solvent annealing is introduced to crystallise PVDF-based polymers, which is a facile, cost-effective method that can be processed at room temperature in ambient air. Attributed to the room temperature annealing process, a wider selection of polymer substrates that cannot typically sustain the relatively high post-annealing processes were now accessible. In addition, the solvent annealing method is found to form a polymer film with a smoother and flatter surface when compared with that of a thermally annealed one. The induced surface potential on the smooth surface was found to be higher than that of one with a rough surface that was formed using the thermal annealing method, which is due to the electric dipoles aligning along the surface normal. The resultant higher surface potential shows a factor of 10 improvement in the device performance when using the P(VDF-TrFE) layer.

In addition, the solvent annealing approach applied to the P(VDF-TrFE-CTFE) polymer shows a remarkable enhancement in the device performance, which is understood to be due to the irreversible phase transition of the terpolymer film. Using a solvent annealing method, it is possible to form a ferroelectric phase (β-phase) in a P(VDF-TrFE-CTFE) film that demonstrates significantly enhanced ferroelectricity compared to that of a thermally annealed one which is stabilised at an α-phase. In

accordance with the enhanced ferroelectric and materials properties, outstanding device performances of energy harvesting devices are demonstrated in this Chapter.

3.2 Fundamentals of ferroelectric & piezoelectric polymers

3.2.1 The PVDF polymer

Polyvinylidene fluoride (PVDF) and PVDF-based polymers have attracted interest for several decades as they exhibit ferroelectric and piezoelectric properties. Amongst the 32 crystal classes, 20 of these show piezoelectric properties and some piezoelectric crystals also exhibit ferroelectric properties.[114] In other words, if one material is ferroelectric then it is piezoelectric. However, piezoelectric crystals may not necessarily exhibit ferroelectric behaviour. PVDF polymer is unquestionably a unique and attractive material as it is both ferroelectric and piezoelectric when it exists in a certain phase. In different phases, however, the PVDF polymer can be non-ferroelectric and non-piezoelectric, which indicates the formation of a desirable phase is of importance in using PVDF and PVDF-based polymers for electronic applications.

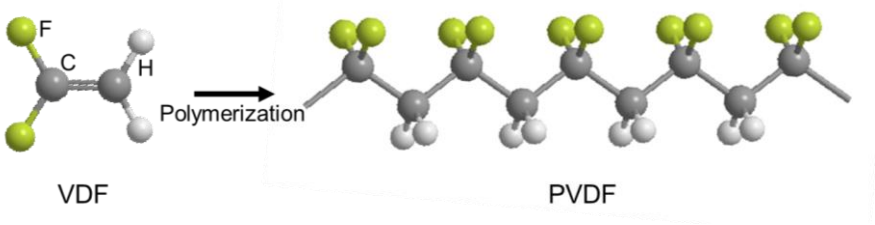

Figure 3.2: Synthesis of the PVDF polymer by a polymerisation of the VDF monomer.

Synthesis of the PVDF polymer is performed by polymerising monomer vinylidene difluoride (VDF) whereby the double carbon bonds in the VDF become a single carbon bond and thus repeating $(CH_2\text{-}CF_2)_n$ molecules are formed as illustrated in Figure 3.2.[109]

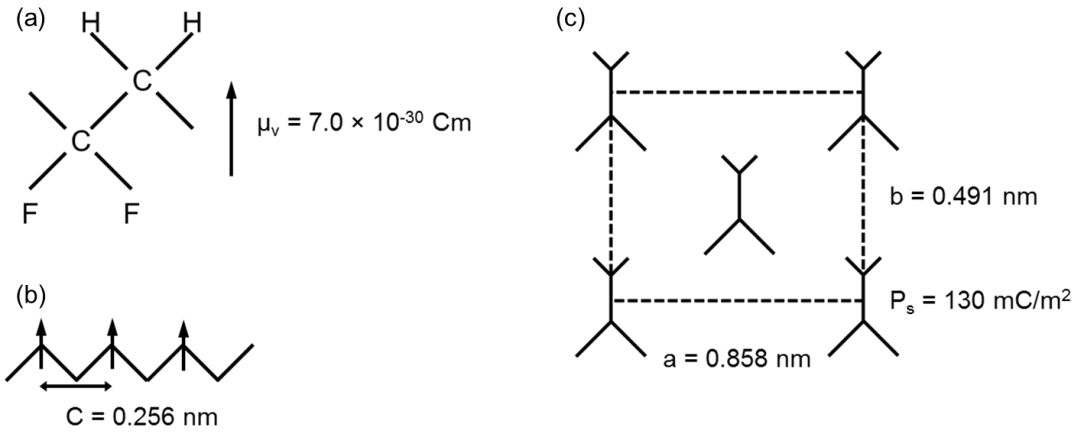

Figure 3.3: Structure of the PVDF polymer in the form of (a) a unit, (b) a molecule, and (c) a crystal.[115,116]

PVDF has three chain conformations; all-*trans*, tg^+tg^- (*transgauche*), and $tttg^+tttg^-$, depending on the torsional bond arrangements.[107-110] Among the three chain conformations, the *all-trans* conformation exhibits the highest vacuum dipole moment, $\mu_v = 7 \times 10^{-30}$ Cm per repeat whereas the tg^+tg^- and $tttg^+tttg^-$ conformations have a dipole moment that is perpendicular to the chain, $\mu_v = 4 \times 10^{-30}$ Cm per repeat, and parallel to the chain, $\mu_v = 3.4 \times 10^{-30}$ Cm per repeat, respectively. In addition, polymer chains in the *all-trans* conformation are packed in such a fashion that the chains align parallel and the dipoles point along the same direction, which results in the polar phase (β-phase). Crystalline polarisation of a polar β-phase in a unit volume is $P = 2\mu_v/abc = 130$ mC/m^2 where *a*, *b*, and *c* are the lattice constants; *a* = 0.858 nm, *b* = 0.491 nm, *c* = 0.256 nm, which is the highest among the PVDF phases.[115] In contrast, in spite of the polarity of the tg^+tg^- molecules in the non-polar α-phase, the antiparallel chain packing cancels out the net polarity, which results in the formation of a non-polar phase.

3.2.2 Piezoelectric Effect in PVDF Polymer

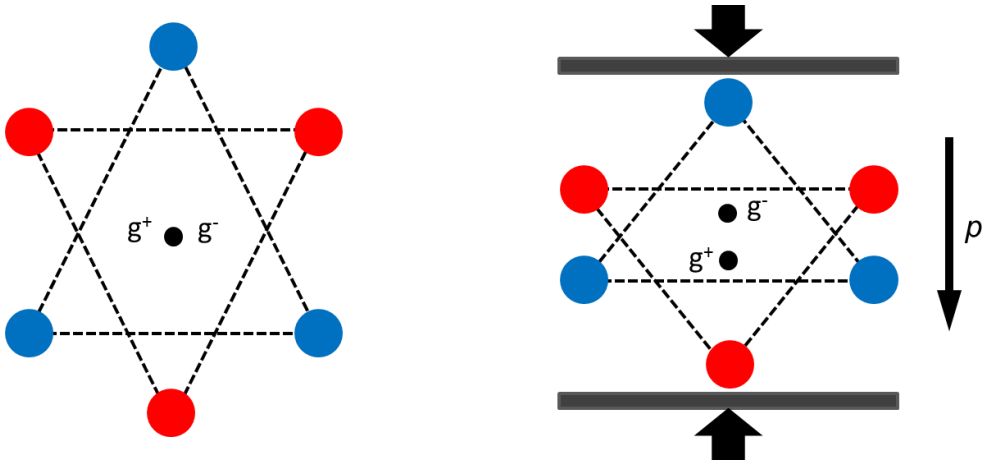

Figure 3.4: An example of the 2-dimensional view of the crystal structures of a piezoelectric material.[117]

The piezoelectric effect is the formation of a polarity across crystal boundaries upon the application of a stress/strain due to the generation of electrical charges as shown in Figure 3.4. The piezoelectric effect can be described in the form of a complex tensor matrix (see equations (3.3) and (3.4)).[117]

$$D_i = \varepsilon_o \varepsilon_{ij}^{\sigma} E_i + d_{iJ}\sigma_J \tag{3.3}$$

$$\delta_I = S_{IJ}^{E}\sigma_J + d_{Ii}E_i \tag{3.4}$$

where D is the electric displacement; E is the electric field; σ is the stress; δ is the strain; ε_o is the free space electric permittivity; d is the piezoelectric coefficient; ε^{σ} is the material's electric relative permittivity (or dielectric constant) matrix at a constant stress and S^{E} is the material's mechanical compliance matrix; I and J are indices with values from 1–6 while i and j are indices from 1–3. D and E are (3 × 1) tensors indicating the three coordinate directions x, y and z. σ and δ are (6 × 1) tensors indicating the normal stresses or strains (elements from 1–3) and shear stresses or strain (elements from 4–6).[117] However, most of the elements in the matrix are zero and thus the result is 3 or 4 piezoelectric coefficients. Among them, two piezoelectric modes are commonly used,

which correspond to the d_{31} and d_{33} coefficient.[118] The coefficient d_{31} describes the polarisation of electric dipoles perpendicular to the applied stress/strain whereas the coefficient d_{33} (longitudinal) describes the polarisation of electric dipoles along the same direction as the applied stress/strain. Table 3.1 summarises the d_{31} and d_{33} values of commonly used PVDF-based polymers.[117]

Table 3.1: Piezoelectric coefficients and other parameters of the PVDF and P(VDF-TrFE) polymers.

Parameters	Unit	PVDF[119-120]	P(VDF-TrFE)[119-122]
Density	[kgm^{-3}]	1800	1900
Young's modulus Y	[GPa]	2.5-3.2	1.1-3
Dielectric constant ε_r		12	12
Dielectric loss tan δ_e		0.018	0.018
Mechanical loss tan δ_m		0.05	0.05
d_{33}	[pCN^{-1}]	13-28	24-38
d_{31}	[pCN^{-1}]	6-20	6-12
k_{33}		0.27	0.37
k_{31}		0.12	0.07
Maximum use temperature	[°C]	90	100

3.2.3 Ferroelectric Effect in PVDF Polymer

The ferroelectric effect is one whereby the material has a spontaneous polarisation which can be reversed with the application of an external electric field.[123] The polarisation and polarisation reversal result from electric dipoles in the ferroelectric material and therefore it can be used to control the surface polarity for ferroelectric electronic applications. PVDF and PVDF-based polymers are known to exhibit the ferroelectric effect.

3.3 Properties of SA treated PVDF-based polymers

For sample preparation, the copolymer PVDF-TrFE (PVDF : TrFE = 75:25 in mole %) and terpolymer P(VDF-TrFE-CTFE) (PVDF : TrFE : CTFE = 62:31:7 in Mole %) powder were purchased from PIEZOTECH ARKEMA and both powders were dissolved in 2-Butanone (or MEK). PVDF copolymer and terpolymer solution were prepared based on a weight percent (wt%) concentration, which can be calculated as follows (3.5);

$$\text{wt\%} = {}^{powder\ mass}\Big/_{(solvent\ mass + powder\ mass)} \times 100 \qquad (3.5)$$

Throughout Chapter 3, 15 wt% of P(VDF-TrFE) and 10 wt% of P(VDF-TrFE-CTFE) solution were used for energy harvesting applications.

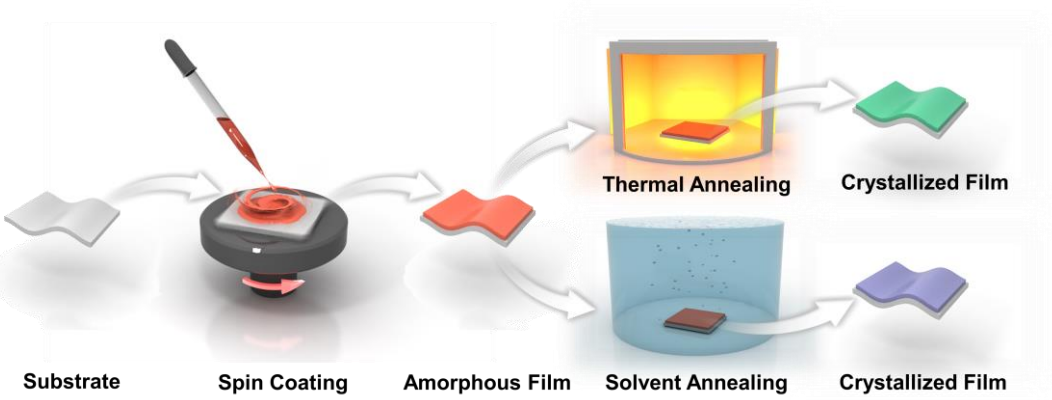

Figure 3.5: An illustration of the sample preparation procedure and the thermal and solvent annealing processes (Copyright – Appendix 1).

As illustrated in Figure 3.5, the polymer film was prepared by spin-coating the solution at 500 rpm for 10 seconds and subsequently at 3000 rpm for 40 seconds. Afterwards, the spin-coated amorphous polymer film was annealed using either the thermal annealing (TA) or solvent annealing (SA) method so as to crystallise the polymer film. TA was performed in an oven at T = 130 ℃ for 2 hours in ambient atmosphere whereas SA was carried out in a petri dish using 2-Butanone as the solvent to crystallise

the film. The optimised conditions of the SA method to crystallise polymer film were approximately 20 ~ 30 min/μm. Subsequently, the SA-treated film was dried in a vacuum chamber at room temperature for 10 hours to remove the remaining solvent. Different annealing methods did not appear to affect the thickness of the crystallised polymer film and the thickness was 4 μm for the P(VDF-TrFE) and 2 μm for the P(VDF-TrFE-CTFE) film.

3.3.1 Characterisation of P(VDF-TrFE)

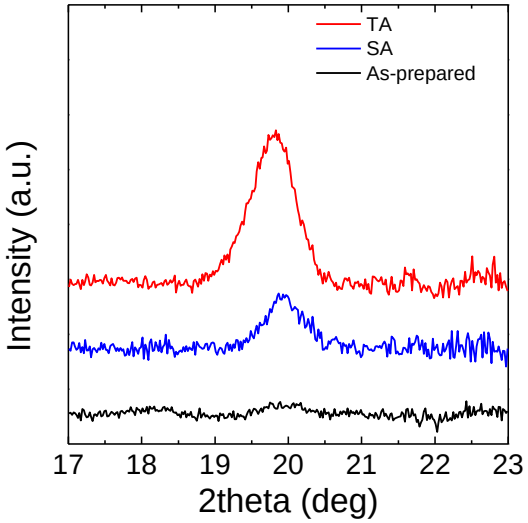

Figure 3.6: XRD measurements of the as-prepared P(VDF-TrFE) film (black), the solvent annealed film (blue), and the thermal annealed film (red) (Copyright – Appendix 1). XRD measurements were performed by the Materials Department at the University of Oxford.

Crystallised P(VDF-TrFE) films using either the TA or SA method was characterised using X-ray diffraction (XRD), Fourier-transform infrared spectroscopy (FTIR), differential scanning calorimeter (DSC), Atomic force microscopy (AFM) and surface potential. First, a XRD measurements were performed on both the SA and TA treated P(VDF-TrFE) films and exhibited a diffraction peak at $2\theta \approx 20°$, which indicates the formation of the β-phase in both films as shown in Figure 3.6.[110,124] It is worth noting

that the P(VDF-TrFE) polymer can reach up to 90% crystallinity whereas the PVDF polymer can only reach up to 50% crystallinity, which means that the P(VDF-TrFE) film is able to induce a higher electric dipole polarisation compared to that of the PVDF polymer. This high dipole polarisation field is beneficial for piezoelectric/ferroelectric electronic device applications, such as energy harvesting devices.[115]

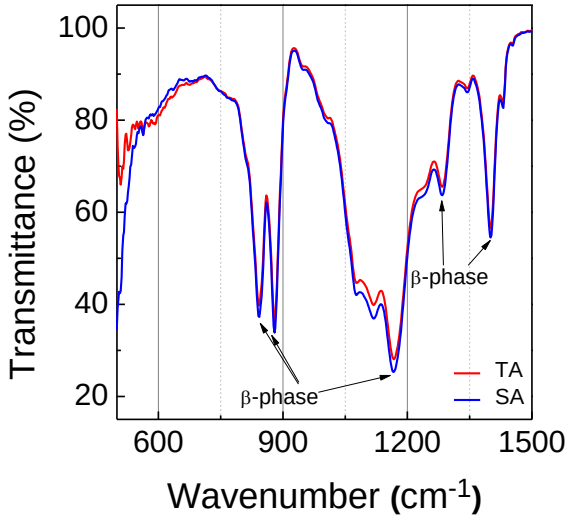

Figure 3.7: FTIR spectra of a TA-treated P(VDF-TrFE) film (Red) and an SA-treated P(VDF-TrFE) film (Blue).

To further confirm the phases of a TA- and SA-treated P(VDF-TrFE) film, FTIR, which is one of the powerful techniques to measure the molecular vibration spectrum, was used. For the case of the P(VDF-TrFE) film, molecular vibrations at wavenumbers of roughly 840, 880, 1170, 1290, and 1400 cm^{-1} are associated with the β-phase whereas wavenumbers at approximately 530, 614, 765, 795, and 976 cm^{-1} are related to the α-phase.[125,126] Figure 3.7 shows FTIR absorption bands of the P(VDF-TrFE) film which was treated using either the SA or TA method. Consistent with XRD measurement results, both the SA and TA treated P(VDF-TrFE) films exhibited the formation of a β-phase whereas molecular vibrations associated with the formation of an α-phase were not

noticeable, which indicates that both methods were effective in forming the β-phase.

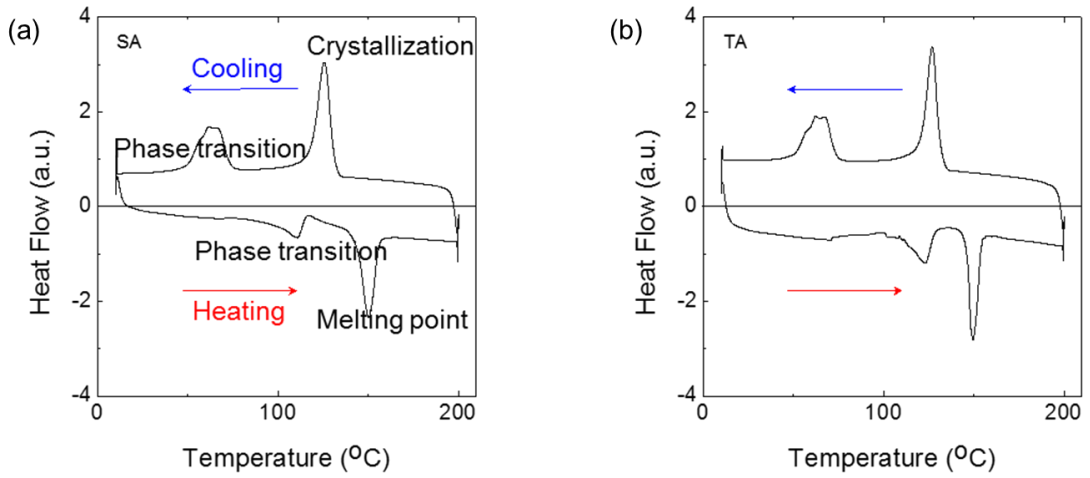

Figure 3.8: The first heating and cooling cycle from DSC measurements on (a) an SA-treated P(VDF-TrFE) film and (b) a TA-treated P(VDF-TrFE) film. DSC measurements were performed by the operator in the Materials Department at the University of Oxford.

DSC analysis was followed the XRD and FTIR measurements. First, the temperature was stabilised at T = 10℃ for 2 minutes and then raised to T = 250℃ at a ramping rate of 10℃/min. Once the temperature reached T = 250℃, it was held there for 2 minutes. For the cooling process, the temperature was lowered to T = 10℃ at a rate of 10℃/min. As shown in Figure 3.8, there are two endothermic peaks at approximately T = 110°C and T = 150°C during the heating process, which corresponds to the Curie temperature (T_c), or phase transition temperature, and the melting temperature (T_m), respectively. The observance of T_c indicates that both the SA and TA treated P(VDF-TrFE) films were in a ferroelectric phase as the phase transition occurs from the ferroelectric to paraelectric phase. The DSC results are consistent with the XRD and FTIR results, which further confirms that both annealing methods are able to form the polar β-phase.[127,128]

It is shown that a polar β-phase can be formed using both the SA and TA annealing methods as confirmed using three different types of experimental analysis. However, it is worth noting that the SA method is a more desirable process than the TA method as it can be carried out at room temperature. Also, the room temperature SA method offers access to a wider range of flexible polymer substrates selections that are not compatible with high temperature annealing processes. So far, I have highlighted the merits of the SA method from a fabrication point of view. The benefits of the SA method in terms of device performance will be discussed in a later section.

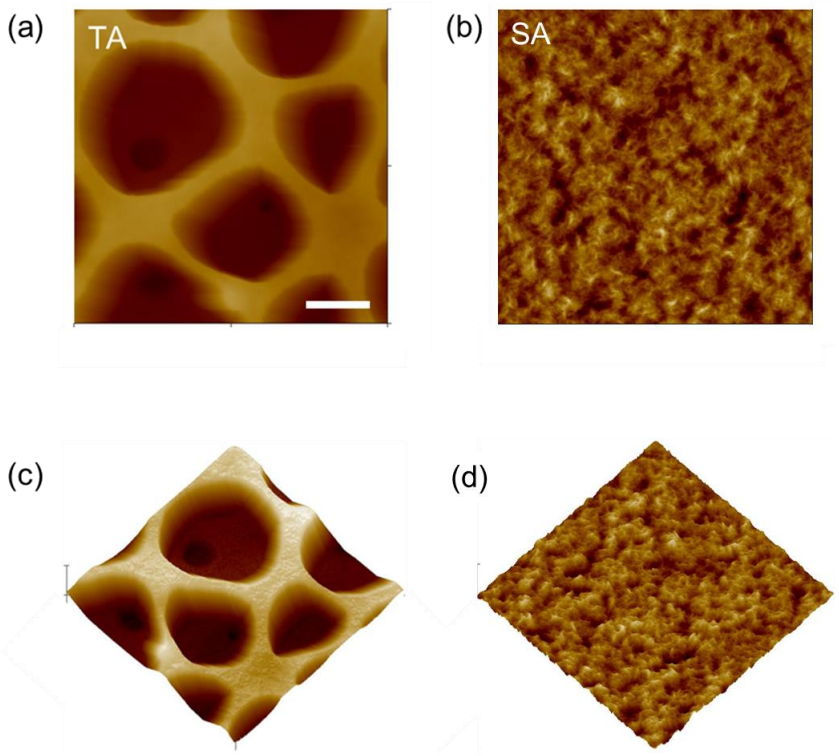

Figure 3.9: 2-dimensional AFM images of (a) a TA-treated P(VDF-TrFE) film and (b) an SA-treated film and 3-dimensional AFM images of (c) a TA-treated P(VDF-TrFE) film and (d) an SA-treated film (Scale bar: 1 μm).

In contrast to the XRD and FTIR measurements that provide crystal and molecular information, respectively, AFM is an effective tool for measuring the surface morphology

on the nanometer scale. Although both the TA- and SA-treated P(VDF-TrFE) films were in the β-phase, the surface of each polymer film exhibited significantly different profiles. As shown in Figure 3.9, the TA-treated film was extremely rough (a root-mean-square roughness: 184.11 nm) and highly porous, which can cause the frequent failure of devices due to shorts and poor performances. On the contrary, the SA-treated film revealed a flat and smooth surface (evidenced by a root-mean-square roughness of 7.8 nm). This smooth surface is attributed to the slow crystallisation process with the SA treatment, preventing the abrupt vaporisation of solvent in the film which can form huge pores on the surface. The smooth and flat surface of the SA-treated film was able to induce a higher polarisation potential/field and thus a significant improvement in device performance was observed. This will be discussed in more detail in Section 3.4.

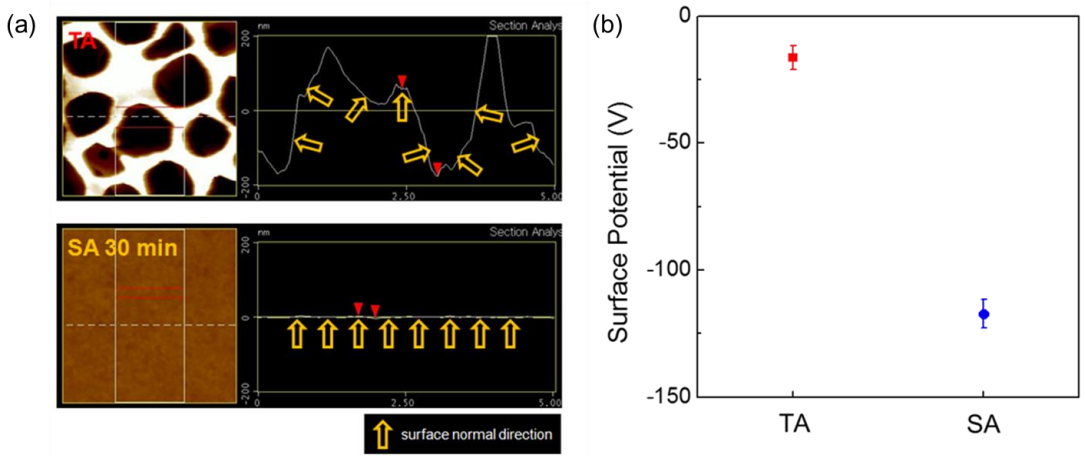

Figure 3.10: (a) Surface images and profiles of a TA-treated and an SA-treated P(VDF-TrFE) film. (b) Surface potential of P(VDF-TrFE) films treated with TA (red) and SA (blue) (Copyright – Appendix 1).

It is known that the electric dipoles in PVDF-based polymers tend to form along the surface normal and thus the surface morphology has a huge effect on the alignment of electric dipoles.[129-131] As shown in Figure 3.10(a), electric dipoles on the TA-treated film

are randomly oriented due to the extremely rough surface whereas the dipoles on the SA-treated film are well aligned along the surface normal direction. Therefore, the vector sum of the electric dipoles is higher in the SA-treated film than that of the TA-treated film. The equation (3.6) describes the field that is generated by a polarised object.[132] Considering that the thickness of the SA- and TA- treated P(VDF-TrFE) films was the same, the potential (and thus an electric field) depends on a dipole moment that is perpendicular to the integration surface.

$$\mathrm{V}(\bar{r}) = \frac{1}{4\pi\varepsilon_0}\int_{volume} \bar{\nabla}\cdot\left(\frac{1}{\Delta r}\bar{P}\right)d\tau - \frac{1}{4\pi\varepsilon_0}\int_{volume}\frac{1}{\Delta r}(\bar{\nabla}\cdot\bar{P})d\tau$$

$$= \frac{1}{4\pi\varepsilon_0}\int_{surface}\frac{1}{\Delta r}\sigma_b da + \frac{1}{4\pi\varepsilon_0}\int_{volume}\frac{1}{\Delta r}\rho_b d\tau \qquad (3.6)$$

where $\sigma_b = \bar{P}\cdot d\hat{n}$; $\rho_b = -(\bar{\nabla}\cdot\bar{P})$; σ_b is bound surface charge; $\bar{P}$ is a dipole moment; $\hat{n}$ is perpendicular to the integration surface, and ρ_b is bound volume charge.

This theoretical conjecture was confirmed by surface potential measurements using an electrostatic voltmeter (TREK 542A). The SA-treated film had a surface potential that was a factor of five larger than that of the TA-treated film, which is attributed to the well-aligned electric dipoles on the flat surface as shown in Figure 3.10(b).

3.3.2 Characterisation of P(VDF-TrFE-CTFE)

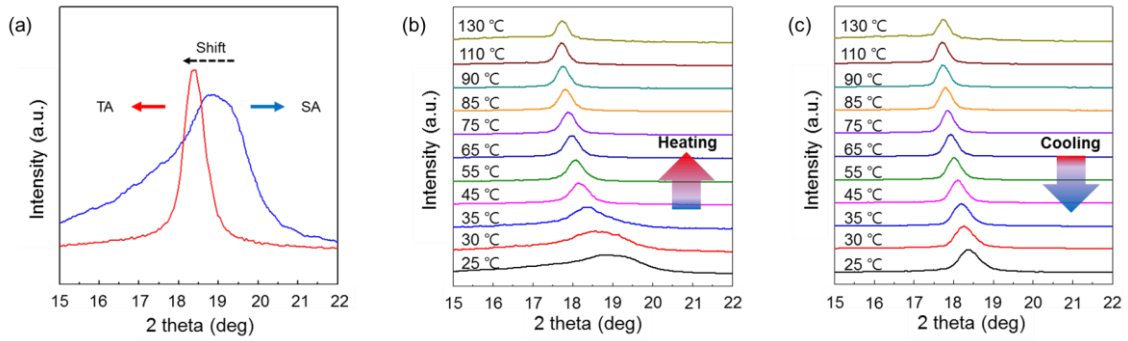

Figure 3.11: (a) *ex-situ* XRD peaks of a TA-treated P(VDF-TrFE-CTFE) (red) and an SA-treated P(VDF-TrFE-CTFE) film (Blue). *in-situ* XRD measurements during the (b) heating cycle and (c) cooling cycle (Copyright – Appendix 1). XRD was performed at the Materials Department at the University of Oxford and Dr. Ahn performed the in-situ XRD in the Pohang Accelerator Laboratory, Republic of Korea.

To characterise the SA- and TA-treated P(VDF-TrFE-CTFE) films, *ex-situ* and *in-situ* XRD measurements were performed. In contrast to the copolymer P(VDF-TrFE), it is known that the terpolymer P(VDF-TrFE-CTFE) becomes stabilised in the paraelectric α-phase once the terpolymer film undergoes a phase transition from the ferroelectric to paraelectric phase (or Curie temperature, T_c), due to its unique irreversible phase transition behaviour.[133-135] As shown in Figure 3.11, an XRD peak at approximately 18.4º was observed from the TA-treated film, which indicates the formation of an α-phase. In contrast, the SA-treated film exhibited an XRD peak at approximately 19.4º, which is attributed to the formation of a β-phase film.[136,137] The broad shoulder in the SA film is due to a small portion of the α-phase or weak long-range ordering of the terpolymer film.[134] In order to investigate the irreversible phase transition characteristics of the P(VDF-TrFE-CTFE) polymer in more detail, *in-situ* XRD measurements were carried out. For *in-situ* XRD measurement, the temperature was stabilised at T = 25 ℃ for 10 minutes.

The temperature was then raised at a rate of 10 ℃ min^{-1} for the heating cycle and cooled at a rate of 5 ℃ min^{-1} for the cooling cycle. An SA-treated film that was in the β-phase initially exhibited a shift in the XRD peak when the sample was heated. A phase transition (ferroelectric to paraelectric) was observed in the temperature range of 35 to 45 ℃. As we expected, however, during the cooling cycle the SA-treated sample did not exhibit a phase transition from the paraelectric to ferroelectric phase unlike other PVDF-based polymers. The *in-situ* XRD results confirm that the phase transition of the terpolymer P(VDF-TrFE-CTFE) is irreversible on thermal cycling.

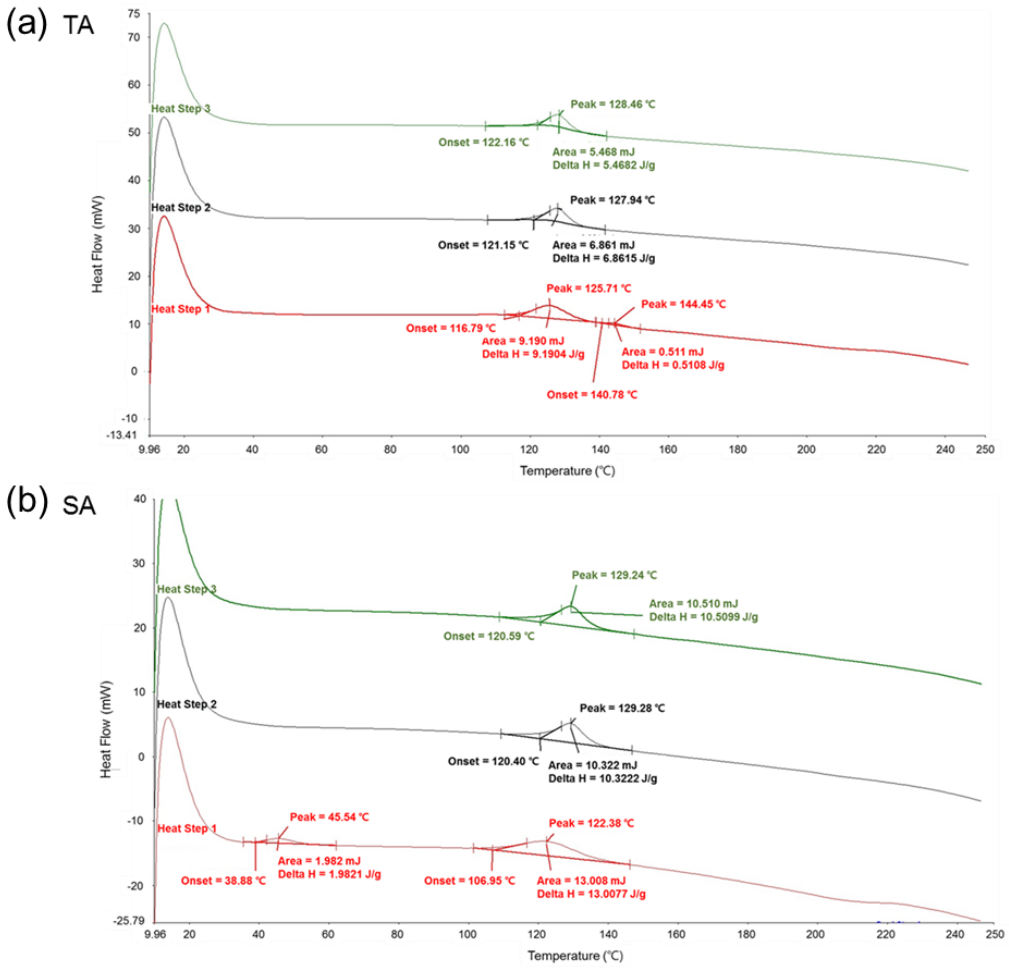

Figure 3.12: DSC graphs of three heating and cooling cycles on (a) a TA film and (b) an SA film (Copyright – Appendix 1). DSC was performed by the operator in Materials Department, University of Oxford.

DSC curves were obtained using the following conditions; first, the temperature was held at T = 10 ℃ for 2 minutes and then the temperature was raised to 250 ℃ at 200 ℃min^{-1}. Again, the temperature was held at T = 250 ℃ for half a minute and subsequently it was then cooled down to T = 10 ℃ at a rate of 200 ℃min^{-1}. As shown in Figure 3.12, the SA and TA-treated films showed noticeably different behaviour during the first cycle of the DSC analysis. The first endotherm in the temperature range of approximately 39 to 46 ℃ that was observed in the SA film is related to the phase transition temperature (T_c), where the second endotherm is referred to as the melting temperature. The observation of the F-P transition point indicates that the SA film underwent a transition from the ferroelectric phase to the paraelectric phase during the first heating cycle.[133,138] In contrast, the TA sample did not show any endotherms related to this phase transition, but only a melting endotherm, indicating that the TA film was in the paraelectric phase initially. It is worth noting that the disappearance of the phase transition point in the SA film during the second and third cycles indicates the irreversible phase transition characteristics of the terpolymer.

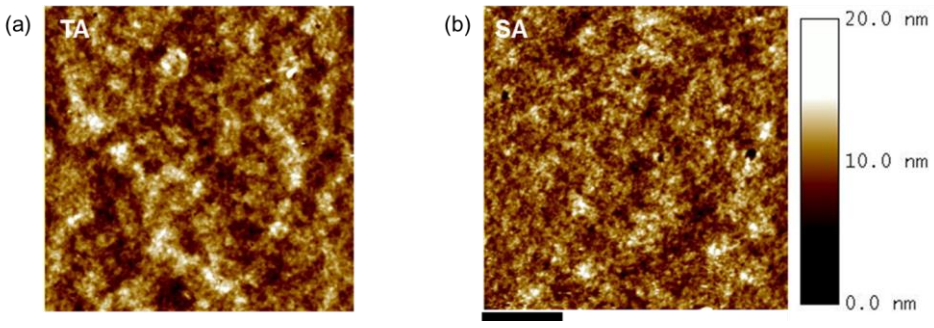

Figure 3.13: AFM surface images of P(VDF-TrFE-CTFE) that was treated by (a) a TA and (b) an SA (Scale bar: 1 μm) (Copyright – Appendix 1).

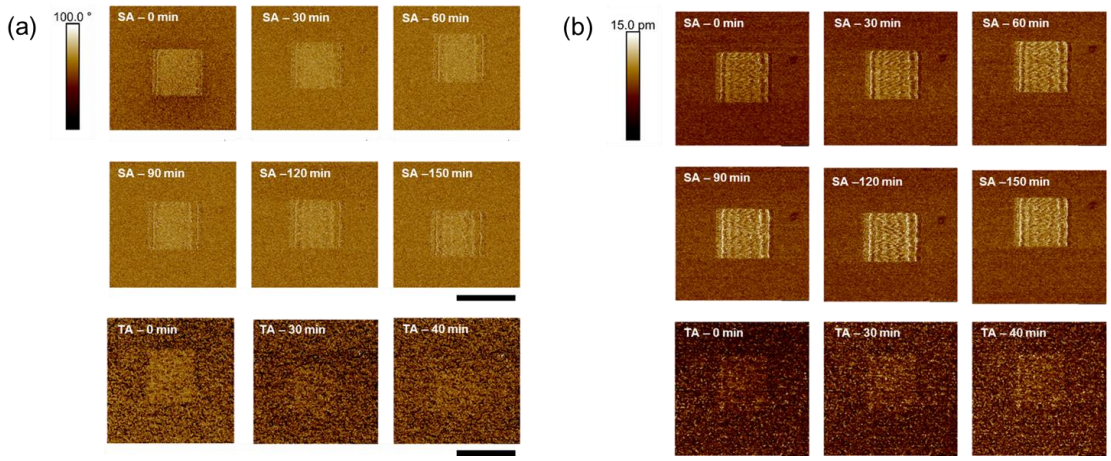

Figure 3.14: (a) PFM amplitude and (b) PFM phase images of the SA- and TA-treated P(VDF-TrFE-CTFE) films where the time-scale indicates the elapsed measurement time (scale bar: 1 μm) (Copyright – Appendix 1). Dr. Park performed the PFM measurement at the Korea Basic Science Institute, Jeonju, Republic of Korea.

In order to further confirm the formation of a β-phase in the SA film, AFM and piezoelectric force microscopy (PFM) measurements were conducted using Multimode 8 (Nanoscope V, Bruker) and the Pt/Ir coated AFM probe (SCM-PIC, Bruker). A root-mean-square surface roughness of each film was approximately 1.7 nm over 4 by 4 μm^2 area as shown in Figure 3.13. It is worth noting that the TA film was initially annealed using the SA method in order to attain smooth and flat surface because PFM signals are affected by a surface morphology of a film. To perform local poling on both the SA and TA films, a 10 V DC bias was applied to the films with a size of 1 μm^2 at a 5 ms^{-1} scan rate. After the local poling process, the PFM signals were read by applying a 2 V AC bias at a frequency of 15 kHz over a slightly larger area, 4 μm^2, at a scan rate of 5 ms^{-1}. Due to the polarisation of the electric dipoles by an external bias during the poling process, the PFM amplitude and phase measurements showed a clear difference between the poled area and a non-poled region on the SA-treated film as shown in Figure 3.14. In contrast, there was no detectable piezoelectric signal between the two regions on the TA-treated

film.

In addition, the piezoelectric response on the SA film lasted for more than 150 minutes whereas the response was no longer detectable after 40 minutes for the TA film. The long retention time of the dipole polarisation in the SA film again confirms that the SA-treated film forms a ferroelectric β-phase. On the other hand, a fast relaxation of the electric dipoles in the TA treated film suggests that the film is in a paraelectric α-phase which exhibits dipole polarisation only when the external electric field is present.

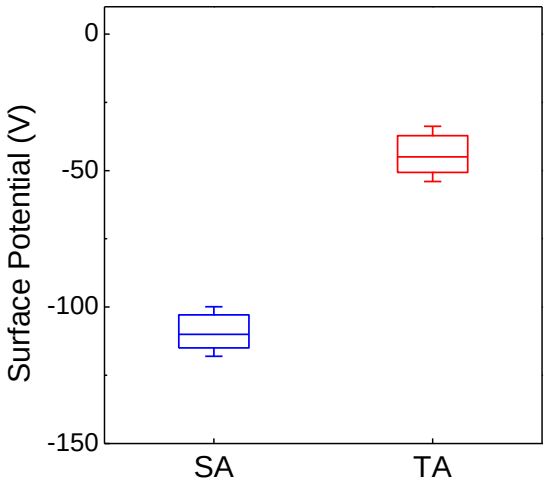

Figure 3.15: Surface potential measurements of the SA-treated P(VDF-TrFE-CTFE) film (Blue) and the TA-treated P(VDF-TrFE-CTFE) film (Red) (Copyright – Appendix 1).

Attributed to the polarisation of the electric dipoles in a ferroelectric β-phase, the surface of the SA treated film exhibits a stronger polarisation field/potential than that of the α-phase film, which is beneficial for electronic device applications, such as energy harvesting devices (Section 3.4) and ferroelectric memory (Section 3.6). Figure 3.15 shows the results of surface potential measurements. The SA-treated film exhibited a surface potential of approximately 120 V whereas the TA-treated film had a surface potential of around 45 V. This factor of 2-3 larger surface potential is attributed to the

polarised electric dipoles in the ferroelectric β-phase. Other material properties, such as dielectric constant, remnant, spontaneous polarisation and so on, for both the P(VDF-TrFE) and P(VDF-TrFE-CTFE) polymer that were provided by the material manufacturer can be found in the website of the company (PIEZOTECH).

3.4 Mechanical energy harvesting: performances

For all mechanical energy harvesting devices reported in this section, I used a flexible ITO substrate unless otherwise stated and the size of the active area was 2.5 x 2.5 cm^2. It is worth noting that the operating principle of an energy harvesting device using the triboelectric effect in this chapter is by the interaction between surface charges/potential of the PVDF-based polymer films and a top electrode, where surface charges/potential are induced by electric dipoles in the ferroelectric β-phase of the polymer films.

3.4.1 Energy harvesting output performance: Physical Effect

In order to characterise the mechanical energy harvesting device (MEH) for a piezoelectric-only coupling, a 15 wt% P(VDF-TrFE) solution was spin-coated on to an ITO substrate. To exclude any possible triboelectric effects from the top electrode, an Au electrode was directly deposited onto the spin-coated P(VDF-TrFE) film. The output characteristics for a piezoelectric-only effect are depicted by the black curve in Figure 3.16(a). The output potential of the MEH using only the piezoelectric effect was approximately 1.5 V. In contrast, a 15 times higher output potential was obtained when combining both piezoelectric and triboelectric effects. This is because, in the case of a triboelectric effect, electric dipoles in the β-phase (ferroelectric phase) film induce higher

surface potential, which results in the generation of a higher potential in the mechanical energy harvesting device by the triboelectric effect, whereas generation of the potential is determined by the dipole moment of the electric dipoles in the β-phase film, i.e. not taking into account the surface potential, in the case of a piezoelectric effect. It is worth noting that generally the piezoelectric response is relatively low compared with that of the triboelectric response as the polarisation field/potential induced by the piezoelectric effect is far smaller than that of triboelectric coupling.[139]

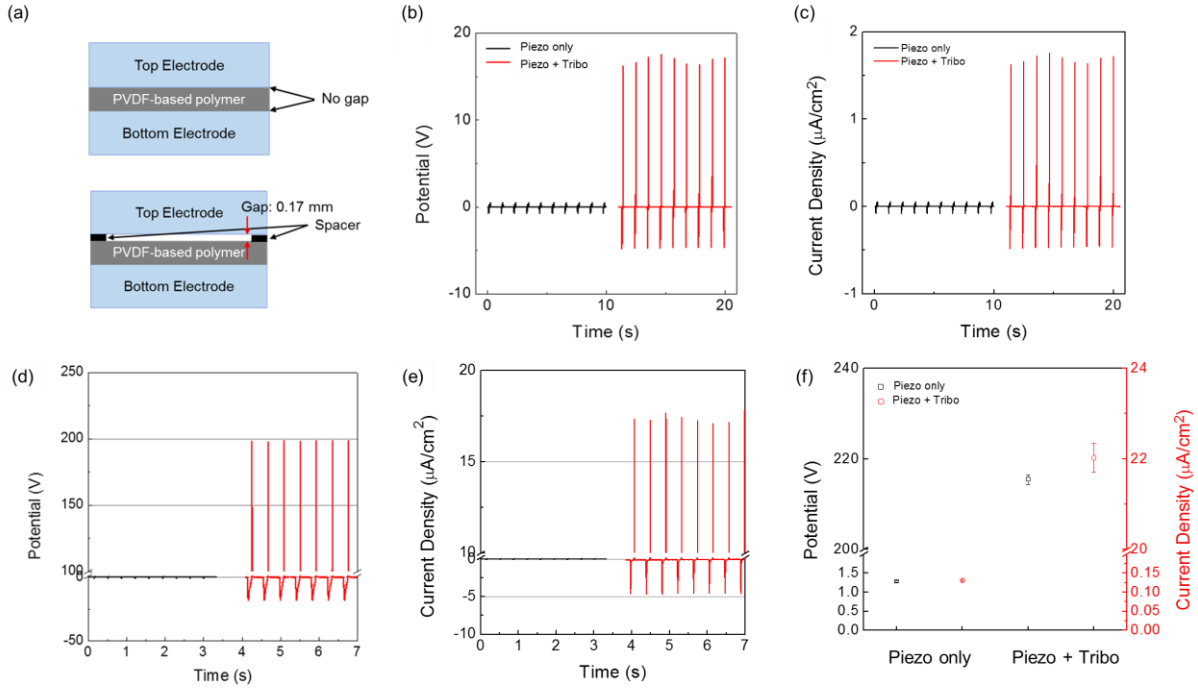

Figure 3.16: (a) Illustrations of of the device behaviour in the case of a piezoelectric effect (top) and a triboelectric effect (bottom). (b),(c) and (d)(f) Potential and current density of a mechanical energy harvester using a P(VDF-TrFE) and P(VDF-TrFE-CTFE) film (in a β-phase), respectively, where the curve shown in black is generated using only a piezoelectric effect and the curve shown in red is generated harnessing both the piezoelectric and triboelectric effects. (f) Average values with standard deviations of potential and current density shown in (b-e).

A similar phenomenon was observed in the case of the terpolymer P(VDF-TrFE-

CTFE) as that noted for the copolymer P(VDF-TrFE) as shown in Figure 3.16(b), which is again due to the high surface charge/potential of the PVDF-based polymers. Also, compared to the P(VDF-TrFE) polymer, the MEH using both effects in the P(VDF-TrFE-CTFE) film exhibited a 10 times higher potential (approximately 225 V) than that observed for the P(VDF-TrFE) film, which is because the P(VDF-TrFE-CTFE) polymer has a higher electromechanical response and elastic energy density than that of other PVDF-based polymers.[112,113]

Power density generated by energy harvesting devices was calculated by multiplying the peak value of voltage and the peak value of current density (P = VI), which was found to be 0.175 $\mu W/cm^2$ and 46.81 $\mu W/cm^2$ for only the piezoelectric effect and both effects, respectively, using the P(VDF-TrFE) copolymer. In the case of energy harvesting devices using the P(VDF-TrFE-CTFE) terpolymer, these power densities were found to be 0.170 $\mu W/cm^2$ and 4.77 mW/cm^2, respectively. However, the calculated power density can only indicate the peak power density, which is due to the output characteristics (alternative signal) of the mechanical energy harvesting devices. In order to extract the actual power that can be delivered by the energy harvesting devices, a rectifying circuit with a storage device is required to calculate the power delivered. This is discussed in Section 3.5.

Table 3.2. Average values of potential and current generated by mechanical energy harvesting devices using a P(VDF-TrFE) and P(VDF-TrFE-CTFE) film.

Samples	Effect	Potential (V)	Current density ($\mu A/cm^2$)
P(VDF-TrFE)	Piezo only	1.26 ± 0.01871	0.13934 ± 0.00105
	Piezo + Tribo	21.62 ± 0.70143	2.16498 ± 0.05062
P(VDF-TrFE-CTFE)	Piezo only	1.2932 ± 0.00550	0.13113 ± 0.00211
	Piezo + Tribo	217.146 ± 1.87568	21.9858 ± 0.28433

3.4.2 Energy harvesting output performance: Annealing Effect

In an earlier part of this chapter (Section 3.3), the SA- and TA-treated P(VDF-TrFE) films were characterised, which revealed that both films formed a β-phase. However, the surface morphology of the TA-treated film was extremely rough whereas the SA-treated film exhibited a smooth and flat surface (Figure 3.9), which affected the alignment of the electric dipoles (See surface potential measurement result in Section 3.3). As a result, the potential induced by electrostatic forces on each film was significantly different. It is worth noting that an SA-treated energy generator is denoted as a SEG and a TA-treated energy generator is denoted as a TEG, hereafter, throughout Chapter 3.

As shown in Figure 3.17(a) and (b), the TEG produced a potential and current density of around 1 V and 0.2 μA/cm^2, respectively. In contrast, the potential and current density of the SEG showed a significantly enhanced performance, approximately 11 V and 0.6 μA/cm^2. In order to confirm the importance of the smooth surface on the device performance, thermal annealing to an SA-treated film was applied. It is worth noting that the application of TA to the SA film formed a smooth and flat surface because the solvent in a polymer film was removed during SA treatment. As shown in Figure 3.17(a) and (b) by the red curve, the MEH that was treated with solvent annealing and subsequently the TA method exhibited a similar performance to that of the SEG, which indicates that the improved performance is due to the smoothing of the surface that arises from the SA treatment, not due to the different annealing method.

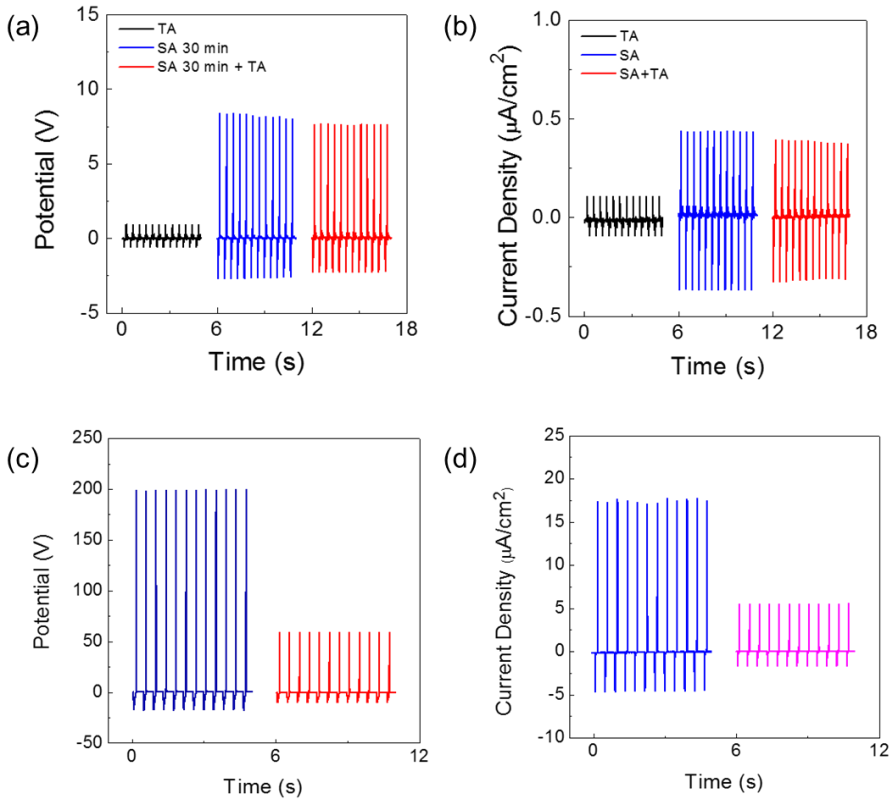

Figure 3.17: (a) and (b) MEH performances of the SEG and TEG using a P(VDF-TrFE) film. (c) and (d) MEH performances of the SEG and TEG using a P(VDF-TrFE-CTFE) film.

As I demonstrated in Section 3.3.2, the terpolymer P(VDF-TrFE-CTFE) exhibits an irreversible phase transition, which results in the formation of two different phases; the α- and β- phases for the TA-treated and SA-treated terpolymer film, respectively. As a result of the polarisation of the electric dipoles in the β-phase film, the SA-treated film exhibited a higher surface potential than that of the TA-treated film. Because the output performance of the energy harvesters depends upon the surface charges/potential (Section 3.1.2), the formation of a ferroelectric β-phase is of prime importance for energy harvesting applications using ferroelectric polymers. Figures 3.17(c) and (d) show the output performances of an SEG (blue) and a TEG (red) device. The SEG generated around 230 V and 23 μA cm^{-2} whereas the TEG generated four times less potential and current density, of approximately 60 V and 6 μA cm^{-2} by harvesting mechanical vibrations at a

frequency of 3 Hz with a pressure of 2 N cm^{-2} that was delivered by the stamping machine. The output potential and current density from the SEG were approximately 20 times higher than that of the copolymer P(VDF-TrFE) energy harvesters shown in Figure 3.17. This indicates that the terpolymer P(VDF-TrFE-CTFE) is better for energy harvesting applications than the copolymer P(VDF-TrFE), which is due to the larger electromechanical response and elastic energy density of the P(VDF-TrFE-CTFE) film compared with that of a P(VDF-TrFE) film.

3.4.3 Energy harvesting output performance: Poling Effect

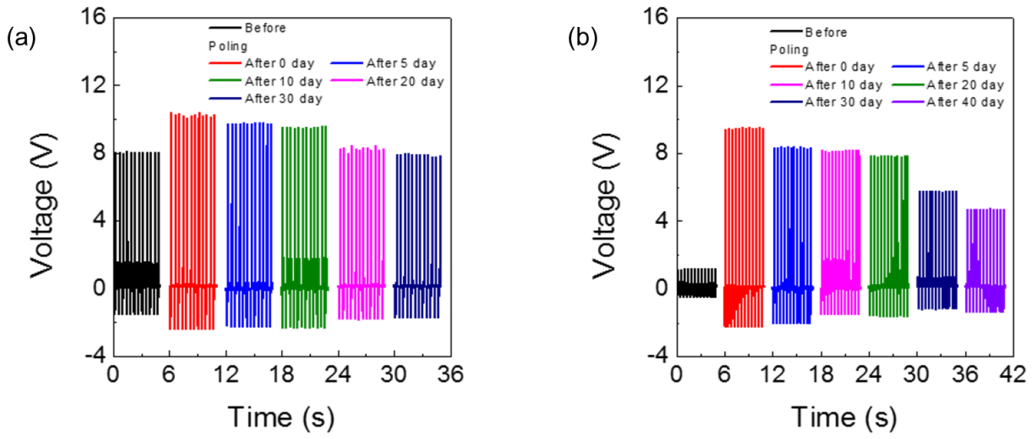

Figure 3.18: The effect of electric poling on the performance of (a) SEG and (b) TEG using a P(VDF-TrFE) film.

Electrical poling is a commonly used technique to polarise electric dipoles of PVDF-based ferroelectric polymers. Although the applied electric field and heating temperature vary depending on references, generally, the electrical poling process requires a high electric field, up to 100 MV m^{-1} and a temperature of around T = 90 °C.[110,117,140] Figure 3.18 shows changes in the energy harvesting performance after electrical poling on both the SA- and TA- treated P(VDF-TrFE) films. Consistent with the assumption based on AFM morphology and surface potential measurements, the SEG did not show a

significant improvement in the device performance whereas the TEG exhibited a substantial enhancement in the device performance. As a result, the potential generated by the TEG that was electrically poled was similar to that of the SEG. This is because the electric dipoles on the flat and smooth surface were already well aligned whereas the electric dipoles on the rough surface had to be polarised by the application of an external electric potential (electrical poling). However, due to the relaxation of the polarised dipoles, the TEG showed a prominent degradation in the device performance after 20 days as shown in Figure 3.18.

For the case of the P(VDF-TrFE-CTFE) polymer, the electrical poling process was not applicable because the application of a heating process on the P(VDF-TrFE-CTFE) film results in a change in phase of the film, leading to the formation of an α-phase. This, in turn, negated the use of the electrical poling process as the α-phase P(VDF-TrFE-CTFE) is paraelectric which shows a spontaneous polarisation only when an external bias exists. In addition, the α-phase P(VDF-TrFE-CTFE) showed a poor device performance compared to the β-phase P(VDF-TrFE-CTFE) film as discussed in Section 3.4.2.

3.5 Demonstrations & Applications

For practical electronic device applications, a minimum power is required to operate the devices. As seen in the previous sections, the output performances of the P(VDF-TrFE)-based energy harvesting devices were not sufficient to operate any electronic devices. Therefore, the terpolymer P(VDF-TrFE-CTFE) film was used for applications in charging energy storage devices and for generating optical signals using light emitting diodes (LEDs) that were controlled by a relay switch.

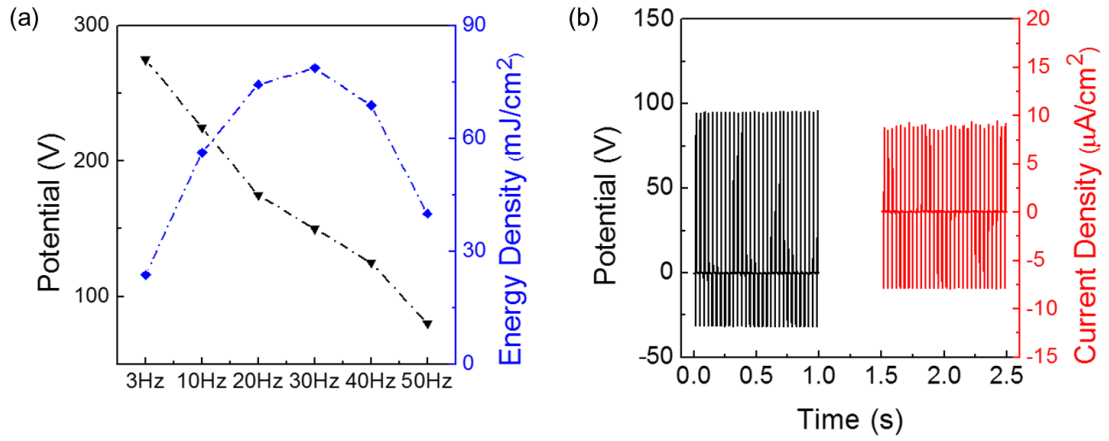

Figure 3.19: (a) Voltage (primary axis) and calculated energy density (secondary axis) at different input frequencies. (b) Voltage (primary axis) and current density (secondary axis) of the SEG that was driven at an input frequency of 30 Hz (Copyright – Appendix 1).

In order to further maximise the output power of the MEH using a SA-treated P(VDF-TrFE-CTFE) film, I first optimised the output performance by increasing the input frequency. Frequency-dependent device performances were carried out using a linear motor that can control the frequency from 1 to 1000 Hz (H2W technologies). Figure 3.19(a) shows the output potential and energy density with respect to various applied frequencies. As the input frequency increased the charge generation rates increased, and consequently the output power was enhanced. The maximum potential and energy density were obtained at a frequency of 30 Hz and the potential and current density at that frequency are shown in Figure 3.19(b).

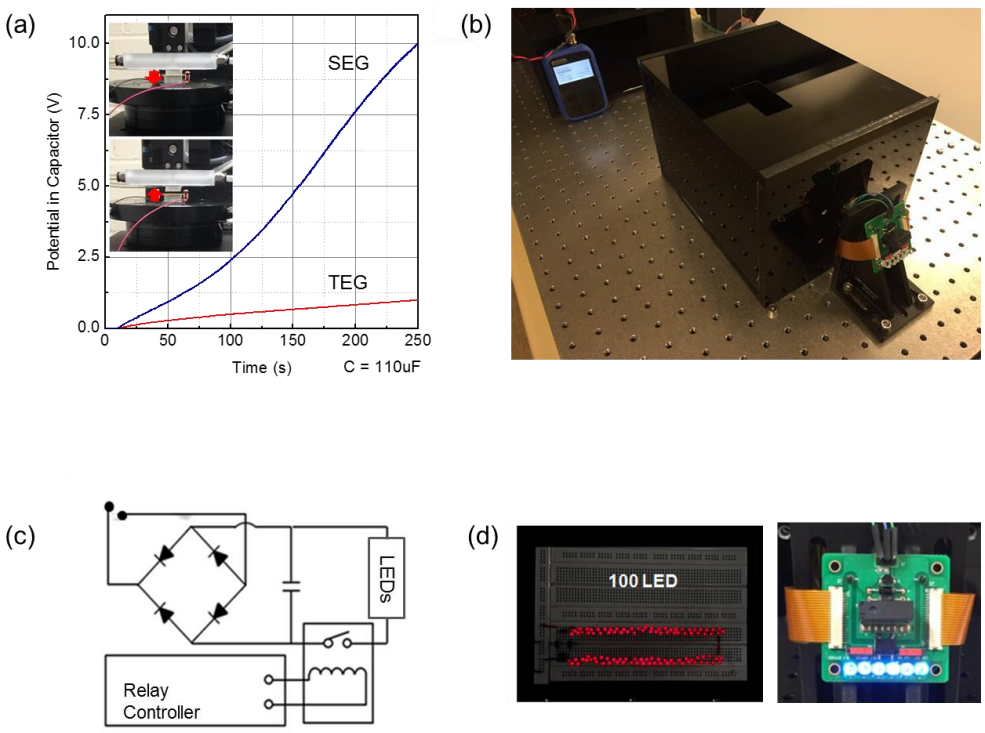

Figure 3.20: (a) Potential reached in the capacitor by the SEG (blue) and TEG (red). (b) Equipment setting for demonstrating the MEH performance and applications. (c) A demonstration circuit that consists of a rectifier, a relay switch and controller, and a series of capacitors (10 µF). (d) Demonstration of the generation of optical signals using a series of LEDs (Copyright – Appendix 1).

For applications in electronic devices, the energy generated by the MEH needs to be stored in capacitors or batteries. Figure 3.20 shows the charging rates of the capacitors (five 22 µF capacitors in parallel, total 110 µF) by the SEG and TEG (in Figure 3.17). In the same time-frame (240 seconds), the SEG charged the capacitors up to 10 V whereas the TEG charged the capacitors to only one tenth of that value, which was approximately 1.1 V. The power density that was generated by each TEG and SEG was calculated by using the potential curve in Figure 3.20(a), which was found to be 0.27 µW/cm^2 and 22 µW/cm^2, respectively.

Following the capacitor charging test, the demonstration of the SEG in a practical application was carried out. Figure 3.20(b) shows the demonstration configuration for driving LEDs, which consists of a rectifying circuit, a relay switch and controller, and a series of capacitors (10 μF) as shown in Figure 3.20(c). The SEG driven at a frequency of 30 Hz generated enough power to turn 100 red LEDs on in dark conditions and also light 6 blue LEDs so that they were visible in ambient room lighting conditions as shown in Figure 3.20 (d).

3.6 Applications to a ferroelectric memory device

As described in Section 3.3.2, the P(VDF-TrFE-CTFE) film treated with the SA process showed the formation of the ferroelectric β-phase. The demonstration of a ferroelectric memory device was also performed using a P(VDF-TrFE-CTFE) film (at a concentration of 4 wt% with a thickness of 400 nm) as a ferroelectric memory device is of considerable interest amongst the electronics research community. Prior to the investigation of a memory device, I first characterised the performance of a field effect transistor (FET) using an indium zinc gallium oxide as the channel.

As shown in Figure 3.21, an IGZO FET (channel length and width were 5 and 8 μm) showed 6 orders of magnitude for the on-off ratio with a threshold voltage at approximately −11 V. After the deposition of the β-phase P(VDF-TrFE-CTFE) film on the IGZO channel, a shift in the threshold voltage was observed whereas the on-off ratio of the FET remained at a similar level of around 6 orders. A slight shift in the threshold voltage was due to the spontaneous polarisation of electric dipoles on the β-phase film as well as a passivation effect of the polymer film.[141-143] More information about the IGZO FET is shown in Table 3.3.

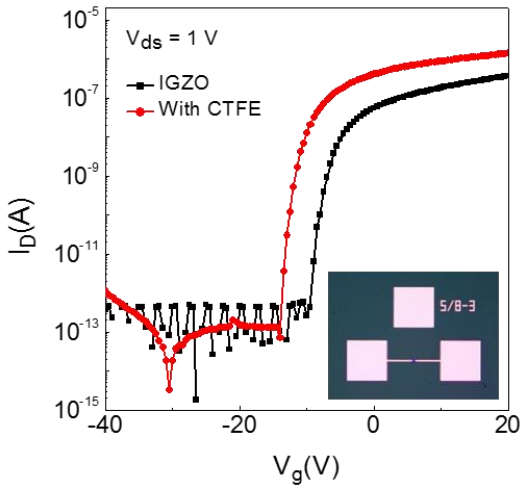

Figure 3.21: Performance of a field effect transistor (FET) before (Black) and after the deposition of a β-phase P(VDF-TrFE-CTFE) film (Red) where the channel length and width were 5 μm and 8 μm, respectively.

Table 3.3: Device parameters for an IGZO FET.

Parameters	Value
Vacuum permittivity (ε_0)	8.8540E-12
V_{ds} (V)	1.0
Dielectric Constant (ε_r)	3.9
Dielectric Thickness (nm)	200
Channel length (L) (μm)	5
Channel width (W) (μm)	8

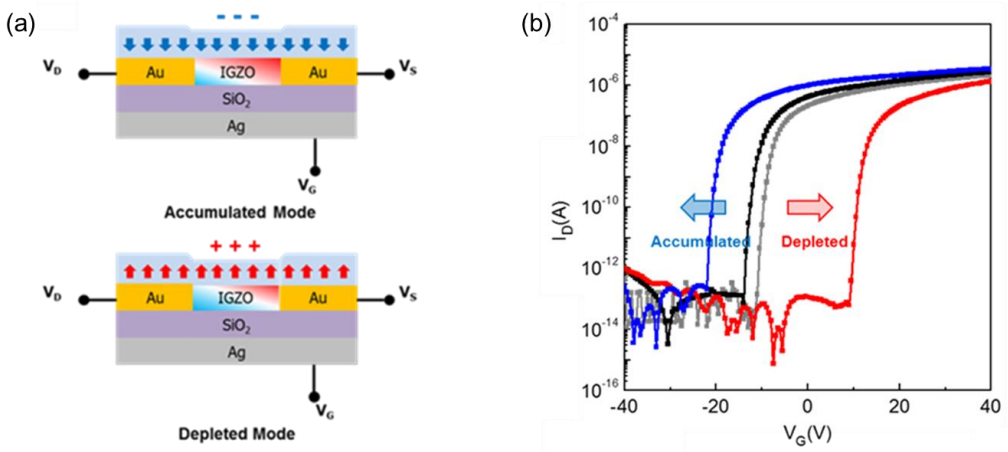

Figure 3.22: (a) Schematics illustrating the mechanism of a ferroelectric memory device. (b) Performances of a ferroelectric memory device with respect to its modes (Copyright – Appendix 1).

Figure 3.22(a) shows a schematic describing the mechanism of a ferroelectric memory device. With respect to the direction of the dipole polarisation, charge carriers in the IGZO channel are either accumulated or depleted where an accumulation mode indicates an on-state (state – 1 in digital system) and a depleted mode indicates an off-state (state – 0 in digital system) of the memory device. The direction of the dipole polarisation was controlled by performing an electric poling process. An electric potential of 80 V was applied to the P(VDF-TrFE-CTFE) film for 30 seconds at room temperature. As shown in Figure 3.22(b), dipole polarisation, negative to the surface and positive to the IGZO side, further accumulated charge carriers (electrons as IGZO is a n-type semiconducting material), which resulted in a shift of the threshold voltage (V_{th}) to more negative values. In contrast, when the dipole polarisation was aligned in the opposite direction charge carriers in the channel were depleted and thus a shift in V_{th} towards positive values was observed. A more prominent shift in V_{th} to the right of the plot is due to the fact that the electric dipoles have a spontaneous polarisation along a preferential

direction which is pointing down from the top surface. More details about the device performance with respect to the dipole polarisation direction are shown in Table 3.4.

Table 3.4: Characteristics of the device performance with respect to the dipole polarisation direction.

Sample	Mobility ($cm^2V^{-1}S^{-1}$)	Threshold voltage (V)	Subthreshold swing ($Vdec^{-1}$)
IGZO (grey)	2.9725	−10.7	0.4543
Before poling (black)	2.9656	−13.4	0.3804
Accumulated mode (blue)	3.0043	−21.6	0.4135
Depleted mode (red)	2.7470	9.9	0.4805

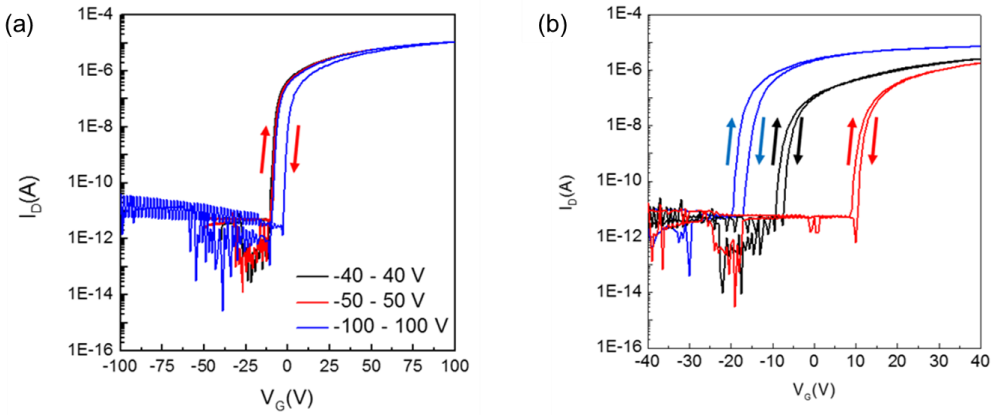

Figure 3.23: (a) Hysteresis effect of IGZO FET with respect to different gate voltage ranges. (b) Hysteresis effect of a ferroelectric memory device in the gate voltage range –40 to 40 V (Copyright – Appendix 1).

Hysteresis characteristics of the I_D-V_G curve depending on the scanning direction were investigated to confirm that the shift in V_{th} was due to the dipole polarisation of the

β-phase P(VDF-TrFE-CTFE) film and was not due to the IGZO channel. Figure 3.23 shows that the hysteresis was negligible for the memory device in the gate voltage range of –40 to 40 V where all the devices were measured, indicating that the shift in V_{th} was due to electric dipole polarisation.

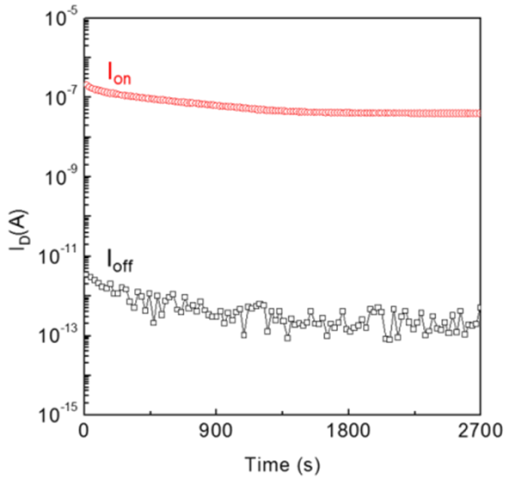

Figure 3.24: Retention performance of a ferroelectric memory device where the on and off states were read at a gate voltage of 0 V (Copyright – Appendix 1).

As shown in Figure 3.24, the memory retention time at a gate voltage of 0 V was measured and turned out to be stable for 2700 seconds (45 minutes) while maintaining a 5 order, which is attributed to the electric dipoles of the β-phase P(VDF-TrFE-CTFE) film and a large potential window (~ 35 V) of the memory device. It is worth noting that due to structural limitations (a bottom gate structure) relatively slow switching was observed (30 seconds electric poling process) and a relatively high electric potential (80 V) was applied. Therefore, further optimization is required for a high performance memory device in the future.

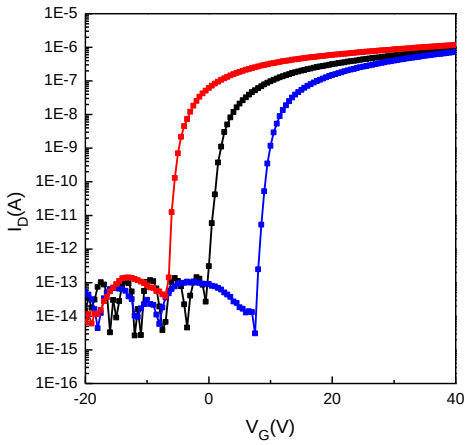

Figure 3.25: Performances (I_D-V_G curves) of a ferroelectric memory device using an α-phase P(VDF-TrFE-CTFE) film with respect to its modes where red indicates an accumulated mode and blue indicates a depleted mode (Copyright – Appendix 1).

For a comparison, a memory device using an α-phase P(VDF-TrFE-CTFE) film was also fabricated. As shown in Figure 3.25, a narrow potential range in spite of the application of electric poling was observed where the conditions were the same as for the case of the β-phase P(VDF-TrFE-CTFE) film.

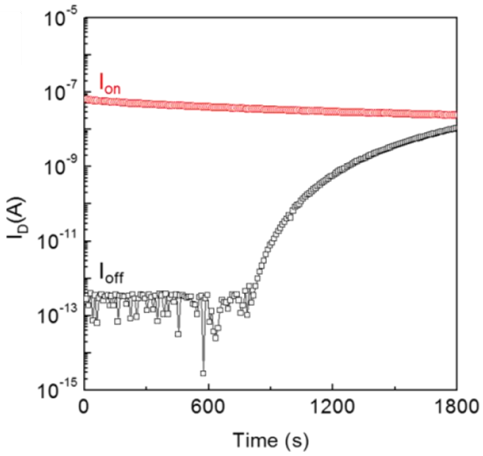

Figure 3.26: Retention performance of a ferroelectric memory device using an α-phase P(VDF-TrFE-CTFE) film where the on and off states were read at a gate voltage of 0 V (Copyright – Appendix 1).

As a result, the retention time of the memory device was found to be only 700 seconds (Figure 3.26), which was less than one third of that of the memory device using the β-phase P(VDF-TrFE-CTFE) film. This is because the α-phase P(VDF-TrFE-CTFE) film is paraelectric and thus the electric dipoles exhibit a temporary polarisation only when an external bias is applied. The above results for the ferroelectric memory devices are consistent with the findings that were presented in Section 3.3.2.

3.7 Conclusions

In the past decade, mechanical energy harvesting technology has shown an unprecedented and rapid development in device performance. Amongst the various promising materials for mechanical energy harvesting, the PVDF and PVDF-based polymers have attracted tremendous interest as they show piezoelectricity, ferroelectricity and also pyroelectricity. However, there are still a number of challenging issues that have to be resolved for further advancement, such as the formation of the most favourable phase for energy harvesting, post-annealing treatment, and an integration of the mechanical energy harvester with other types of energy harvesting devices.

In this chapter, first of all, a phase formation of copolymer P(VDF-TrFE) and terpolymer P(VDF-TrFE-CTFE) was studied and then piezoelectric and ferroelectric properties of a β-phase P(VDF-TrFE) and P(VDF-TrFE-CTFE) were characterised. As the β-phase PVDF-based polymers are piezoelectric and ferroelectric, the fabricated mechanical energy harvester (MEH) using these effects generated an electric potential when external mechanical stimuli were applied. The excellent piezoelectric response of the PVDF-based polymers to external mechanical stress/strain suggests a hybridization of PVDF-based polymers into a flexible solar cell to enhance the electric field with the

aid of the piezoelectric effect for efficient exciton dissociation and charge carrier transport, which will be discussed in Chapter 4.

Following studies on the basic properties of PVDF-based polymers, I have explored a new annealing method (solvent annealing) to address some of the challenging issues, which can be performed at room temperature and in ambient air. Therefore, this solvent annealing method offers access to a wider selection of polymer substrates that cannot typically sustain a post-thermal annealing process. Second, a solvent annealing method can form a flat and smooth surface on the P(VDF-TrFE) and P(VDF-TrFE-CTFE) films, which is favourable for the electric dipoles to align in the same direction. This is because electric dipoles tend to form along the surface normal and thus a smooth surface induces a higher surface potential due to well-aligned electric dipoles. As a result, a significant enhancement in the energy harvesting performance was observed. Thirdly, the solvent annealing method was able to change the greyish opaque colour of an as-coated P(VDF-TrFE) film into a highly transparent one, which provides a great benefit in terms of the integration of a mechanical energy harvesting device with a photon energy harvesting device (see Chapter 5).

Lastly, I have demonstrated a high performance energy harvesting device with a terpolymer P(VDF-TrFE-CTFE) film. Because the terpolymer P(VDF-TrFE-CTFE) exhibits a large electromechanical response and elastic energy density, the terpolymer is desirable for mechanical energy harvesting applications. However, typically, the terpolymer is thermodynamically stabilised in the paraelectric α-phase, which shows a spontaneous polarisation only when an external bias exists. By applying the solvent annealing method, the ferroelectric β-phase in P(VDF-TrFE-CTFE) could be formed,

which is attributed to the room temperature process that crystallises the polymer film below the ferroelectric-to-paraelectric transition point. As a result, an enhancement in device performance of more than a factor of 20 was observed when compared to that of a P(VDF-TrFE)-based energy harvesting device. This enables the generation of optical signals in LEDs using only power that was generated by the P(VDF-TrFE-CTFE) energy harvesting device.

Chapter 4. Hybrid Energy Harvesting Systems: Hybridization of Ferroelectric & Piezoelectric effects in Photovoltaics

4.1 Hybrid energy harvesting devices

4.1.1 Introduction

Harnessing sun light has been the focus of research and development for many decades, yet none of the solar cell technologies that exist, whether they are commercialised or at the laboratory research level, have reached the Shockley-Queisser limit. One of the critical reasons that they have not reached the theoretical limit is due to the inherent material-related limitations, such as the presence of defects, inhomogeneous doping levels, and non-ideal interfaces. One of the possible solutions for overcoming such limitations is the introduction of an additional layer into the device stack that can generate an electric potential, by which severe interface-related issues and charge trapping at defect sites can be resolved.[85,86,144-146] Recently, the demonstration that piezo-/ferroelectric materials can be used to overcome performance limitations has led to tremendous research interest in addressing inherent material-related problems and issues.[146-150] As a result, research has been focused not just on piezo-/ferroelectric materials for their applications to energy harvesting (Chapter 3) but also their roles in other types of energy harvesting devices, such as a solar cell.

In this chapter, I address and discuss a potential route towards enhancing the solar cell efficiency using either a piezoelectric effect or a ferroelectric effect. An additional electric field that was induced by a piezoelectric or ferroelectric effect was found to be able to modify the properties of a heterojunction between the ZnO and PbS QD layers, which resulted in a modulation of the J_{sc} with respect to the direction of the applied electric field. An electric field induced along a particular direction was found to improve

the transport of photo-generated charges and reduce radiative recombination. As a result, a significant enhancement in PCE was observed using both effects.

4.1.2 Schematics of device structure and mechanism

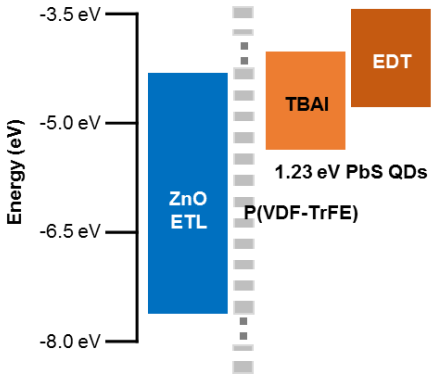

Figure 4.1: A schematic of a QDSC using a hybrid-electron transport layer consisting of ZnO and porous P(VDF-TrFE) (Copyright – Appendix 1).

Figure 4.1 shows a schematic of a QDSC with an additional piezo-/ferroelectric P(VDF-TrFE) layer so as to enhance the transport of photo-generated charges. The P(VDF-TrFE) layer was deposited between the ZnO ETL and the light absorbing QD layers. In the QDSC structure, electrons from the dissociated excitons are transferred to the ZnO ETL and holes are transferred to the EDT-treated QD layer that acts as an electron blocking (or hole transport) layer. Because the P(VDF-TrFE) layer is insulating, however, a porous structure into the polymer film was introduced to provide paths for the current. Porous structures enable photo-generated charges to be transported to the ZnO layer and also a piezo-/ferroelectric field enhances the extraction of photo-generated charges prior to recombination, which results in a significant enhancement in J_{sc} and a concomitant increase in the PCE. It is worth noting that for the study on the piezoelectric effect, a QDSC was fabricated on a flexible ITO substrate in order to be able to apply strain/stress to the QDSC. In contrast, for the study on the ferroelectric effect, a QDSC

was fabricated on a rigid glass ITO substrate in order to minimise any piezoelectric effects arising from the inherent strain/stress that would be introduced in a conformable structure.

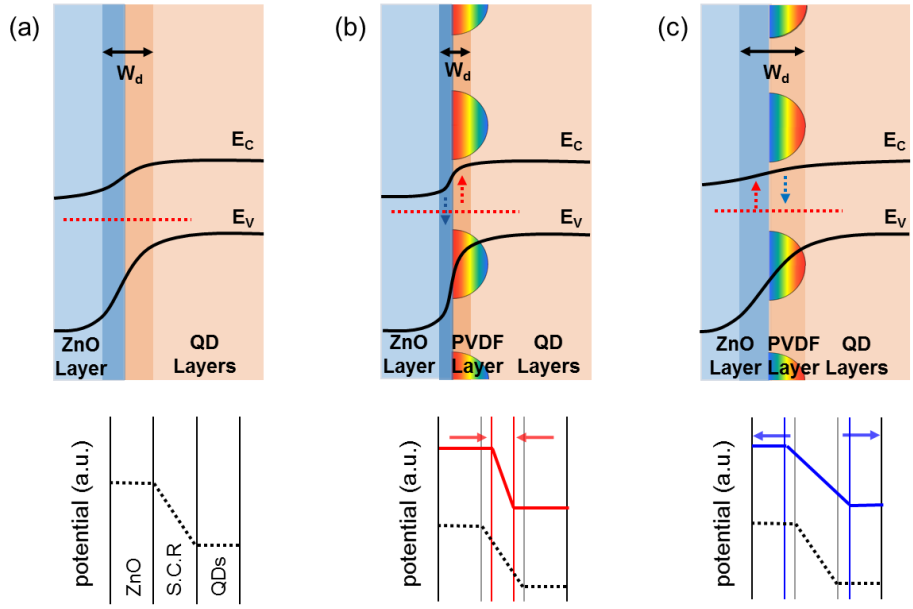

Figure 4.2: Schematics illustrating the modulation of the junction properties with respect to the direction of the induced polarisation by the piezoelectric or ferroelectric effect; (a) initial state (reference); when electric dipoles were polarised (b) positive to ZnO layer and negative to the QD layer (compressive strain) and (c) negative to ZnO layer and positive to QD layer (tensile strain). S.C.R indicates a space charge region and the potential profile was read across the ZnO-PbS QDs layers as illustrated by the red dotted line in the figure.

An illustration of the operating principle of the device is shown in Figure 4.2. A P(VDF-TrFE) layer in a QDSC induces an electric field/potential by the application of strain/stress, which leads to a modulation in the properties at the junction between the ZnO ETL and the P(VDF-TrFE) layer. In the case of the ferroelectric effect, the dipole polarisation is performed by electrical poling process and thus here I focus on the dipole polarisation by the piezoelectric effect. The application of compressive strain induces a piezoelectric-driven potential by inducing a net polarisation; negative charges towards a

PbS QD layer and positive charges towards the ZnO layer (for more detail, see Section 4.2). As a result of the induced piezoelectric potential, a higher amplitude of an electric field, or a steep electric potential, is formed at the hetero-junction, which leads to an enhancement of the exciton dissociation rates and consequently efficient charge transport. By contrast, when tensile strain is applied a lower amplitude of an electric field, or a gradual electric potential, is formed at the junction. This results in a decrease in a solar cell performance due to relatively inefficient charge carrier transport and prominent charge carrier loss by recombination.

4.1.3 Characterisation

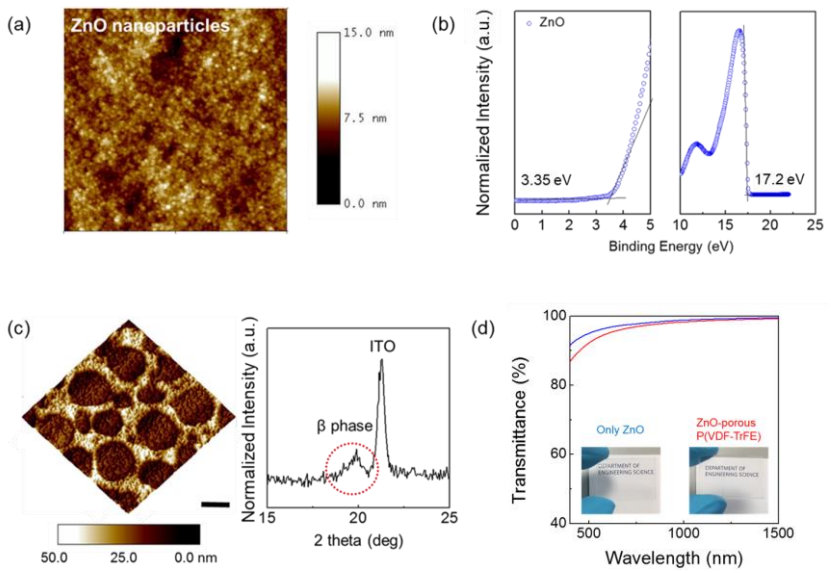

Figure 4.3: (a) AFM topography image of a ZnO layer (Scale bar indicates height profile of the surface). (b) UPS measurement of a ZnO layer where the ionization source was He I (21.2 eV). (c) 3D AFM topography image of a porous P(VDF-TrFE) layer on a ZnO layer (left) and the x-ray diffraction peak. (d) Transmittance spectrum for a ZnO layer (blue) and a ZnO-porous P(VDF-TrFE) layer (red). Insets are photographs of the ZnO and the ZnO-porous P(VDF-TrFE) layer, respectively (Copyright – Appendix 1). Dr. Yun preformed the UPS measurements at the Korea Basic Science Institute, Daejeon, Republic of Korea. And the XRD was performed in the Materials Department at the University of Oxford.

Hybrid electron-transport layers that consisted of ZnO nanoparticles and a P(VDF-TrFE) layer were spin-coated sequentially, followed by thermal annealing at T = 130℃ for 2 hours. As shown in Figure 4.3(a), an AFM image of the ZnO ETL shows a high crystallinity of the nanoparticles with a-root-mean-square roughness of approximately 2.32 nm. Also, Ultraviolet photoelectron spectroscopy (UPS) measurements (Figure 4.3(b)) revealed the Fermi, valence, and conduction energy levels of the ZnO ETL to be 4.0, 7.35, and 4.05 eV, respectively. Because the P(VDF-TrFE) polymer is an insulator, however, it cannot be used as a film structure covering the whole surface despite the high piezoelectric coefficient (d_{33} = 24 – 38 pC N^{-1} as shown in Chapter 3 Table 3.1). Therefore, a highly porous structure was introduced into the P(VDF-TrFE) layer to ensure the transport of charge carriers, as shown in Figure 4.3(c). A porous structure was formed by spin-coating a low concentration (0.5 ~ 1.0 wt%) P(VDF-TrFE) solution at high spin speeds (3000~4000 rpm). Because of the fast vaporisation of the 2-Butanone solvent, a porous structure was formed. Also, the porous structure could be controlled by changing the concentration of the solution as well as the spin-coating speed. The porous P(VDF-TrFE) layer exhibited the formation of a predominantly β-phase after thermal annealing as indicated by XRD peak at ~ 20º, which has the highest dipole moment of the relevant phases. For photovoltaic applications, light transmittance of an ETL is required to be as high as possible to ensure sufficient light absorption within the absorption layer. As shown in Figure 4.3(d), the ZnO ETL alone and our hybrid ZnO-porous P(VDF-TrFE) structure showed almost the same transmittance, which indicates that there would be negligible decrease in the solar cell performance caused by light loss. The UV-Vis measurement (Agilent Cary 5000 UV-Vis) was performed using a light source ranging from approximately 200 to 1500 nm wavelength (halogen lamp).

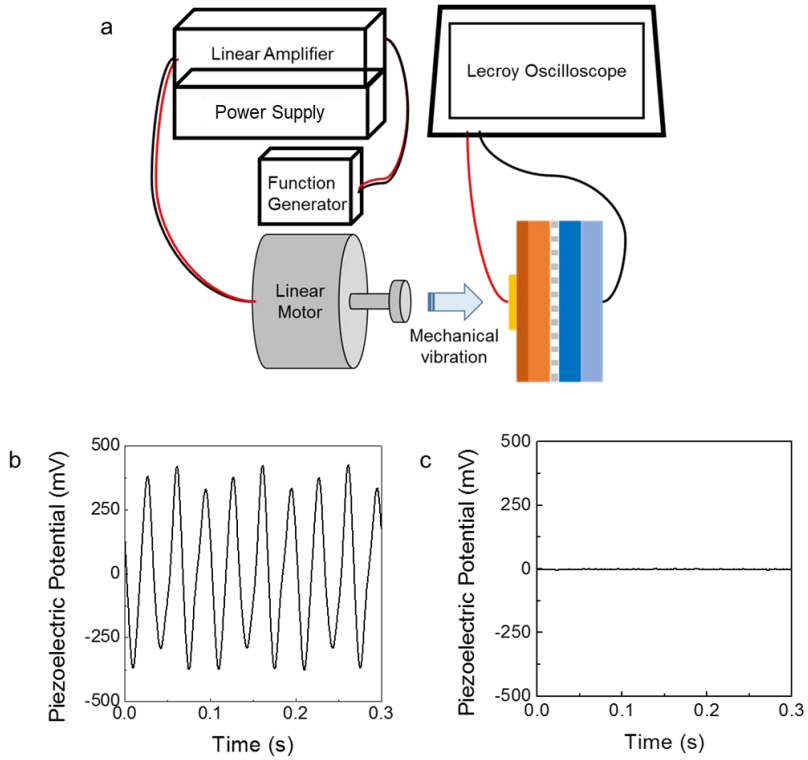

Figure 4.4: (a) The experimental apparatus for measuring the piezoelectric potential of a QDSC using a linear motor. (b) A QDSC with a ZnO-porous P(VDF-TrFE) exhibited a piezoelectric potential whereas (c) a QDSC with only a ZnO layer did not show a piezoelectric potential upon the application of mechanical vibration at an applied frequency of 30 Hz (Copyright – Appendix 1).

The piezoelectric behaviour of the porous P(VDF-TrFE) polymer in the QDSC was characterised by measuring the piezoelectric potential response to mechanical vibrations that were applied to both a QDSC with a only ZnO ETL and a QDSC with a ZnO-porous P(VDF-TrFE) ETL. The experimental apparatus is shown in Figure 4.4(a) where the applied mechanical vibration was at a frequency of 30 Hz. As shown in Figures 4.4(b) and (c), the porous P(VDF-TrFE) layer that was embedded in the QDSC generated a piezoelectric signal whereas the QDSC comprising only a ZnO layer did not exhibit any response. This further confirms that the porous P(VDF-TrFE) layer is in the β-phase and suggests that a piezoelectric-induced QDSC is potentially feasible.

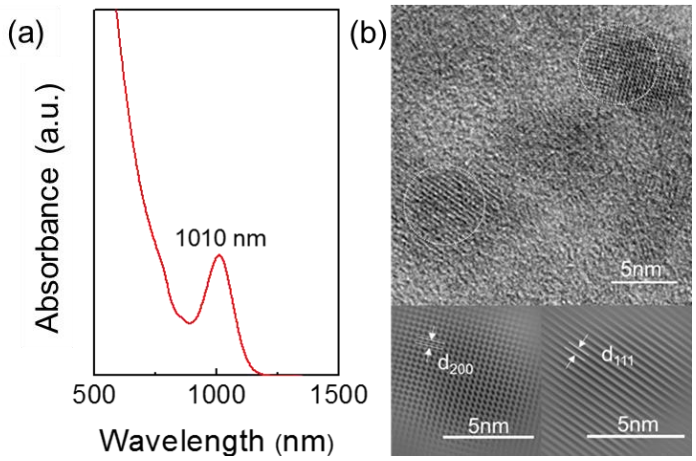

Figure 4.5: (a) Absorbance of the synthesised QDs, which revealed that the band-gap was at 1.23 eV. (b) HRTEM images of the QDs showing the typical rock-salt cubic characteristic with indices of (200) and (111) (Copyright – Appendix 1). Dr. Hou performed the HRTEM measurements in the Materials Department at the University of Oxford.

The PbS QDs that were employed to fabricate the QDSCs had a band-gap of 1.23 eV which was determined by UV-Vis measurements, as shown in Figure 4.5(a). HRTEM images (Figure 4.5(b)) show that the indices of the PbS QDs are ((200) and (111)), which indicates the typical rock-salt cubic characteristics of the synthesised QDs. Following this, ligand treatment using TBAI for the n-type layer and EDT for the p-type layer was performed in order to form a p-n junction so as to enhance the exciton dissociation (for further details on the QD analysis, see Chapter 2).

4.2 Simulations for Hybrid Energy Harvesting Systems

The piezoelectric behaviour of a porous P(VDF-TrFE) structure and the modulation of the junction properties were further explored using the COMSOL Multiphysics software. For piezoelectric materials, the following two piezoelectric equations (4.1) and (4.2) are used;[117,118]

$$\varepsilon = s_E S + d^T \boldsymbol{E} \tag{4.1}$$

$$\boldsymbol{D} = dS + \varepsilon_0 \varepsilon_r \boldsymbol{E} \tag{4.2}$$

where ε is the strain, $\boldsymbol{D}$ is electric displacement, S is stress, and $\boldsymbol{E}$ is an electric field. The material parameters s_E is a compliance, d is a coupling matrix, and ε_r is the relative permittivity, respectively, which are described in matrix form as follows.[150,151]

$$d = \begin{bmatrix} 0 & 0 & 0 & 0 & 0 & 0 \\ 0 & 0 & 0 & 0 & 0 & 0 \\ 6 & 6 & -10 & 0 & 0 & 0 \end{bmatrix} \mathrm{pCN}^{-1},$$

$$\varepsilon_r = \begin{bmatrix} 6.1 & 0 & 0 \\ 0 & 7.5 & 0 \\ 0 & 0 & 6.7 \end{bmatrix},$$

Strain (ε_x) was applied up to 1.5 % (compressive and tensile) where an initial strain tensor is described as $\varepsilon_0 = \begin{bmatrix} \varepsilon_x & 0 & 0 \\ 0 & 0 & 0 \\ 0 & 0 & 0 \end{bmatrix}$. The charge density, σ (Ccm^{-2}) induced by the piezoelectric effect was obtained by running a simulation, which were then subsequently used for the solar cell simulations.

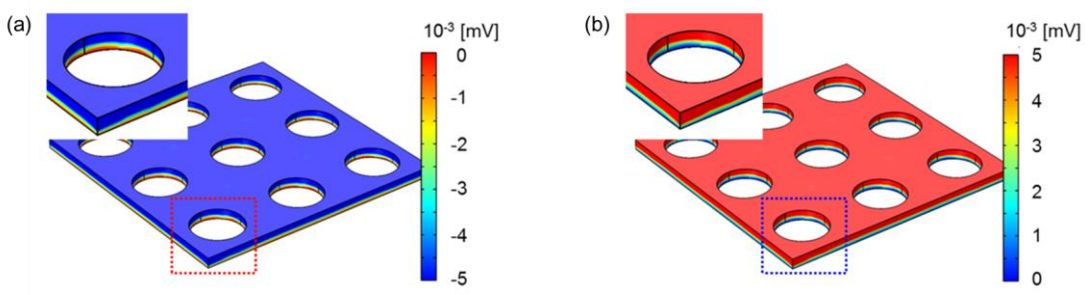

Figure 4.6: Simulation results of the piezoelectric potential induced by a net polarisation in a porous P(VDF-TrFE) layer upon the application of (a) compressive and (b) tensile strain (Copyright – Appendix 1).

Figure 4.6 shows the simulation result of a piezoelectric potential when compressive and tensile strain, each that are 1.5 % in magnitude, were applied to a porous P(VDF-

TrFE) film. Polarisation reversal was observed upon the application of a strain in the opposite direction (compressive ↔ tensile) which can be repeated continuously. The calculated charge density on the surface due to the net polarisation was approximately -2 mCm^{-2} and 2 mCm^{-2} for compressive and tensile strain, respectively.

For the solar cell simulations, the values of the parameters for the thicknesses were the same as those used in an experimental device, which were 100 nm for ZnO, 20 nm for P(VDF-TrFE) film, and 300 nm for the PbS QD film. However, in order to minimise the simulation running time, a relative P(VDF-TrFE) to QD ratio, which was 33 to 84 instead of using the same scale as the real device, was used. It is worth noting that the ZnO ETL was not considered as a piezoelectric layer because the randomly oriented ZnO nanoparticles deposited by spin-coating do not possess piezoelectric behaviour, which is also confirmed by the piezoelectric signal measurement in Figure 4.4. A doping density of PbS QDs was given as 10^{17} cm^{-3} for the acceptor and 10^{14} cm^{-3} for the donor. Other parameters for the solar cell simulation are summarised in Table 4.1.

Table 4.1: Parameters of ZnO and PbS QDs for a simulation using SCAPS software.

Parameters	ZnO	PbS QDs
Relative permittivity (ε)	66	20
Band Gap (eV)	3.2	1.3
Electron Affinity (eV)	4.3	3.9
Effective Density of states, Conduction band (cm^{-3})	1.00E+19	1.00E+19
Effective Density of states, Valence band (cm^{-3})	1.00E+19	1.00E+19
Electron Mobility ($cm^2V^{-1}s^{-1}$)	5.00E-02	2.00E-02
Hole Mobility ($cm^2V^{-1}s^{-1}$)	5.00E-02	2.00E-02

Current density ($J_{total} = J_n + J_p$) was calculated by solving the continuity equations (4.3) and the recombination rate was calculated by using equations describing band-to-band (4.4) and Auger recombination (4.5) where *b* is a radiative recombination coefficient which is 5×10^{-13} cm^3s^{-1}, and Γ_n is an Auger coefficient of electron and Γ_p is an Auger coefficient of holes, which are both 1×10^{-28} cm^3s^{-1}.[58]

$$\begin{cases} \frac{1}{q}\nabla.J_n = -G_{1.5} + R_{band} + R_{auger} \\ -\frac{1}{q}\nabla.J_p = -G_{1.5} + R_{band} + R_{auger}, \end{cases}$$ Equations for current density (4.3)

$$R_{band} = b(np - {n_i}^2)$$ Equations for band-to-band recombination (4.4)

$$R_{auger} = (np - {n_i}^2)\left(\Gamma_n n + \Gamma_p p\right)$$ Equations for Auger recombination (4.5)

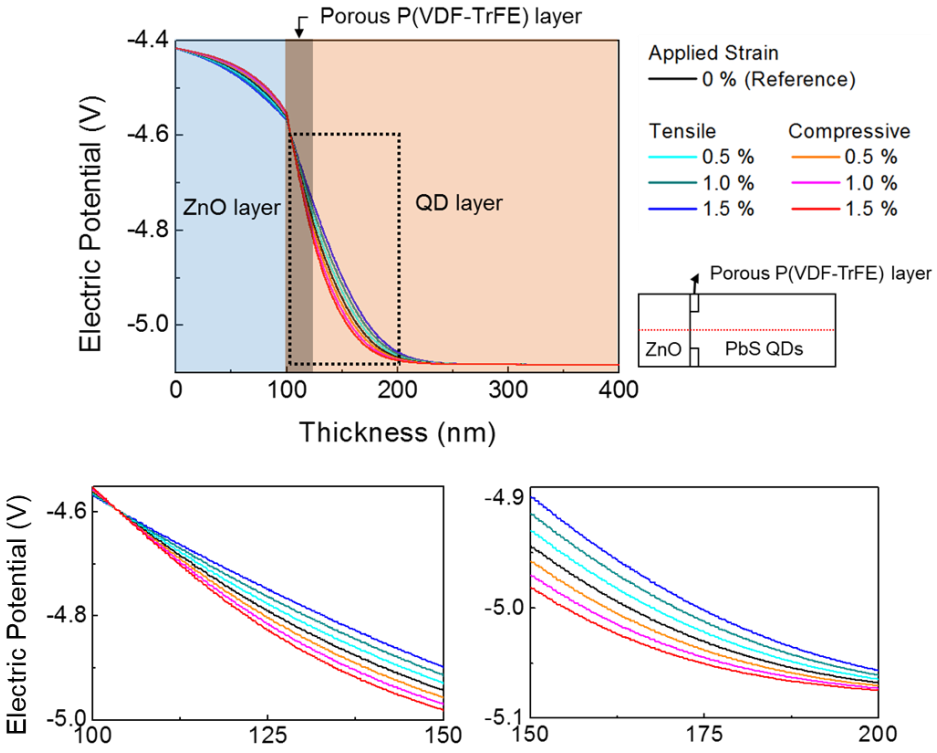

Figure 4.7: The electric potential distribution across the ZnO-PbS QD layer as indicated by the red dotted line (top right) and different strains were depicted in different colours (top right). The enlarged images illustrate the potential distribution ranging from 100 to 200 nm where the potential difference was the highest with the applied piezoelectric potential (Copyright – Appendix 1).

As the simulation results in Figure 4.7 illustrate, the modulation of the electric potential distribution throughout the QDSC was obtained by the application of various strain rates, 0 ~ 1.5 % tensile and compressive strain, which is enough to induce a piezoelectric potential. When a compressive strain was applied, the electric field at the junction increased (a steeper electric potential distribution). The generation of a high electric field enhances exciton dissociation and charge transport to the ZnO ETL. In contrast, the intensity of electric field was relatively reduced compared to no strain one (a gradual electric potential distribution) upon the application of a tensile strain, which resulted in a decrease in the exciton dissociation and inefficient charge transport to the ZnO ETL. The enhanced electric field upon the application of a 1.5 % compressive strain was 2.5×10^6 Vm^{-1} (33 % enhancement, from 7.5×10^6 (no strain) to 10^7 Vm^{-1}), which was calculated at the highest potential region around 100 ~ 120 nm.

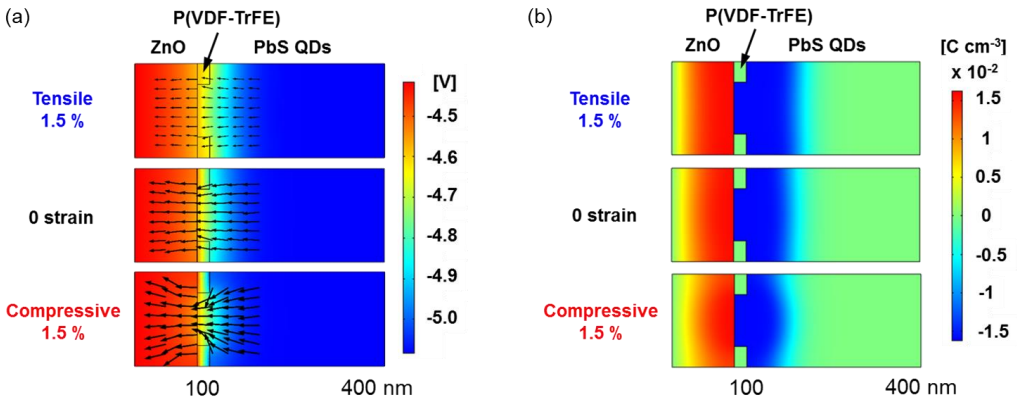

Figure 4.8: (a) A 2-dimensional view of the electric potential distribution at the ZnO-PbS QD hetero-junction for 1.5% tensile, 0 and 1.5% compressive strain, respectively. The direction of electron flow is indicated by the black arrows where the size of the arrows indicates the magnitude of the electric field at each point. (b) An illustration of the space charge region upon the application of 1.5 % tensile, 0 and 1.5% compressive strain, respectively. Positive and negative bound charge densities are depicted in red and blue colour, respectively (Copyright – Appendix 1).

The modulation of the electric potential/field by inducing a piezoelectric potential upon the application of compressive and tensile strains also affects the charge transport behaviour. Figure 4.8(a) shows the flow of electrons (given by the direction of the arrows) and magnitude of the electric field at each point. Under a compressive strain, photo-generated charges (electrons) were drawn into the pores due to the high electric field generated at the junction, which led to efficient transport of charge carriers prior to recombination at the junction. On the contrary, a diverging electric field was observed when tensile strain was applied, which resulted in the loss of photo-generated charges. The origin of the modulation of the electric potential/field is from changes in the space charge region at the junction due to an induced piezoelectric potential/field as illustrated in Figure 4.8(b). As described in Figure 4.6, the application of a compressive strain induced negative surface charges to the PbS QD layer and positive surface charges to a ZnO layer due to the electric dipole polarisation of P(VDF-TrFE) layer. As a result, the width of the space-charge region between a hetero-junction (ZnO-PbS QDs) reduced and thus generated higher electric potential than that of a hetero-junction for no applied strain. It is worth noting that even though the TBAI-treated PbS QD is an n-type semiconducting layer, this layer is relatively less n-type than a ZnO layer, in which case it can be interpreted as a junction (n^+-n-type junction, which is similar to a p-n junction in terms of physical phenomenon).[67,152]

The opposite phenomenon happens when tensile strain is applied to the QDSC; an increase in the space-charge region and thus the generation of a weak electric potential at the junction. Also, the equation (4.6) describing electric potential distribution at the junction supports the claim that the modulation of the potential distribution is due to changes in the space-charge region, where $\varphi(x)$ is a profile of the electric potential across

the junction; V_{bi} is a built-in potential, and ε_r is the relative permittivity of the semiconducting materials.[47]

$$\varphi(x) = \begin{cases} V_{bi}, \ for\ x \leq -w_n \\ V_{bi} - \frac{qN_D(x+w_n)^2}{2\varepsilon_r}, \ for -w_n \leq x \leq 0 \\ \frac{qN_A(x-w_p)^2}{2\varepsilon_r}, \ for\ 0 \leq x \leq w_p \\ 0, \ for\ x \geq w_p \end{cases} \quad (4.6)$$

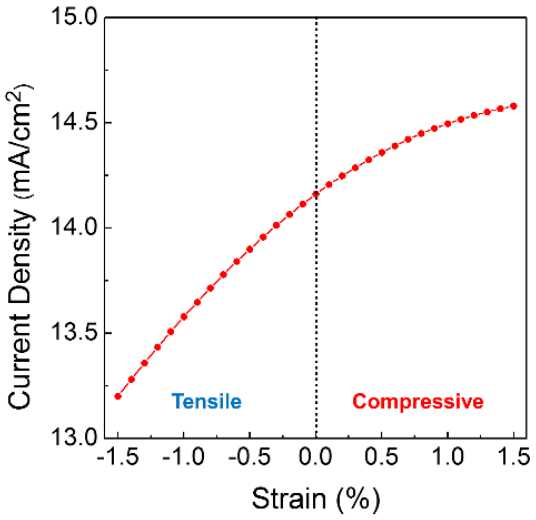

Figure 4.9: Simulation result of the J_{sc} with the application of tensile and compressive strain to the QDSC, which was performed using the COMSOL Multiphysics software (Copyright – Appendix 1).

As a result, a modulation of the photocurrent in a QDSC was observed as shown in Figure 4.9 where the photocurrent was measured and calculated by the simulation program at the terminal of a ZnO layer. The simulation results highlight that the piezoelectric potential that is induced by the application of strain can be simply reversed and, therefore, can modify the junction properties, such as the space charge region and the electric potential distribution, which consequently results in a modulation of the charge transport behaviour. Upon the application of a compressive strain, a higher electric

field is generated at the junction, which leads to a significant enhancement in the photocurrent. In contrast, the photocurrent was reduced upon the application of tensile strain because of the generation of a weaker electric field at the junction.

4.3 Piezoelectric effect in hybrid energy harvesting devices

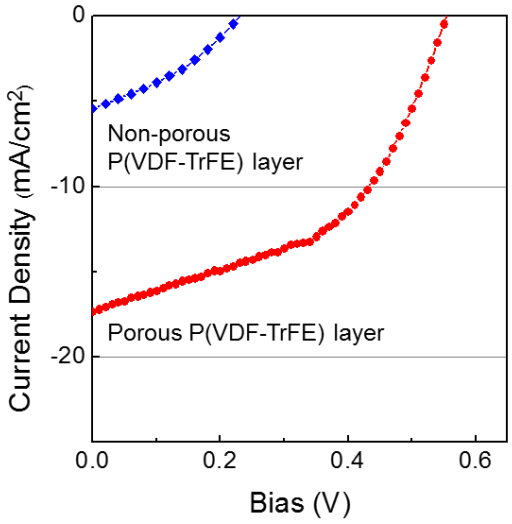

Figure 4.10: Performance of a flexible QDSC with a ZnO-non-porous P(VDF-TrFE) layer (blue) and with a ZnO-porous P(VDF-TrFE) layer (red) in the absence of any applied strain (Copyright – Appendix 1).

Prior to the investigation on the effect of a piezoelectric potential on the solar cell performance, an experiment was conducted on the importance of the porous structure in the P(VDF-TrFE) layer. As shown in Figure 4.10, a QDSC with a non-porous P(VDF-TrFE) layer exhibited poor photocurrent and solar cell performance, which is due to the insulating nature of the P(VDF-TrFE) layer which can block the transport of photo-generated charges. In contrast, a QDSC with a porous P(VDF-TrFE) layer demonstrated a much higher photocurrent, V_{oc} and FF. Considering that the thickness of both P(VDF-TrFE) layers was approximately 20 nm (Figure 4.11), this stark difference is due to whether or not there is a porous structure in the P(VDF-TrFE) layer.

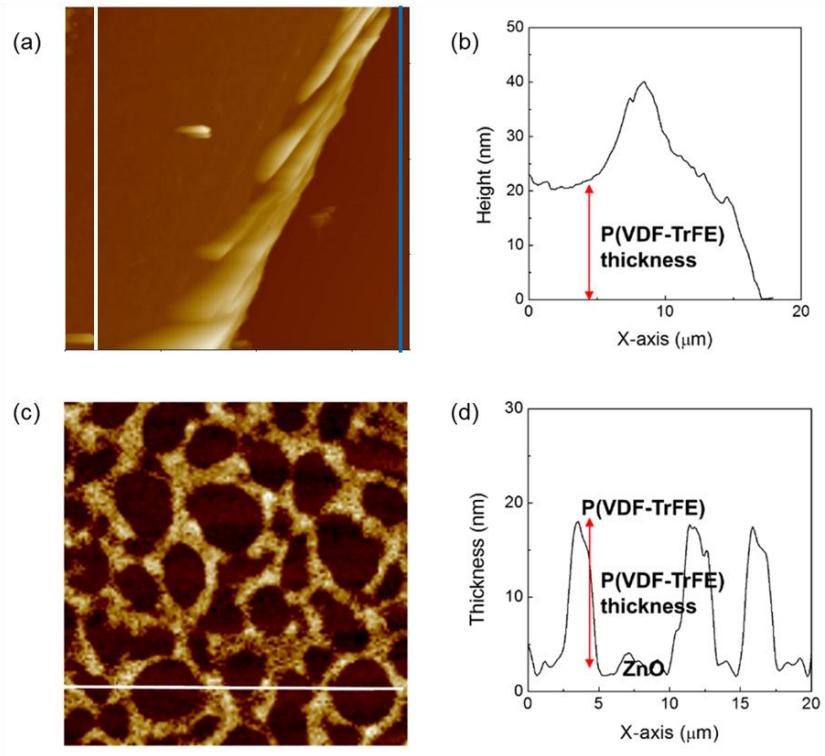

Figure 4.11: An AFM topography image (a) and thickness variation (b) of a non-porous P(VDF-TrFE) layer where the average height value was read between the white line and the blue line. An AFM topography image (c) and thickness variation (d) of a porous P(VDF-TrFE) layer where height profile was read across the white line (Copyright – Appendix 1).

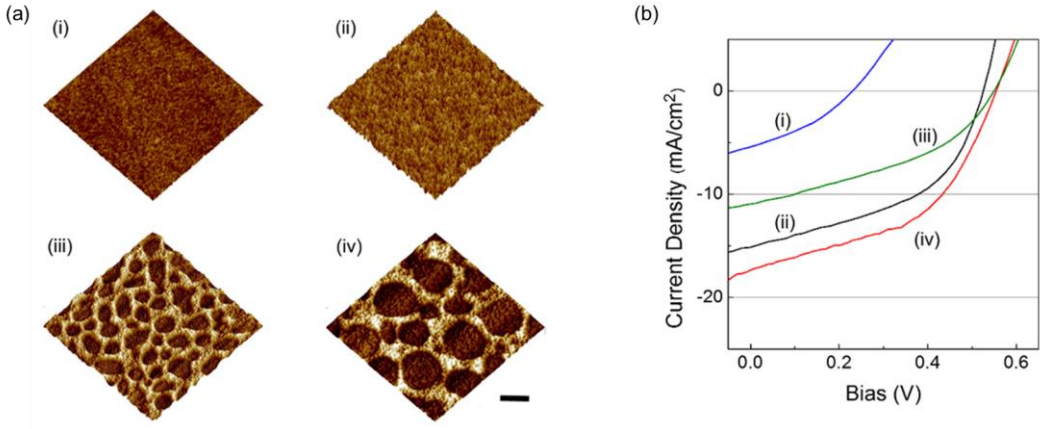

Figure 4.12: (a) 3D images taken by AFM; (i) a non-porous P(VDF-TrFE) layer (ii) a ZnO-only layer, (iii) and (iv) a porous P(VDF-TrFE) layer for different concentrations of the P(VDF-TrFE) solution (Scale bar: 1 μm for (i), (ii), (iii) and 2 μm for (iv)). (b) Performances of the QDSCs with respect to the different layers shown in (a) (Copyright – Appendix 1).

Table 4.2: Parameters of the QDSCs with the different ETLs shown in Figure 4.12.

Sample	Device structure	V_{oc}(V)	J_{sc}(mAcm^{-2})	FF	PCE (%)
(a)-(i)	ZnO-non-porous P(VDF-TrFE)	0.24	5.41	0.34	**0.44**
(a)-(ii)	ZnO-only	0.52	15.13	0.47	**3.69**
(a)-(iii)	ZnO-porous P(VDF-TrFE)	0.55	11.37	0.40	**2.50**
(a)-(iv)	ZnO-porous P(VDF-TrFE)	0.55	16.74	0.47	**4.32**

It is worth noting that the covering of the ZnO ETL by a P(VDF-TrFE) layer also affected the solar cell performance as shown in Figure 4.12, which is due to the insulating nature of the P(VDF-TrFE) layer. The results of the AFM image in Figure 4.12(a)-(iii) and the curve in Figure 4.12(b)-(iii) show that a lower solar performance is observed for a porous P(VDF-TrFE) film consisting of very small pores when compared with that of a QDSC comprising a ZnO-only ETL layer (curve (ii)). In contrast, when the pore size increases to the optimal size the QDSC exhibited an enhanced performance (curve (iv) and also see Table 4.2), which is because the transported charge carriers outnumber the number of charges blocked by the polymer layer. This is repeatedly observed in QDSCs fabricated on rigid glass substrates so as to exclude any strain effects on the solar cell performance that may arise from the flexible structure.

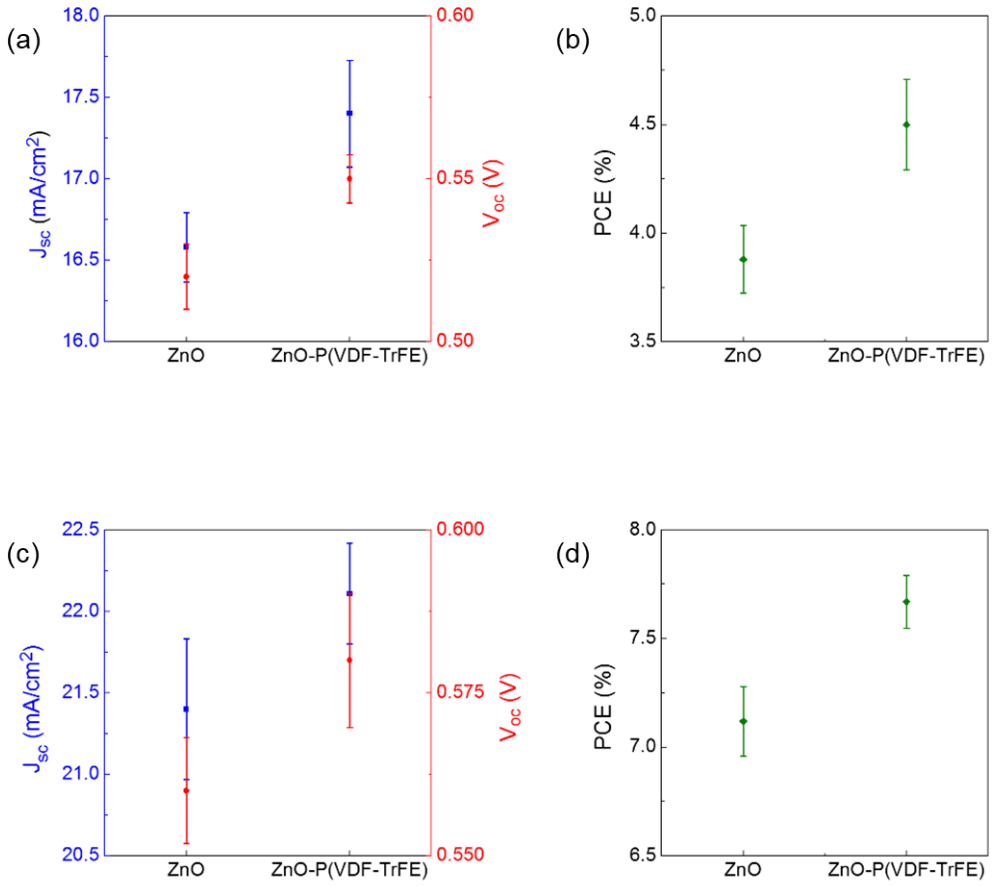

Figure 4.13: Average values for J_{sc}, V_{oc}, and PCE of PbS QDSCs with a ZnO-only layer and a ZnO-porous P(VDF-TrFE) layer on (a and b) flexible ITO substrates (c and d) rigid ITO glass substrates with no applied strain (Copyright – Appendix 1).

Table 4.3: Parameters of QDSCs shown in Figure 4.13 where Z-P ETL indicates ZnO-Porous P(VDF-TrFE) layer, T indicates TBAI-treated QD layer, and E indicates EDT-treated QD layer.

Sample	Structure	V_{oc} (V)	J_{sc} (mAcm^{-2})	FF	PCE (%)
Figure 4.13 (a) and (b)	Only ZnO-T10L/ E 2L	0.52 ± 0.01	16.58 ± 0.21	0.45 ± 0.01	**3.88 ± 0.16**
	Z-P ETL T 10L/ E 2L	0.55 ± 0.01	17.40 ± 0.33	0.47 ± 0.03	**4.50 ± 0.21**
Figure 4.13 (c) and (d)	Only ZnO-T 10L/ E 2L	0.56 ± 0.01	21.40 ± 0.43	0.59 ± 0.01	**7.12 ± 0.16**
	Z-P ETL T 10L/ E 2L	0.58 ± 0.01	22.11 ± 0.31	0.60 ± 0.01	**7.67 ± 0.12**

Figure 4.13 and Table 4.3 show the average solar cell parameters and performance without the application of strain, but only with a spontaneous polarisation of a P(VDF-TrFE) layer on a rigid ITO glass substrate to confirm the effect of spontaneous polarization on a QDSC. QDSCs reported in this chapter were made using the optimised pore sizes and distribution (Figure 4.12(a)-(iv)) unless otherwise stated.

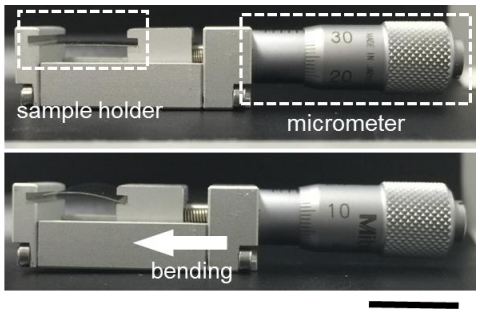

Figure 4.14: A custom sample holder for applying tensile strain to the flexible QDSCs.

The experimental verification of a piezoelectric effect on the performance of QDSCs was carried out by applying compressive and tensile strain using a homemade bending machine fitted with a micrometer as shown in Figure 4.14. The micrometer enabled us to apply strain to the layers/devices with a fine degree of control. The applied strain was calculated by assuming that the strain that was applied to a substrate was equal to the strain applied to a QDSC as the thickness of the substrate was far greater than that of the QDSC (total 500 nm).[148,152]

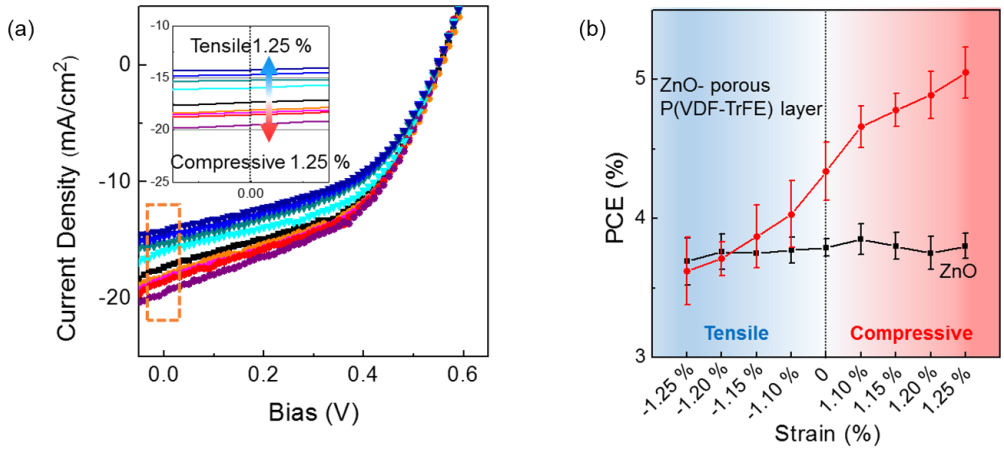

Figure 4.15: (a) Performances (J-V curves) of a QDSC with respect to the applied tensile and compressive strain, ranging from 1.10 to 1.25%. The black curve shows the solar cell performance for no applied strain. The inset shows an enlargement of the plot so that the J_{sc} level at 0V bias with respect to the applied strain can be seen. (b) The modulation in the PCE upon the application of either a tensile or compressive strain on a QDSC with a ZnO-porous P(VDF-TrFE) layer (red) whereas there was no observable modulation in the QDSC that consisted of a ZnO-only layer (black) (Copyright – Appendix 1).

Figure 4.15 shows the QDSC performance (J-V curves) with respect to an applied compressive or tensile strain, 0 ~ 1.25%. Consistent with the simulation results in Section 4.2, the application of a compressive strain led to the enhancement of J_{sc} whereas a decrease in J_{sc} was observed when a tensile strain was applied. The modulation of J_{sc} was found to be as large as 37%, from 14.18 (tensile strain 1.25%) to 19.53 mA cm^{-2} (compressive strain 1.25%), which was attributed to an enhanced exciton dissociation and charge carrier transport by the higher electric field induced by a piezoelectric effect at the junction. The experimental result is consistent with both the simulated studies shown in Figure 4.9 as well as the equation for exciton dissociation rates (K_d) (4.7) that describes the direct dependence of the exciton dissociation rates on the strength of an electric potential as shown in 4.7;

$$K_d = \frac{3R}{4\pi a^3} e^{-E_B/K_B T} \left(1 + b + b^2/3 + \cdots\right), \mathrm{b} = b^3 E / 8\pi\varepsilon_0 \varepsilon K^2 T^2 \qquad (4.7)$$

where R is the bimolecular rate constant of the bound electron-hole (e-h) pair; a is the initial separation of the bound e-h pair at the interface charge transfer exciton; E_B is the e-h pair's binding energy; and k_B is the Boltzmann constant.[153,154]

It is perhaps worth commenting that a modulation in the V_{oc} with respect to the applied strain was not significant compared to J_{sc}, which is because the induced piezoelectric potential had an effect only on an area that was adjacent to the heterojunction. As a result, the quasi-Fermi level of the whole solar cell system was not affected by the local piezoelectric potential, resulting in a modulation in J_{sc} but a negligible change in V_{oc}. The enhancement in J_{sc} led to a concomitant improvement in the PCE of the QDSC, of approximately 1.4% (from 3.68% to 5.05%) as shown in Figure 4.15(a) and Table 4.4. In contrast, the QDSC that employed a ZnO-only ETL, i.e. without a piezoelectric effect, did not show any noticeable improvement in either J_{sc} or PCE (Table 4.5).

Table 4.4: Extracted Solar Cell Performance Parameters from the QDSC that was subjected to an applied strain in Figure 4.15(a) where C and T indicate compressive and tensile strain, respectively.

Strain (%)	V_{oc} (V)	J_{sc} (mAcm^{-2})	R_s (Ωcm^2)	R_{sh} (Ωcm^2)	FF	PCE (%)
C 1.25	0.55	19.53	8.88	118.67	0.47	**5.04**
C 1.20	0.55	18.54	8.66	115.92	0.48	**4.92**
C 1.15	0.55	18.28	8.79	112.31	0.48	**4.83**
C 1.10	0.55	17.83	8.44	114.01	0.48	**4.71**
0	0.55	17.41	10.02	107.00	0.47	**4.30**
T 1.10	0.54	15.68	13.78	103.69	0.47	**4.00**
T 1.15	0.54	15.22	12.62	107.30	0.47	**3.91**
T 1.20	0.54	14.66	13.07	107.20	0.47	**3.79**
T 1.25	0.54	14.26	12.14	108.21	0.47	**3.68**

Table 4.5: Average solar cell parameters from 15 devices of a QDSC comprising a ZnO-only layer where C and T indicate compressive and tensile strain, respectively.

Strain (%)	V_{oc} (V)	J_{sc} (mAcm^{-2})	FF	PCE (%)
C 1.25	0.52 ± 0.0070	-16.55 ± 0.66	0.44 ± 0.01	**3.80 ± 0.09**
C 1.20	0.52 ± 0.0058	-16.49 ± 0.79	0.44 ± 0.01	**3.75 ± 0.12**
C 1.15	0.52 ± 0.0050	-16.70 ± 0.19	0.44 ± 0.01	**3.80 ± 0.10**
C 1.10	0.52 ± 0.0058	-16.96 ± 0.09	0.44 ± 0.01	**3.85 ± 0.11**
0	0.52 ± 0.0058	-16.65 ± 0.69	0.44 ± 0.02	**3.79 ± 0.06**
T 1.10	0.52 ± 0.0010	-16.71 ± 0.71	0.43 ± 0.02	**3.77 ± 0.09**
T 1.15	0.52 ± 0.0050	-16.10 ± 1.08	0.44 ± 0.02	**3.75 ± 0.11**
T 1.20	0.52 ± 0.0083	-16.47 ± 0.83	0.44 ± 0.02	**3.76 ± 0.13**
T 1.25	0.52 ± 0.0072	-16.03 ± 0.51	0.44 ± 0.02	**3.69 ± 0.17**

Figure 4.15(b) presents the average value of the PCE extracted from 15 devices with respect to different applied strains, which shows that the PCE changes with the amount of strain for the ZnO-porous P(VDF-TrFE) layer due to the piezoelectric effect. However, for the QDSCs with only a ZnO layer there was a negligible change in the PCE irrespective of the application of a compressive or a tensile strain. Table 4.6 summarises the results and shows other solar cell parameters. It is worth noting that any change in distance from the light source of the QDSC, which arises from the applied strain during measurements, was small, approximately 2.5 mm. Also, considering that a collimated light source was used for the solar cell measurements, a modulation in the solar cell performance and enhancement were due to a piezoelectric potential that was induced by the application of strain. Moreover, when either compressive or tensile strain was applied to the QDSC repeatedly the performance of the QDSC was reversible with a high reliability, as shown in Figure 4.16.

Table 4.6: Average parameters of QDSCs with a ZnO-porous P(VDF-TrFE) layer (Figure 4.15(b)) where C and T indicate compressive and tensile strain, respectively.

Strain (%)	V_{oc} (V)	J_{sc} (mAcm^{-2})	FF	PCE (%)
C 1.25	0.55 ± 0.0101	19.53 ± 0.72	0.47 ± 0.02	**5.05 ± 0.18**
C 1.20	0.55 ± 0.0092	18.68 ± 0.32	0.48 ± 0.02	**4.91 ± 0.17**
C 1.15	0.55 ± 0.01	18.23 ± 0.38	0.48 ± 0.01	**4.80 ± 0.12**
C 1.10	0.55 ± 0.01	17.79 ± 0.25	0.48 ± 0.02	**4.68 ± 0.15**
0	0.55 ± 0.0074	17.40 ± 0.33	0.47 ± 0.03	**4.50 ± 0.21**
T 1.10	0.55 ± 0.01	15.84 ± 0.44	0.47 ± 0.02	**4.09 ± 0.24**
T 1.15	0.55 ± 0.0095	15.28 ± 0.23	0.47 ± 0.02	**3.95 ± 0.23**
T 1.20	0.55 ± 0.0074	14.77 ± 0.27	0.47 ± 0.02	**3.80 ± 0.12**
T 1.25	0.55 ± 0.0079	14.18 ± 0.33	0.47 ± 0.02	**3.68 ± 0.24**

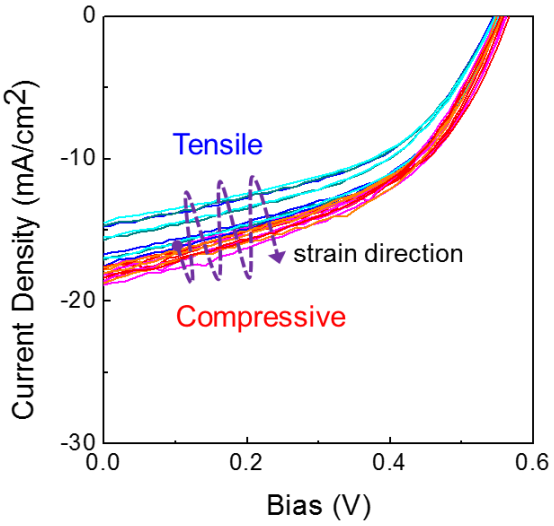

Figure 4.16: Reversibility of QDSC performance (J-V curves) when repeated compressive and tensile strain were applied to the device (Copyright – Appendix 1).

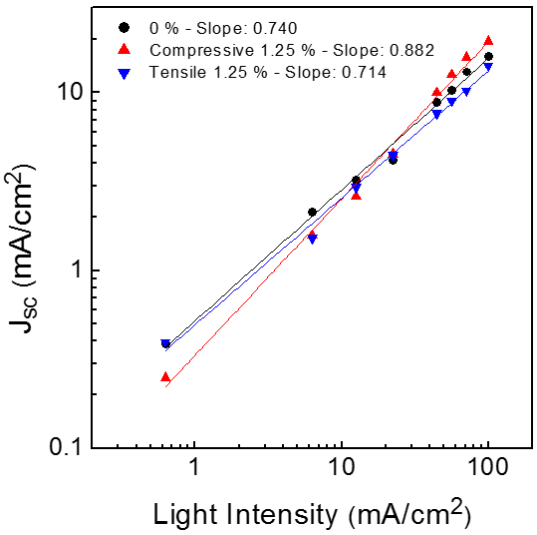

Figure 4.17: The short-circuit current, J_{sc}, as a function of the light intensity for no deformation, 1.25% compressive-, and 1.25% tensile-strain where the solid lines represent linear fits (Copyright – Appendix 1).

Lastly, the effect of the piezoelectric potential on the recombination kinetics was also investigated by performing a light-intensity-dependent solar cell measurement, and by calculating the diode ideality factor. The measured J_{sc} with respect to various light

intensities was plotted on a double logarithmic scale and then the plotted curves were fitted using a linear function. Afterwards, the exponential factor α ($J_{sc} \propto I^{\alpha}$) was extracted, which was found to be 0.740, 0.882, and 0.714 for 0% strain, 1.25% compressive strain, and 1.25% tensile strain, respectively. As an exponential factor close to unity (one) indicates effective transport of charge carriers prior to recombination, higher exponential factor values for compressive strain indicate the suppression of non-radiative recombination in the QDSC, which led to efficient charge transport and therefore enhanced J_{sc} as well as an improved PCE.[155,156] On the contrary, a decrease in the exponential factor upon the application of a tensile strain compared to no applied strain suggests that more recombination occurred at the junction due to the weaker electric field.

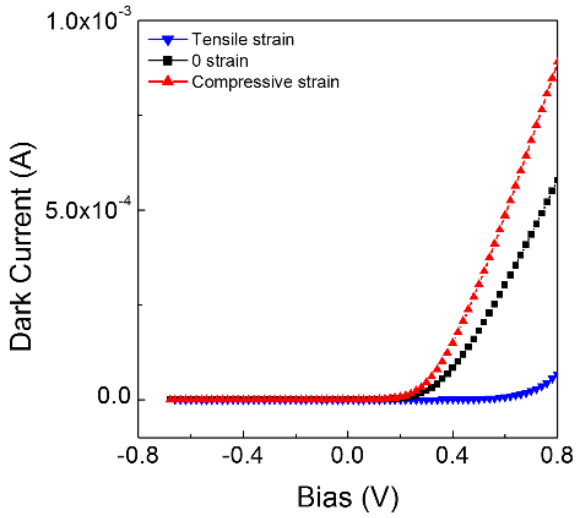

Figure 4.18: QDSC dark current as a function of the bias voltage for no strain (Black), 1.25% tensile strain (Blue), and 1.25% compressive (Red) strain (Copyright – Appendix 1).

Further verification of the recombination dynamics was performed by calculating an ideality factor using the ideal diode equation (4.8);

$$I = I_s \left[exp\left(\frac{qV}{nk_BT}\right) - 1 \right] \tag{4.8}$$

where I_s is the dark saturation current and n is the ideality factor that depends on the recombination dynamics. As the measurement was performed at room temperature we set k_BT/q to be 25.86 mV for the calculation.[145]

Figure 4.18 shows the measured dark current at each strain condition: no applied strain (black), 1.25% compressive strain (red), and 1.25% tensile strain (blue). An ideality factor was extracted by fitting the dark I-V curves using the equation (4.8). An ideality factor gives information about the dominant recombination mechanism in a solar cell; for $n = 1$ band-to-band recombination is dominant whereas for $n > 1$ other dominant recombination kinetics are present, for example trap-induced recombination ($n = 2$).[145,157] Table 4.7 summarises the obtained ideality factor for each strain condition, which is consistent with the result of the light-intensity-dependent solar cell measurements as both indicate the suppression of non-radiative recombination by the application of compressive strain to the QDSC.

Table 4.7: Ideality factor (*n*) that was calculated from a QDSC with a ZnO-porous P(VDF-TrFE) layer using the dark current shown in Figure 4.18.

Strain (%)	n
Compressive 1.25	**1.755**
0	**1.823**
Tensile 1.25	**2.927**

Complementary results for the recombination kinetics revealed an efficient transport of charge carriers and reduced charge carrier-loss upon the application of compressive strain, which is attributed to the enhanced electric potential at the junction by the

piezoelectric effect. Therefore, the non-radiative recombination was suppressed, which resulted in an improvement in the QDSC performance.

4.4 Ferroelectric effect in hybrid energy harvesting devices

In this section, the ferroelectric effect of a P(VDF-TrFE) layer on the PCE of QDSCs is addressed. It is worth noting that all QDSCs reported in this section are based on rigid ITO glass substrates in order to exclude any piezoelectric effects that might be induced by any strain/stress arising from the flexible substrate.

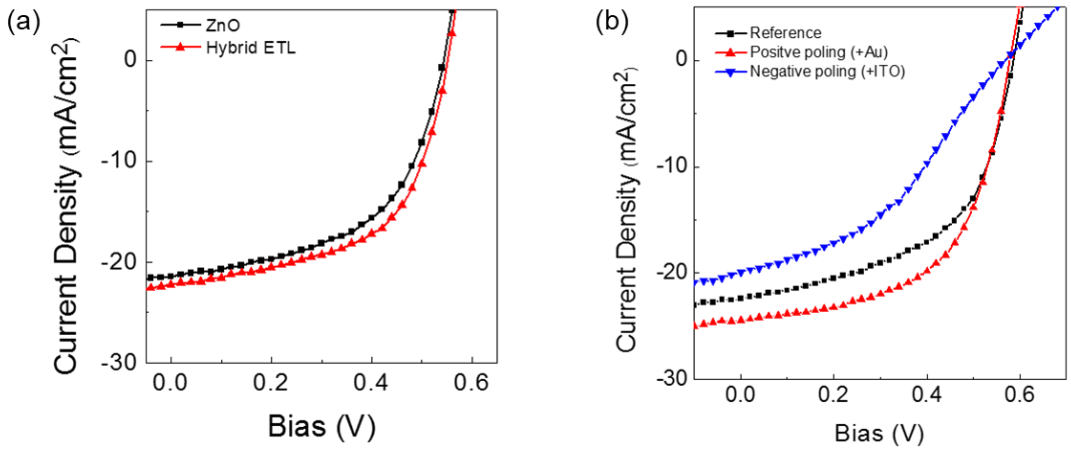

Figure 4.19: (a) Performances of a QDSC with a ZnO-only layer (black) and with a ZnO-porous P(VDF-TrFE) layer on a rigid ITO substrate. (b) Performances of a QDSC with respect to the direction of dipole polarisation by the electrical poling process; positive poling indicates that a positive bias was applied to the Au electrode side whereas negative poling indicates that a positive bias was applied to ITO electrode.

To assess and compare the ferroelectric effect on the QDSC, a QDSC with the same structure as that shown in Figure 4.1 was fabricated. Figure 4.19(a) shows the solar cell performance with a ZnO-only ETL (black) and with a ZnO-porous P(VDF-TrFE) ETL (red) on a glass ITO substrate. Similar to the piezoelectric induced QDSC (Figure 4.13),

the QDSC with a ZnO-porous P(VDF-TrFE) ETL exhibited an enhanced performance before the application of a bias, which is due to a spontaneous polarisation of the P(VDF-TrFE) film.

Afterwards, electrical poling was applied to the QDSC with a ZnO-porous P(VDF-TrFE) ETL. An external bias using a DC power supplier was applied to each electrode, ITO and Au. When a positive bias (up to +10 V) was applied to the Au electrode (0 V at ITO) this biasing condition is referred to as positive poling whereas a negative poling indicates that a bias was applied to the ITO electrode (up to +10 V) where Au was grounded. The external bias was applied for 30 minutes at 60~90 ℃ as the QDs might be damaged at high temperature. After poling, both electrodes were grounded for 30 minutes in order to remove any trapped charges during the process which might affect the measurement results. As shown in Figure 4.19(b), the application of positive poling to the device led to a significant solar cell performance enhancement whereas a negative poling led to a deterioration of the device performance, which is due to the same reasons as described in Sections 5.2 and 5.3. Table 4.8 shows the extracted solar cell parameters from Figure 4.19(b) and also average values taken from 15 devices with respect to positive and negative poling are shown in Table 4.9.

Table 4.8: Solar Cell Parameters extracted from the QDSC results (Figure 4.19 (b)).

Sample	V_{oc}(V)	J_{sc}(mAcm^{-2})	R_s(Ωcm^2)	R_{sh}(Ωcm^2)	FF	PCE (%)
Reference (Black)	0.58	22.37	7.36	226.40	0.54	**6.95**
Positive (Red)	0.58	24.46	4.36	250.54	0.57	**8.05**
Negative (Blue)	0.56	19.93	10.73	47.57	0.40	**4.52**

Table 4.9: Average values for the solar cell parameters taken from 15 devices with respect to the electrical poling direction.

Sample	V_{oc}(V)	J_{sc}(mAcm^{-2})	R_s(Ωcm^2)	R_{sh}(Ωcm^2)	FF	PCE (%)
Before	0.57 ± 0.01	22.94 ± 1.21	10.04 ± 0.62	205.92 ± 39.22	0.50 ± 0.02	**6.54 ± 0.33**
Positive	0.58 ± 0.02	24.14 ± 1.04	5.64 ± 1.67	221.92 ± 43.72	0.53 ± 0.03	**7.39 ± 0.44**
Negative	0.56 ± 0.01	20.61 ± 1.32	11.44 ± 1.32	88.35 ± 50.80	0.44 ± 0.05	**5.50 ± 0.67**

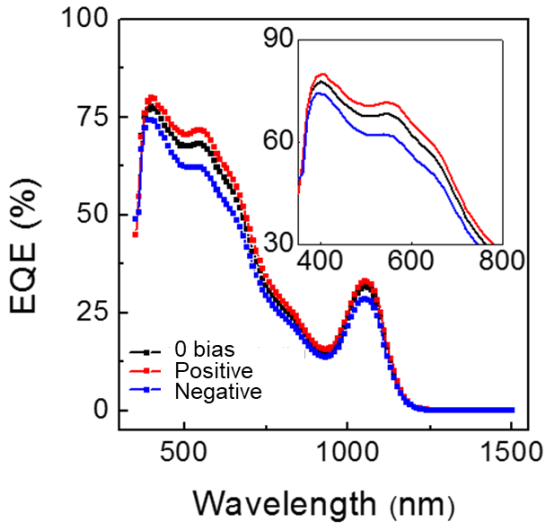

Figure 4.20: The EQE as a function of wavelength for different electrical poling conditions.

The enhancement in the photocurrent was also confirmed by measuring the external quantum efficiency (EQE) as shown in Figure 4.20. Over the spectral range from 350 to 1500 nm, an enhanced EQE was observed when a positive poling was applied to the device. By integrating over the spectrum, it was revealed that J_{sc} was approximately 18.56, 20.01, and 17.42 mA cm^{-2}, for reference, positive poling, and negative poling, respectively. A slight decrease in the J_{sc} level compared to a J-V sweep measurement was due to a change of photo-active materials under light illumination and a measurement error.[58,91] The EQE measurement further confirms that the enhancement in both the J_{sc}

and the PCE is attributed to efficient charge transport resulting from an enhanced electric field at the junction.

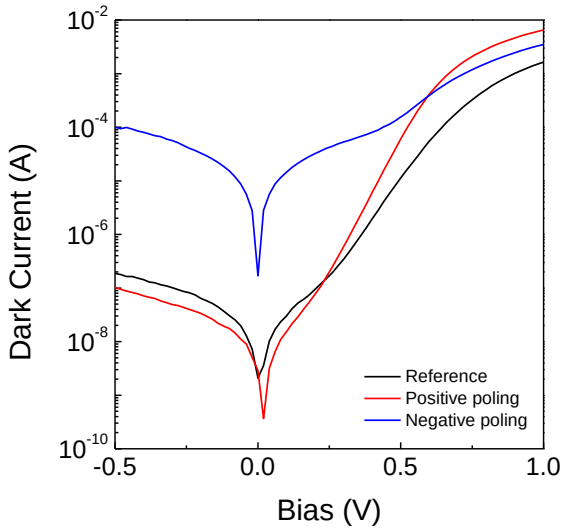

Figure 4.21: QDSC dark current for no poling (Black), positive poling (Red), and negative poling (Blue).

Finally, the recombination dynamics were also investigated on the ferroelectric-induced QDSC. Figure 4.21 shows the measured dark current for the different poling conditions, which revealed that the noticeable dark saturation current changes. By using the diode equation, an ideality factor for each QDSC was calculated as shown in Table 4.10, which was consistent with the results for the piezoelectric-induced QDSC.

Table 4.10: Ideality factor (*n*) that was calculated from a QDSC with a ZnO-porous P(VDF-TrFE) layer using the dark current shown in Figure 4.21.

Sample	n
Positive poling	**1.81**
reference	**1.92**
Negative poling	**4.09**

4.5 Conclusions

In this Chapter, it is demonstrated that the introduction of a P(VDF-TrFE) layer can induce an additional piezoelectric potential when mechanical strain/stress was applied to a quantum dot solar cell (QDSC). A porous structure in the P(VDF-TrFE) polymer was formed in order to ensure the transport of photo-generated charges since this polymer typically behaves as an insulator, which cannot ordinarily transfer charges when the thickness is greater than the tunnelling limit (~ a few nm). A predominantly β-phase porous P(VDF-TrFE) layer exhibited piezoelectric properties upon the application of mechanical vibration. In contrast, a ZnO-only electron transport layer (ETL) did not exhibit a piezoelectric potential due to the random orientation of the ZnO that forms by spin-coating a solution of ZnO nanoparticles, which confirmed that the piezoelectric potential generated by mechanical stress only occurred with the porous P(VDF-TrFE) layer. PbS QDSCs with a ZnO-porous P(VDF-TrFE) ETL demonstrated a modulation in the hetero-junction properties by the induced piezoelectric potential. As a result, both the J_{sc} and PCE were modulated with respect to the applied strain: a decrease in a solar cell performance was observed when a tensile strain was applied whereas the device performance was enhanced when a compressive strain was applied, which was found to be as large as 38% for the J_{sc} (from 14.18 to 19.53 $mAcm^{-2}$) and 37% for the PCE (from 3.68% to 5.05%), respectively. The enhanced solar cell performance was attributed to an enhanced exciton dissociation and charge transport as well as a suppressed non-radiative recombination.

A similar phenomenon was observed when the same structure was used but a ferroelectric effect was exploited instead of the piezoelectric effect. The demonstration of the same result is considered to be due to the fact that the dipole polarisation generates an

additional electric field, either through ferroelectric or piezoelectric coupling, which indicates that an additional electric field/potential is effective in enhancing the performance of a QDSC

Chapter 5. Hybrid Energy Harvesting Systems: Integration of Photovoltaics with a Mechanical Energy Harvester

5.1 Introduction

In Chapters 2 and 3, energy harvesting mechanisms involving photovoltaic, piezoelectric, and ferroelectric effects as well as materials that can be potentially used for energy harvesting have been considered. Also, excellent energy harvesting performance has been demonstrated with an individual device and potential application in a solar panel (Chapter 2) and in the generation of optical signals using light emitting diodes (Chapter 3) as a proof-of-concept have been suggested. However, for energy harvesting devices, it is the sustainability and reliability that are frequently questioned as environmental energy sources are intermittent, by their nature. Moreover, different types of energy harvesting devices typically exhibit high contrast in their output characteristics; for instance, a high current but low voltage for a solar cell whereas low current but high voltage for a mechanical energy harvester (MEH).[32,158,159] This high contrast suggests that an integrated system, which can synergistically generate a high current from one device while increasing the upper potential limit from the other device, is highly desirable and potentially realisable. In addition, an integrated energy conversion system would be able to harvest different kinds of environmental energy, simultaneously, which potentially reduces the risk of power interruption due to intermittence.[159,160]

In this regard, it is highly desirable that integrated energy harvesting devices are developed to overcome the aforementioned limits so as to eventually realise sustainable energy and electronic devices by harnessing environmental energy sources. Therefore, enormous progress has been made so far to accomplish a sustainable and reliable

integrated energy harvesting system. Up to now, the integration of different types of energy harvesting devices has been performed on a large scale for generating a large amount of energy. For the realisation of the sustainable and independent electronic devices, however, it is also necessary to develop a versatile compact energy harvester with high-power density that can extract various types of environmental energy sources using cost-effective methods.

In this chapter, an integrated energy harvester (IEH) is explored by employing entirely solution-based techniques at room temperature and in ambient air. An IEH is able to harvest various environmental energy sources, such as sunlight and mechanical vibrations, both individually and simultaneously. The IEH consists of solar cells connected in series to supply the current and an MEH to increase the potential limit of the IEH. For the solar cell, PbS QDs were used as they have a high absorption coefficient, bandgap tunability, and are solution processable. Also, the P(VDF-TrFE-CTFE) terpolymer was employed for the MEH because the polymer exhibits a high mechanical stability, excellent performance, and high transparency that ensures light penetration to the PbS QD layer. By integrating the QDSC and the MEH into a single device, the IEH is found to exhibit a significantly enhanced output power when compared to the separate components. In addition, the IEH was able to harvest various environmental energy sources simultaneously, which makes it more reliable and consistent. For a future application of the IEH as a sustainable power supplier, the operation of an infrared motion sensor which was independent of any other power source was demonstrated.

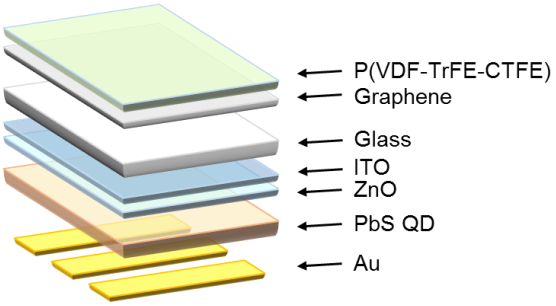

Figure 5.1: A schematic of an integrated energy harvester that consists of a QDSC and a mechanical energy harvester.

Figure 5.1 shows an illustration of an IEH which was composed of QDSCs connected in series and an MEH. An inverted structure of QDSCs was used with TBAI and EDT ligands as explained in Chapter 2. Thickness of each layer was 200 nm of an ITO electrode, 80 ~ 100 nm of a ZnO ETL, 270 nm of TBAI-treated QD layers, 50 nm of EDT-treated QD layers, and 100 nm Au electrode, respectively. On the other side of the ITO substrate, an MEH which consists of a single layer graphene as an electrode and a β-phase P(VDF-TrFE-CTFE) film as an active material was transferred. Thickness of a P(VDF-TrFE-CTFE) film was approximately 2 μm.

5.2 Photovoltaic Cells for integrated energy conversion system

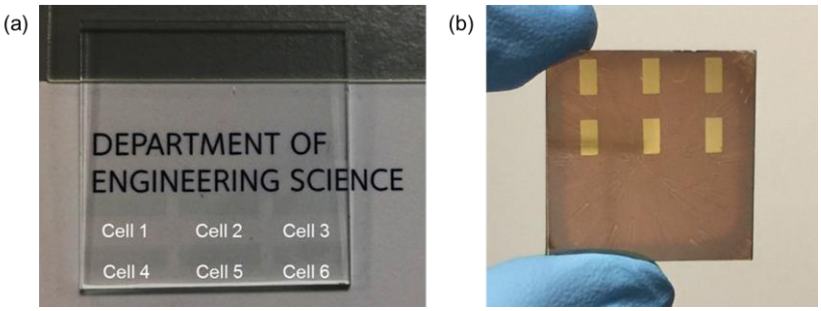

Figure 5.2: (a) A photograph of a patterned ITO substrate for the QDSCs. (b) An image of 6 QDSCs fabricated onto the ITO substrate with a total size of 2.5 × 2.5 cm^2.

An IEH consisted of a series of 6 QDSCs and an MEH. As shown in Figure 5.2(a) and (b), 6 QDSCs were fabricated using the same method as explained in Chapter 2 except that a patterned ITO substrate with areas of 2.5 × 2.5 cm^2 was employed for a QDSC. A fabricated QDSCs in an IEH showed a uniformly coated QD film and therefore 6 QDSCs showed a similar solar cell performance with high PCE as summarised in Table 5.1. It is worth noting that a batch of QDs with a 1.24 eV bandgap was used for experiments in this chapter (see Chapter 2 for more details about QD analysis).

Table 5.1: A performance of each QDSC that was fabricated on the same substrate by patterning an ITO electrode.

Samples	V_{oc} (V)	J_{sc} (mA/cm^2)	FF	PCE (%)
1	0.52	26.44	0.59	8.11
2	0.50	26.75	0.68	9.11
3	0.52	26.75	0.62	8.65
4	0.50	25.92	0.58	7.50
5	0.52	27.44	0.57	8.13
6	0.50	27.02	0.61	8.24
Average	0.51	26.72	0.61	8.29

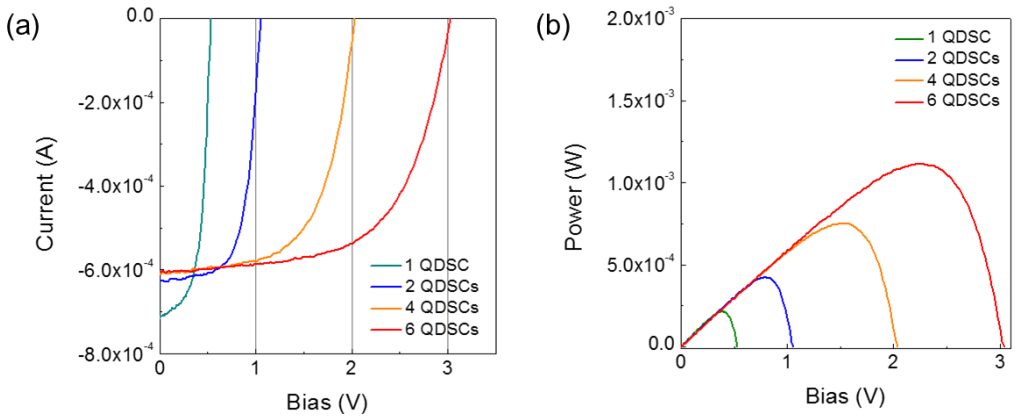

Figure 5.3: (a) Current-voltage curves for the QDSCs consisting of one solar cell to 6 solar cells connected in series. (b) Calculated output power from QDSCs (a) with respect to the number of cells connected in series.

Although all the single QDSCs exhibit high I_{sc} (or J_{sc}) and high PCE, the low V_{oc} of a solar cell is generally a limiting factor for practical device applications, such as sensors which require at least 3 to 5 V to operate. Considering the V_{oc} of a single QDSC, which typically ranges from 0.35 V to 0.8 V at maximum, enhancing V_{oc} either by fabricating a tandem solar cell or solar cells that are connected in series is of particular importance. However, for a tandem solar cell to attain higher V_{oc}, the J_{sc} is compromised and therefore this is not a desirable approach. Instead, 6 QDSCs were connected in series to enhance the output V_{oc}. Figure 5.3(a) shows the performance (J-V curves) of a single QDSC and QDSCs that were connected in series ranging from 2 to 6 solar cells. For the QDSCs arranged in series there was found to be an increase in the V_{oc} up to 3 V but a decrease in the I_{sc} at the same time as the series resistance increased linearly ($R_s \times N$ (a number of cells), as shown in equivalent circuit in Figure 2.30). However, the drop in the I_{sc} was negligible when compared with the enhancement in V_{oc} and therefore a significant enhancement in output power was observed in the QDSCs when connected in series, reaching approximately 1.2 mW as shown in Figure 5.3(b).

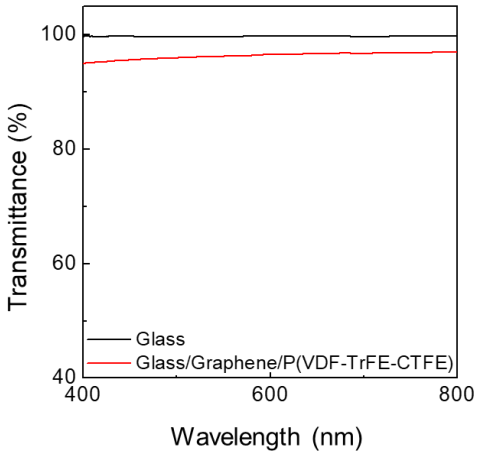

Figure 5.4: Transmittance of for a MEH layer assembled on the other side of the IEH. Compared to only a glass substrate, the MEH layer exhibited a high transmittance with the slight decrease being attributed to the single layer of graphene that was employed as the bottom electrode.

Afterwards, the assembly of a MEH was carried out so as to fabricate the IEH. More details about the fabrication methods are described later (see Section 5.3). For the QDSCs and the MEH to operate in harmony, it was important that neither one of the devices should be compromised so as to ensure the enhancement of the output performance when compared with that of a single device. One of the most important conditions for a solar cell to maintain its output performance is the sufficient absorption of light within the photo-active layer (the PbS QD layer in our case). As shown in Figure 5.4, an additional P(VDF-TrFE-CTFE) layer deposited onto a graphene electrode showed high transmittance comparable with that of a glass substrate, which is attributed to the highly transparent single graphene electrode and the formation of a highly transparent P(VDF-TrFE-CTFE) film (see Section 5.3 for more details).[161,162]

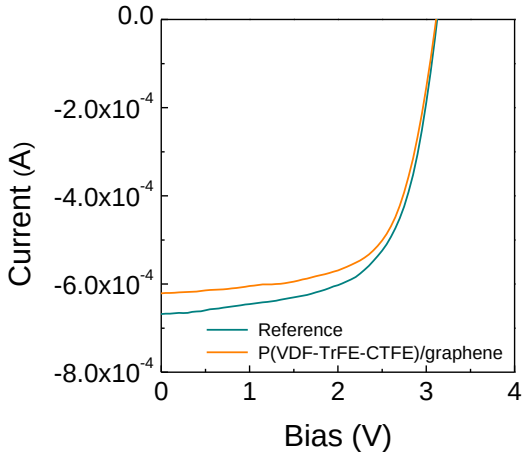

Figure 5.5: The performance of 6 QDSCs connected in series before (denoted as reference in light blue colour) and after the deposition of a MEH layer (denoted as P(VDF-TrFE-CTFE)/graphene in yellow colour) on the other side of the ITO substrate so as to fabricate the IEH.

After the deposition of the P(VDF-TrFE-CTFE) layer for the purposes of mechanical energy harvesting, we measured the performance of the QDSCs. As shown in Figure 5.5,

a slight decrease in I_{sc} (6.68×10^{-4} A to 6.19×10^{-4} A) was observed in the QDSCs that were connected in series whereas there was no noticeable change in V_{oc}, which indicates that it is due to a slight decrease in the transmittance, not other physical or chemical damages induced during the deposition process. It is worth noting that the decrease in the PCE was small (Δ0.3%) and also the IEH provides more significant benefits, such as harvesting various environmental energy sources, supplying energy continuously, and potentially enhancing the overall device performance.

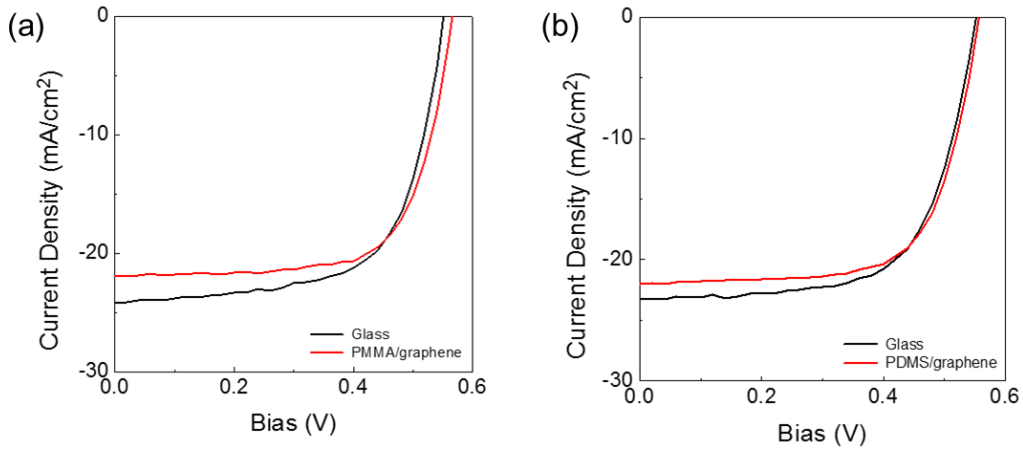

Figure 5.6: Compatibility test of an IEH using different polymer layers for a MEH, such as PMMA (a) and PDMS (b) which are also widely and commonly used for mechanical energy harvesters.

In order to address whether the proposed approach for the IEH system can be generalised the compatibility of other frequently used materials for mechanical energy harvesting, such as polymethylmethacrylate (PMMA) and polydimethylsiloxane (PDMS), was also investigated. As shown in Figure 5.6(a) and (b), it is found that the deposition of PMMA and PDMS showed a comparable result to that obtained using the P(VDF-TrFE-CTFE) layer, which suggests that the fabrication of integrated energy harvesters using other materials is entirely feasible. It is worth noting that for a compatibility test a

single QDSC with an active area of 0.03 cm^2 was used whereas the other experimental conditions remained the same.

5.3 Mechanical energy harvesting devices for an integrated energy conversion system

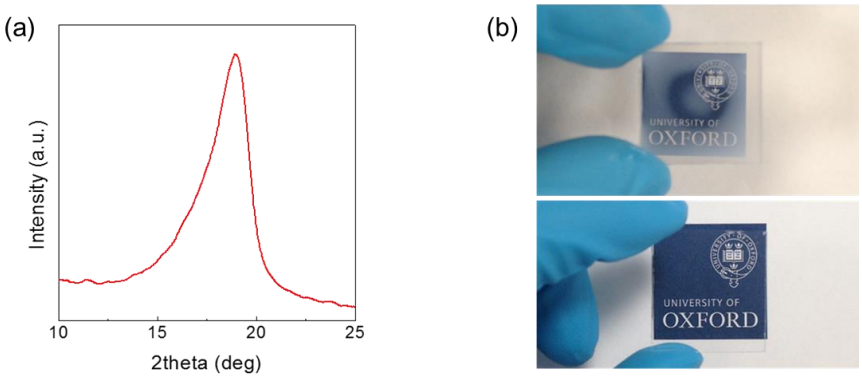

Figure 5.7: (a) XRD measurement of an SA-treated P(VDF-TrFE-CTFE) film, which showed the formation of the ferroelectric β-phase. (b) The results of SA treatment on the transmittance of ambient light through a P(VDF-TrFE-CTFE) film. The greyish opaque polymer film became highly transparent with the application of the SA treatment. The XRD was measured in the Materials Department at the University of Oxford.

For the mechanical energy harvester in the IEH, the terpolymer P(VDF-TrFE-CTFE) was employed as it has a large electromechanical response, elastic energy density, and mechanical stability. A P(VDF-TrFE-CTFE) solution of 10 wt% concentration was spin-coated onto a graphene electrode and then solvent annealing (SA) was performed in order to form a β-phase film (for more details, see Chapter 3). An SA-treated P(VDF-TrFE-CTFE) film exhibited a formation of the β-phase as identified from the XRD measurement which shows a peak at approximately 19.4˚ (Figure 5.7(a) and detailed explanation is described in Chapter 3).[136,137,163] Another important point to mention is

that the SA treatment has a significant effect on the colour tuning of the film. Figure 5.7(b) shows images of a spin-coated P(VDF-TrFE-CTFE) film (top) and the polymer film after SA treatment (bottom). The ordinarily greyish opaque polymer film became highly transparent using SA treatment, which is probably due to the reduced light scattering from the smooth and flat surface (for more details, see Chapter 3).[164] This high transparency is an essential requirement for IEH application so as to ensure light penetration through to the light absorption layer, which otherwise deteriorates the performance of a solar cell and thus overshadows the benefits of the integrated energy conversion system.

The assembly of a mechanical energy harvester into the IEH was then carried out. First, Cu foil under graphene was etched and then washed three times using deionised (DI) water.[165] Afterwards, graphene with a β-phase P(VDF-TrFE-CTFE) film on it was transferred to the other side of the IEH using a dry transfer method to avoid any possible damage by solution (by a wet transfer method) to the QDSCs. Lastly, the assembled IEH was dried at room temperature for several hours before use.

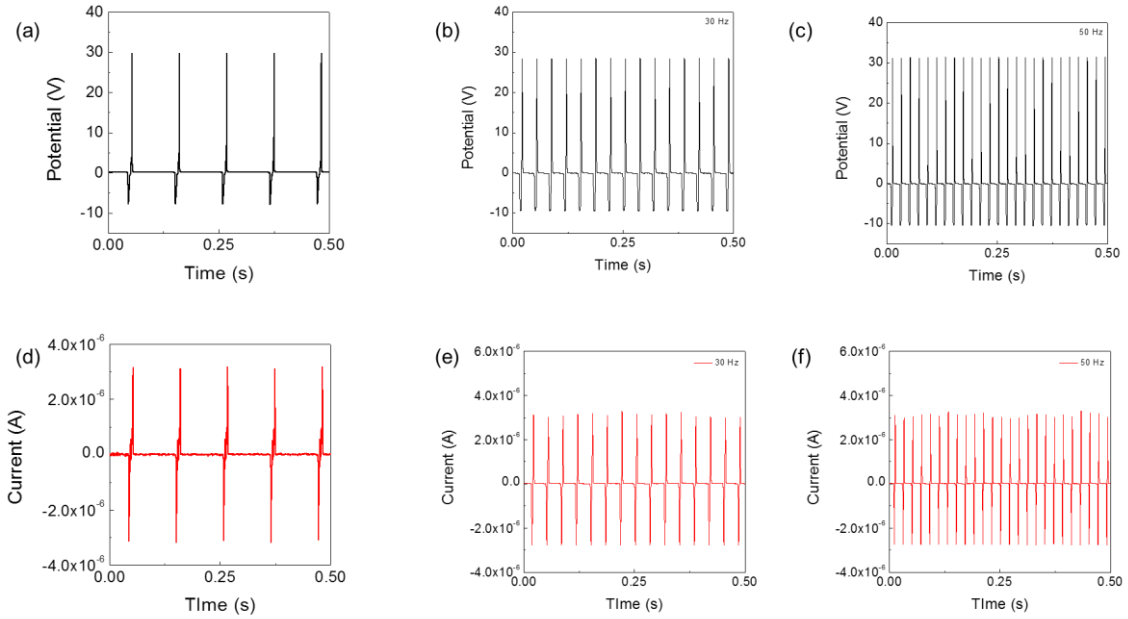

Figure 5.8: Output potential and output current of the MEH when driven by a linear motor at a frequency of (a) and (d) 10 Hz, (b) and (e) 30 Hz, and (c) and (f) 50 Hz, respectively.

Investigation of the individual mechanical energy harvesting performance was conducted by using environmentally abundant energy sources, such as mechanical vibrations, sound waves and wind. Figure 5.8 shows the output performance of the MEH driven by mechanical vibrations at three different frequencies; 10, 30, and 50 Hz. The generated peak-to-peak potential was approximately 40 V whereas the generated peak-to-peak current was around 6×10^{-6} A, which shows a stable device performance regardless of the input frequency. It is worth noting that a generated potential by the MEH was adjusted to a relevant level by controlling the travel distance of the linear motor shaft (0.13 cm per stroke) so as to reduce damage to a power management circuit and a QDSC in an integrated system (Section 5.4) by a high potential of the MEH. As the performance of a mechanical energy harvester using the ferroelectric effect is dependent upon the relative electrostatic forces between the active material and the electrode there is typically an optimum point where the output performance is maximised.

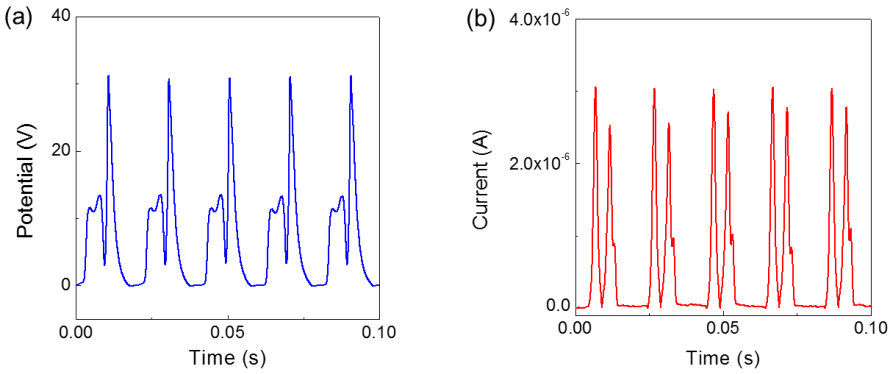

Figure 5.9: Output characteristics (a) potential and (b) current of the MEH using a rectifying circuit where the MEH was driven at 50 Hz by a linear motor.

For the integration of two different systems (alternative current (AC) for a mechanical energy harvester and direct current (DC) for a solar cell), the AC signal from the mechanical energy harvester was rectified using a rectifying circuit (Section 5.4, Figure 5.12). Figure 5.9 shows the output potential and current at a frequency of 50 Hz after rectification. It is worth noting that the use of a high frequency is desirable for generating not only a high output power within the same time frame as that of low frequency one, but also a more DC-like potential output as the time gap between pulses at fixed duty cycle significantly decreases. The instantaneous power that was calculated from the rectified potential and current of the MEH was approximately 0.48 mW.

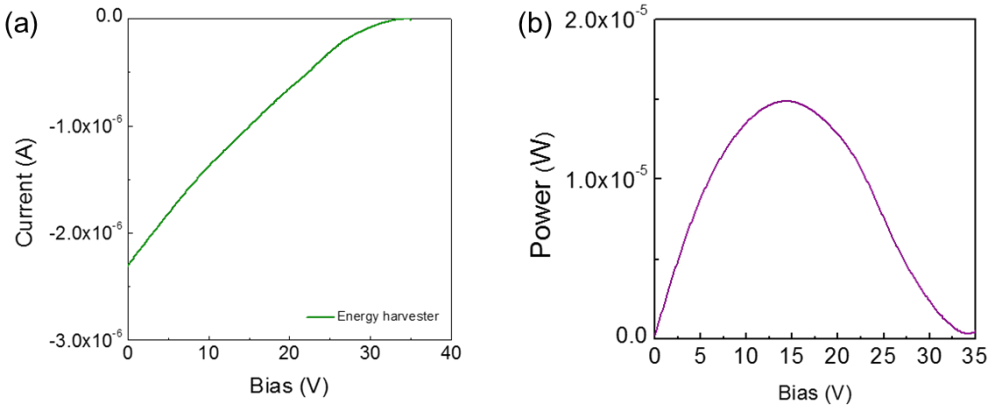

Figure 5.10: (a) I-V sweep measurements of the MEH at 50 Hz using a Keithley 4200-SCS. (b) Calculated output power of the MEH at 50 Hz where a maximum power of 15 μW can be delivered by the MEH.

As the instantaneous power is the value that is obtained at each potential (V_{oc}) and current (I_{sc}) maximum, it does not take into account the real output power of a device at various impedance values in the same way as the solar cell case. Therefore, I-V measurements were performed using a Keithley 4200-SCS to provide a more realistic estimation of the output power of the MEH. Figure 5.10 shows the result of an I-V sweeping measurement at an input frequency of 50 Hz. Following this, the output power of a device was calculated by multiplying the current and potential (P = IV) and it was revealed that a maximum power can be obtained at a potential of 13.5 V (V_{mp}, i.e. maximum power voltage) for which I_{mp} was 1.11 μA. As a result, the maximum power was approximately 15 μW and the internal device resistance was 12 MΩ, which indicates that the polymer film is highly insulating.

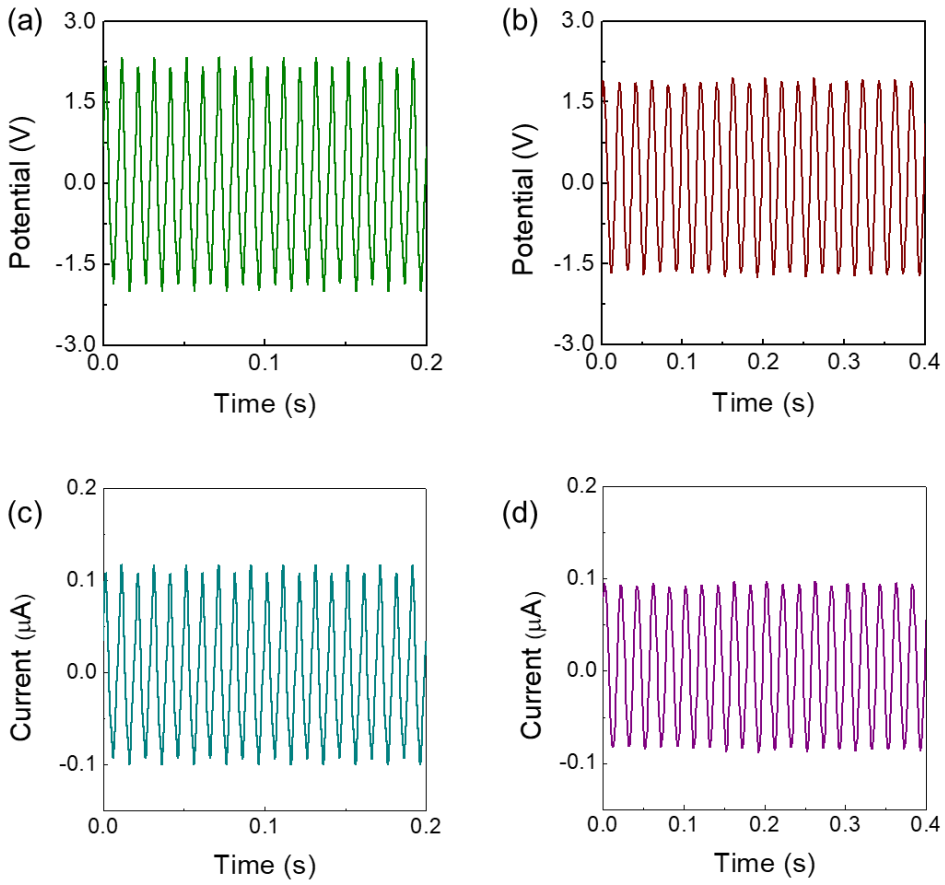

Figure 5.11: Output potential and current of the MEH by harvesting environmentally-abundant energy sources. (a and c) are generated potential and current by harvesting sound waves and (b and d) are potential and current output by harvesting wind.

In addition, other types of environmentally-abundant energy, such as sound and wind, were harvested by the MEH. Sound waves were produced using a function generator and the output decibel was 90 dB. Also, a fan to generate wind waves was used. As shown in Figure 5.11, a generation of output potential and current was observed by harvesting energy from sound and wind waves, which were approximately 3.5 V and 0.2 μA, and 3.2 V and 0.18 μA, respectively. The MEH using a β-phase P(VDF-TrFE-CTFE) and graphene electrodes showed versatile behaviour in harvesting various environmental energy sources and excellent energy harvesting performance for even minute mechanical vibrations typically surround us in our daily life.

5.4 An integrated energy conversion system

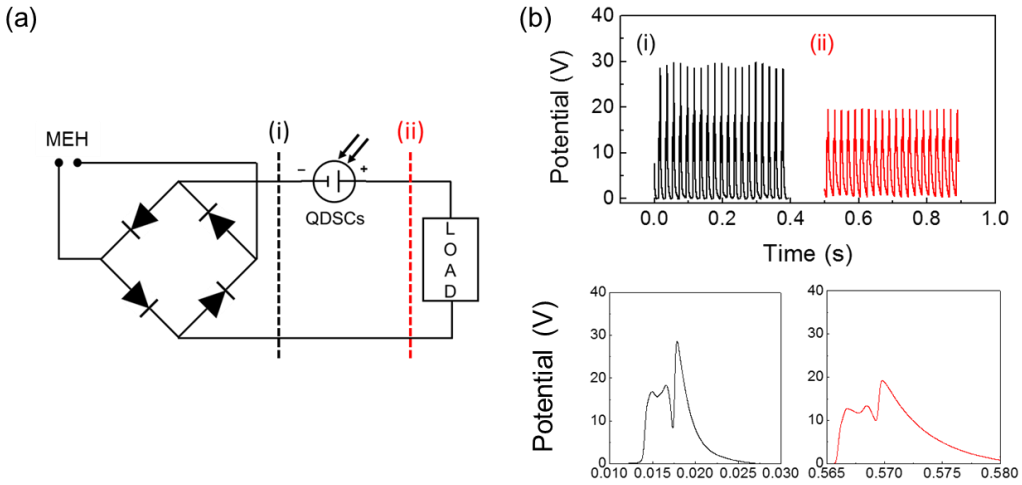

Figure 5.12: (a) A circuit for integration that consists of a MEH, a rectifier, and QDSC. (b) Output potential characteristics of a MEH with and without the presence of QDSCs in the integration circuit.

Finally, the performance of the IEH and its possible applications are demonstrated. The MEH and the QDSCs in the IEH were connected in series in order to enhance the upper potential limit according to Kirchhoff's voltage law, which states that the total voltage in a closed loop is identical to the sum of the voltage differences around the loop.[166] Moreover, a parallel connection might cause a backflow of current to the other generator as the current generated by the MEH was lower than that of the QDSCs. However, a decrease in the output potential was observed due to an increase in the series resistance from the perspective of the MEH as shown in Figure 5.12(b). Nevertheless, the output potential (~ 20 V) was far higher than that of the QDSC and still large enough for driving most modern electronic devices such as 4.2 V for a mobile and 14.8 V for a laptop.

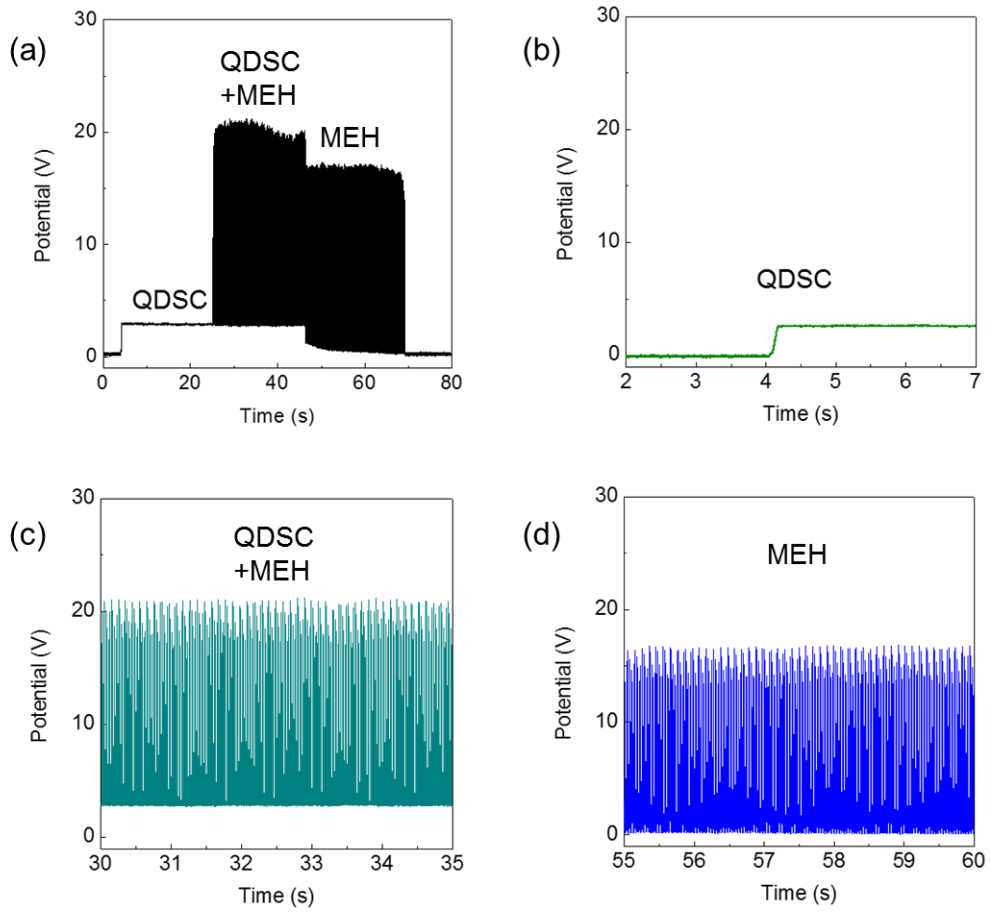

Figure 5.13: (a) Output characteristics of the IEH that exhibited the individual characteristic outputs when it was driven by (b) a solar simulator only, (c) both a solar simulator and a linear motor, simultaneously, and (d) a linear motor only.

Harvesting various energy sources, photons and mechanical vibrations, individually and simultaneously was carried out using the IEH. First, light (photons) from a solar simulator was shone on the QDSCs in the IEH. As expected, the QDSCs generated a potential of ~3 V as shown in Figure 5.13(a) and (b). After 20 seconds, the mechanical energy source was turned on using a linear motor at a frequency of 50 Hz. As shown in Figure 5.13(a) and (c), the rectified output potential generated by the MEH was added onto the potential generated by the QDSC, reaching ~21 V, which demonstrates the simultaneous energy harvesting of two different energy sources. Then, the light source

was turned off and consequently the potential drop (3 V), which corresponds to the contribution from QDSCs, was observed as shown in Figure 5.13(a) and (d). Finally, when all the energy sources were turned off, the output potential of the IEH reduced to zero.

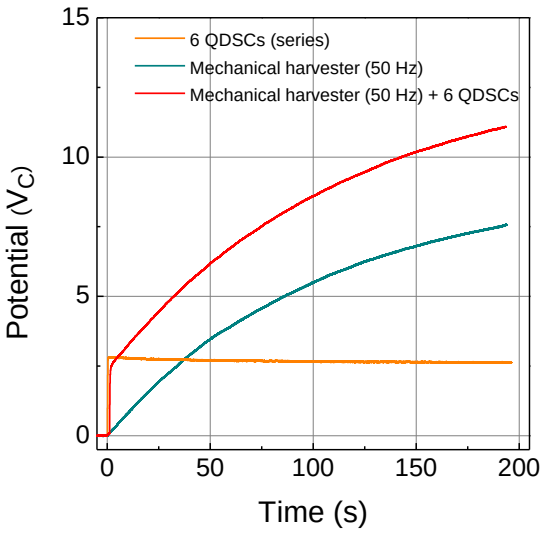

Figure 5.14: The potential in a capacitor (200 µF, 16 V) that was charged by harvesting environmental energy sources using only the QDSC (yellow curve), the MEH only (light green curve), and both the QDSC and the MEH, i.e. the IEH (red curve).

For a better use of harvested energy, a power management circuit which consists of an energy harvester and a storage system is required. Towards this end, a commercially available capacitor (200 µF, 16 V) was connected to the circuit (Figure 5.12) to store the generated energy. The capacitor was then charged using light, light and mechanical vibrations, and mechanical vibrations only. As shown in Figure 5.14, the QDSC again showed an immediate charging of the capacitor to 3 V but afterwards there was no more potential enhancement, which indicates that a potential limit of the QDSC was 3 V (V_{oc}). In contrast, the mechanical energy harvester charged the capacitor slowly but constantly up to 7.5 V, which suggests that the upper potential limit of the MEH is higher than that

of QDSC but the generated current is lower than that of QDSC. Lastly, when photons and mechanical vibrations were harvested simultaneously, we could observe a synergetic effect of the IEH. As illustrated by the red colour in Figure 5.14, the potential curve showed a rapid potential rise which is attributed to the high current from QDSCs. This rapid potential charging was followed by a constant increase in potential above 10 V, which is attributed to the high potential of the MEH. In addition, the slope of the IEH was 92 $mVsec^{-1}$ whereas that of the MEH was 84 $mVsec^{-1}$, which again demonstrated high capacitor charging rates by harvesting two different energy sources. The above results highlight the beneficial coupling of the integrated system; initial rapid potential rise and constant potential increase to more than 10 V with an increased charging rate, which cannot be attained by using only the QDSC or the MEH.

5.5 Demonstration & Applications

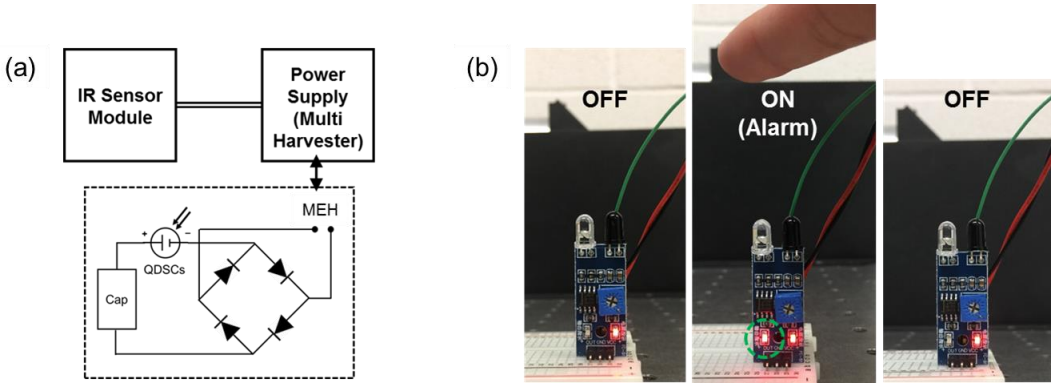

Figure 5.15: (a) A schematic of an integrated circuit for powering a sensor module using the IEH. (b) Images of the IR motion sensor in operation as a proof-of-concept where the IEH can be applied in a practical application.

The IEH exhibited an excellent ability to harvest energy by harnessing photon and mechanical vibrations that are abundant around us in our daily life. For a proof-of-concept, an application to the realisation of building sustainable sensors (and sensor networks) was

demonstrated. A commercially-available IR motion sensor was obtained that generated an alarm when human motion was detected. The IR motion sensor was connected with a power management circuit (Figure 5.12 (a)) as illustrated in Figure 5.15 (a). To operate the IR motion sensor, a total capacitance of 40 mF (16 V) was used as operating sensors requires not only a high voltage (3.5 ~ 5 V) but also a high current. 40 mF capacitors were charged for one hour. Figure 5.15(b) shows the operation of the IR motion sensor that was connected to the IEH and its power management circuit, i.e. independent from any other power supply. When an object passed the IR-sensor the detected IR light reflected from the object and rang the alarm. The above result highlights the demonstration of building sustainable sensors using the IEH for future applications.

It is worth noting that the IEH proposed in this chapter can be more efficient in supplying power by employing sensors consuming nano- to microscale power. For example, the IEH is able to generate power of 60.5 μW using 200 μF capacitors in an integrated circuit, which is enough to operate low power sensors. Another possible way to use the IEH is that, by scaling up the device dimensions, the device can be embedded into motorways to monitor the volume of traffic where both solar energy and mechanical pressure are present. However, in this case, a piezoelectric effect rather than a triboelectric effect will be more suitable to harvest mechanical energy, which in turn results in reduced potential and current from the mechanical energy harvester.

5.6 Conclusions

An integrated energy harvester (IEH), which consisted of a quantum dot solar cell (QDSC) and a mechanical energy harvester (MEH), was fabricated by an all-solution processing technique without any thermal annealing process. The individual components showed excellent energy conversion performance by harvesting various environmental

energy sources, such as sunlight, mechanical vibrations, sound waves, and wind. In addition, the combined coupling of these harvesters was observed when various energy sources were harvested by the IEH simultaneously; a potential that was greater than the limit of V_{oc} of a solar cell was obtained, which was attributed to the high potential output of the MEH, and also the charging rate of the storage system was enhanced due to the high current contribution from the QDSC. As an independent and self-sustainable power source, the IEH demonstrated the operation of an IR-sensor for building a sensor network system.

6. Conclusions and Future Work

6.1 Summary of Key Results

In this thesis, current energy harvesting technology harnessing photons and mechanical vibrations was investigated. Via novel approaches, significant enhancement in the QDSC and MEH performance was achieved.

First, as revealed by the Shockley–Queisser limit for a single junction solar cell, i.e. using only one type of bandgap material, it has a certain maximum PCE that can be attained depending on its bandgap. One of the strategies for achieving higher PCEs greater than the Shockley–Queisser limit is to employ various bandgaps to form a multiple junction. This enables the absorption of a wider range of the solar spectrum and thus the J_{sc} of a solar cell can be greatly improved. In the field of QDSCs, this strategy was limited due to the time-dependent QD synthesis method, which led to less homogeneous size distribution of synthesised QDs. Through the development of a reagent limiting synthesis method, it was possible to achieve QDs with a narrow size distribution, which ensures uniform optical properties and efficient charge carrier transport. Attributed to a uniform distribution of QD size, a high efficiency multi-junction QDSC was fabricated, which showed a significant enhancement in the PCE (Δ7.97%, from 8.0 to 8.7%).

Second, a room temperature annealing method, which is called solvent annealing (SA), provided several benefits in the fabrication of a MEH with enhanced performance. In terms of an engineering issue, the SA method makes it possible to have a wider selection of polymer substrates that cannot sustain the relatively high temperature post-annealing process. This provides a huge benefit in terms of the fabrication of highly

flexible MEH or textile-based MEH for future electronic applications. In addition, the formation of a smooth and flat surface by the application of the SA induced higher surface potential than that of a rough surface PVDF-based polymer film that was formed by a thermal annealing (TA) method. This is because the electric dipoles formed normal to the surface and thus the vector sum of electric dipoles on a smooth and flat surface was higher. Remarkable device performance was achieved by employing a terpolymer P(VDF-TrFE-CTFE) which was attributed to the high electromechanical response and elastic energy density and the formation of the β-phase terpolymer film.

Based upon the studies conducted on the characteristics and performances of an individual energy harvesting device, advanced energy harvesting devices were fabricated.

First, a high efficiency QDSC using the ferroelectric and piezoelectric effect of PVDF-based polymer was demonstrated. An employment of a piezoelectric and ferroelectric effect induced an additional electric field at the hetero-junction between a ZnO ETL and a light absorbing layer QDSC where charge trapping and recombination occur much faster than at other locations. As a result, the photo-generated charges were transported prior to recombination, resulting in an enhanced current density (J_{sc}) and consequently a higher power conversion efficiency (PCE) in the QDSC.

In the next stage of the thesis, the integration of a QDSC with a mechanical energy harvester, which was called an integrated energy harvester (IEH), was demonstrated so as to realise an all-in-one energy harvesting device. The IEH exhibited a noticeable enhancement in device performance by delivering power beyond that achievable with the individual components, which greatly enhances the overall device performance. Also, as the IEH is able to harvest various environmental energy sources simultaneously, the

hybridisation approach reduces any risk of sudden power interruption and, in turn, greatly improves device reliability. With the IEH, the demonstration of a self-powered electric device, such as an IR sensor operation, was performed, which suggests a promising future for the sustainable energy system using energy harvesting technology.

Finally, an investigation of a larger scale application of the energy harvesting technology was carried out based on the current 'cell' scale technology. By using simulated studies, it was revealed that an improvement in the cell scale is directly applicable to the larger scale energy harvesting device, which suggests that researches on a cell scale energy harvesting will contribute to the development of better performance and efficiency larger scale energy harvesting devices.

6.2 Future Work

A recent demonstration of an ink-type QDs solution exhibited a PCE of more than 11%, which has been a great breakthrough in QDSC as the PCE had previously saturated at less than 10% for several years.[62] The enhancement is attributed to a solution-phase ligand exchange process which enables the formation of closely packed QD films with flat energy landscapes. Also, the reduced QD aggregation and energy funnelling enhance the transport of charge carriers, and facilitate efficient charge carrier injection into the electrodes. Motivated by this work, currently research on QDSC is shifting from a solid-state ligand exchange method to a solution-phase ligand exchange method.[84,167]

Also, due to the similarities between PbS QDs and Pb-based perovskites in terms of their compositions, it has been revealed that QD in perovskite solids can greatly enhance carrier transport of QDs due to a significantly enhanced diffusion length. Together with

a solution-phase ligand exchange method, the employment of perovskite-QD hybrid solar cell material could be promising for further improvement in the PCE.[168]

A multiple exciton generation, which is one of the merits of QDs as I revealed in Chapter 2, can be also used to improve the photoelectrochemical hydrogen evolution reactions.[169] This work suggests a potential use of QDs for not only QDSC technology but also for other types of energy device applications.

In terms of mechanical energy harvesting (MEH), I was not able to research the effect of electrical poling on the resulting performances of MEH in great detail. An electrical poling process is able to align the electric dipoles of a PVDF-based polymer film and therefore higher surface potential will be induced on the surface of the film, which can result in a further boost in the device performance.

In addition, research into MEH is becoming more and more oriented towards the integration of an MEH with other types of energy harvesting devices[41] and also with storage systems[170] for the development of a more reliable and stable sustainable power source. The realisation of self-powered electronics technologies enables MEH to be used in biomedical systems, such as health monitoring, pacemakers, and implantable cardioverter defibrillators.[171]

Although the current energy generation system is highly dependent on fossil fuels there is reason to be optimistic that progress in photon and mechanical energy harvesting will resolve and mitigate the energy crisis and future risks, such as global warming and climate change, in the future, not to mention advances in other energy devices, such as fuel cells, storages, and CO2 reduction devices.[172-174]

Appendix 1. Permission and Rights

ELSEVIER LICENSE
TERMS AND CONDITIONS

Sep 25, 2017

This Agreement between Mr. Yuljae Cho ("You") and Elsevier ("Elsevier") consists of your license details and the terms and conditions provided by Elsevier and Copyright Clearance Center.

License Number	4195971017325
License date	Sep 25, 2017
Licensed Content Publisher	Elsevier
Licensed Content Publication	Nano Energy
Licensed Content Title	Enhanced energy harvesting based on surface morphology engineering of P(VDF-TrFE) film
Licensed Content Author	Yuljae Cho,Jong Bae Park,Byung-Sung Kim,Juwon Lee,Woong-Ki Hong,Il-Kyu Park,Jae Eun Jang,Jung Inn Sohn,SeungNam Cha,Jong Min Kim
Licensed Content Date	Sep 1, 2015
Licensed Content Volume	16
Licensed Content Issue	n/a
Licensed Content Pages	9
Start Page	524
End Page	532
Type of Use	reuse in a thesis/dissertation
Intended publisher of new work	other
Portion	full article
Format	electronic
Are you the author of this Elsevier article?	Yes
Will you be translating?	No
Title of your thesis/dissertation	Hybrid energy harvesting towards a sustainable energy system
Expected completion date	Oct 2017
Estimated size (number of pages)	200
Requestor Location	Mr. Yuljae Cho Exeter college, Turl street Oxford, OX1 3DP United Kingdom Attn: Mr. Yuljae Cho
Publisher Tax ID	GB 494 6272 12
Total	0.00 GBP
Terms and Conditions	

INTRODUCTION

1. The publisher for this copyrighted material is Elsevier. By clicking "accept" in connection with completing this licensing transaction, you agree that the following terms and conditions

JOHN WILEY AND SONS LICENSE TERMS AND CONDITIONS

Sep 25, 2017

This Agreement between Mr. Yuljae Cho ("You") and John Wiley and Sons ("John Wiley and Sons") consists of your license details and the terms and conditions provided by John Wiley and Sons and Copyright Clearance Center.

License Number	4195970905292
License date	Sep 25, 2017
Licensed Content Publisher	John Wiley and Sons
Licensed Content Publication	Advanced Electronic Materials
Licensed Content Title	Enhanced Ferroelectric Property of P(VDF-TrFE-CTFE) Film Using Room-Temperature Crystallization for High-Performance Ferroelectric Device Applications
Licensed Content Author	Yuljae Cho,Docheon Ahn,Jong Bae Park,Sangyeon Pak,Sanghyo Lee,Byoung Ok Jun,John Hong,Su Yong Lee,Jae Eun Jang,Jinpyo Hong,Stephen M. Morris,Jung Inn Sohn,Seung Nam Cha,Jong Min Kim
Licensed Content Date	Aug 11, 2016
Licensed Content Pages	1
Type of use	Dissertation/Thesis
Requestor type	Author of this Wiley article
Format	Electronic
Portion	Full article
Will you be translating?	No
Title of your thesis / dissertation	Hybrid energy harvesting towards a sustainable energy system
Expected completion date	Oct 2017
Expected size (number of pages)	200
Requestor Location	Mr. Yuljae Cho Exeter college, Turl street Oxford, OX1 3DP United Kingdom Attn: Mr. Yuljae Cho
Publisher Tax ID	EU826007151
Billing Type	Invoice
Billing Address	Mr. Yuljae Cho Exeter college, Turl street Oxford, United Kingdom OX1 3DP Attn: Mr. Yuljae Cho
Total	0.00 GBP
Terms and Conditions	

TERMS AND CONDITIONS

This copyrighted material is owned by or exclusively licensed to John Wiley & Sons, Inc. or one of its group companies (each a"Wiley Company") or handled on behalf of a society with

JOHN WILEY AND SONS LICENSE TERMS AND CONDITIONS

Sep 25, 2017

This Agreement between Mr. Yuljae Cho ("You") and John Wiley and Sons ("John Wiley and Sons") consists of your license details and the terms and conditions provided by John Wiley and Sons and Copyright Clearance Center.

License Number	4195970800091
License date	Sep 25, 2017
Licensed Content Publisher	John Wiley and Sons
Licensed Content Publication	Advanced Energy Materials
Licensed Content Title	Charge Transport Modulation of a Flexible Quantum Dot Solar Cell Using a Piezoelectric Effect
Licensed Content Author	Yuljae Cho,Paul Giraud,Bo Hou,Young-Woo Lee,John Hong,Sanghyo Lee,Sangyeon Pak,Juwon Lee,Jae Eun Jang,Stephen M. Morris,Jung Inn Sohn,SeungNam Cha,Jong Min Kim
Licensed Content Date	Sep 22, 2017
Licensed Content Pages	1
Type of use	Dissertation/Thesis
Requestor type	Author of this Wiley article
Format	Electronic
Portion	Full article
Will you be translating?	No
Title of your thesis / dissertation	Hybrid energy harvesting towards a sustainable energy system
Expected completion date	Oct 2017
Expected size (number of pages)	200
Requestor Location	Mr. Yuljae Cho Exeter college, Turl street Oxford, OX1 3DP United Kingdom Attn: Mr. Yuljae Cho
Publisher Tax ID	EU826007151
Billing Type	Invoice
Billing Address	Mr. Yuljae Cho Exeter college, Turl street Oxford, United Kingdom OX1 3DP Attn: Mr. Yuljae Cho
Total	0.00 GBP
Terms and Conditions	

TERMS AND CONDITIONS

This copyrighted material is owned by or exclusively licensed to John Wiley & Sons, Inc. or one of its group companies (each a"Wiley Company") or handled on behalf of a society with which a Wiley Company has exclusive publishing rights in relation to a particular work (collectively "WILEY"). By clicking "accept" in connection with completing this licensing

Bibliography

[1] Weiss, P. S. A conversation with prof. Zhong Lin Wang, energy harvester. *ACS Nano* **9**, 2221-2226 (2015).

[2] http://www.iop.org/resources/energy/index.html

[3] Jean, J., Brown, P. R., Jaffe, R. L., Buonassisi, T. & Bulović, V. Pathways for solar photovoltaics. *Energy Environ. Sci.* **8**, 1200-1219 (2015).

[4] Wang, Z. L. New wave power. *Nature*, **542**, 159-160 (2017).

[5] Wang, Z. L., Jiang, T. & Xu, L. Toward the blue energy dream by triboelectric nanogenerator networks. *Nano Energy* **39**, 9-23 (2017).

[6] Polman, A., Knight, M., Garnett, E. C., Ehrler, B. & Sinke, W. C. Photovoltaic materials: Present efficiencies and future challenges. *Science* **352**, aad4424 (2016).

[7] Lewis, N. S. Research opportunities to advance solar energy utilization. *Science* **351**, aad1920 (2016).

[8] Graetzel, M., Janssen, R. A., Mitzi, D. B. & Sargent, E. H. Materials interface engineering for solution-processed photovoltaics. *Nature* **488**, 304 (2012).

[9] Chu, S., Cui, Y. & Liu, N. The path towards sustainable energy. *Nat. Mater.* **16**, 16-22 (2017).

[10] Chu, S. & Majumdar, A. Opportunities and challenges for a sustainable energy future. *Nature* **488**, 294 (2012).

[11] Lee, R. The outlook for population growth. *Science* **333**, 569-573 (2011).

[12] Climatewire, J. Soaring electricity use by new electronic devices imperils climate change efforts. *The New York Times*.

[13] Chow, J., Kopp, R. J. & Portney, P. R. Energy resources and global development. *Science* **302**, 1528-1531 (2003).

[14] http://www.bbc.co.uk/news/world-asia-china-39971667

[15] https://www.bp.com/en/global/corporate/energy-economics/statistical-review-of-world-energy/primary-energy.html

[16] http://www.ren21.net/wp-content/uploads/2017/06/GSR2017_Highlights_FINAL.pdf

[17] Roemmich, D. *et al*. Unabated planetary warming and its ocean structure since 2006. *Nat. Clim. Change* **5**, 240-245 (2015).

[18] Rogelj, J. *et al*. Paris Agreement climate proposals need a boost to keep warming well below 2 ºC. *Nature* **534**, 631-639 (2016).

[19] Wang, Z. L. & Wu, W. Nanotechnology-enabled energy harvesting for self-powered micro-/nanosystems. *Angew. Chem. Int. Ed.* **51**, 11700-11721 (2012).

[20] https://en.wikipedia.org/wiki/Timeline_of_solar_cells

[21] https://energy.gov/articles/top-6-things-you-didnt-know-about-solar-energy

[22] https://sos.noaa.gov/datasets/energy-on-a-sphere/

[23] Parida, B., Iniyan, S. & Goic, R. A review of solar photovoltaic technologies. *Renew. Sustainable Energy Rev.* **15**, 1625-1636 (2011).

[24] Lee, J. *et al*. All-in-one energy harvesting and storage devices. *J. Mater. Chem. A* **4**, 7983-7999 (2016).

[25] Zheng, C. & Kammen, D. M. An innovation-focused roadmap for a sustainable global photovoltaic industry. *Energy Policy* **67**, 159-169 (2014).

[26] Yang, W. S. *et al*. Iodide management in formamidinium-lead-halide-based perovskite layers for efficient solar cells. *Science* **356**, 1376-1379 (2017).

[27] https://www.nrel.gov/pv/assets/images/efficiency-chart.png

[28] Cutting, C. L., Bag, M. & Venkataraman, D. Indoor light recycling: a new home for organic photovoltaics. *J. Mater. Chem. C* **4**, 10367-10370 (2016).

[29] Freitag, M. *et al*. Dye-sensitized solar cells for efficient power generation under ambient lighting. *Nat. Photon.* **11**, 372-378 (2017).

[30] Li, W. *et al*. Nanogenerator-based dual-functional and self-powered thin patch loudspeaker or microphone for flexible electronics. *Nat. Commun.* **8**, 15310 (2017).

[31] Wang, J. *et al*. Sustainably powering wearable electronics solely by biomechanical energy. *Nat. Commun.* **7**, 12744 (2016).

[32] Chen, J. *et al*. Micro-cable structured textile for simultaneously harvesting solar and mechanical energy. *Nat. Energy* **1**, 16138 (2016).

[33] Song, K. *et al*. Subdermal flexible solar cell arrays for powering medical electronic implants. *Adv. healthcare Mater.* **5**, 1572-1580 (2016).

[34] Tang, W. *et al*. Liquid-Metal Electrode for High-Performance Triboelectric Nanogenerator at an Instantaneous Energy Conversion Efficiency of 70.6%. *Adv. Funct. Mater.* **25**, 3718-3725 (2015).

[35] Zi, Y. et al. Effective energy storage from a triboelectric nanogenerator. *Nat. Commun.* **7**, 10987 (2016).

[36] Niu, S., Wang, X., Yi, F., Zhou, Y. S. & Wang, Z. L. A universal self-charging system driven by random biomechanical energy for sustainable operation of mobile electronics. *Nat. Commun.* **6**, 8975 (2015).

[37] Guo, H. et al. All-in-one shape-adaptive self-charging power package for wearable electronics. *ACS Nano* **10**, 10580-10588 (2016).

[38] Zhang, B. et al. Rotating-Disk-Based Hybridized Electromagnetic–Triboelectric Nanogenerator for Sustainably Powering Wireless Traffic Volume Sensors. *ACS Nano* **10**, 6241-6247 (2016).

[39] Lee, M., Yang, R., Li, C. & Wang, Z. L. Nanowire− Quantum Dot Hybridized Cell for Harvesting Sound and Solar Energies. *J. Phys. Chem. Lett.* **1**, 2929-2935 (2010).

[40] Yang, Y. *et al*. Silicon-based hybrid energy cell for self-powered electrodegradation and personal electronics. *ACS Nano* **7**, 2808-2813 (2013).

[41] Lee, J. *et al*. Highly stretchable piezoelectric-pyroelectric hybrid nanogenerator. *Adv. Mater.* **26**, 765-769 (2014).

[42] Lee, S. *et al*. Flexible hybrid cell for simultaneously harvesting thermal and mechanical energies. *Nano Energy* **2**, 817-825 (2013).

[43] Xue, X., Wang, S., Guo, W., Zhang, Y. & Wang, Z. L. Hybridizing energy conversion and storage in a mechanical-to-electrochemical process for self-charging power cell. *Nano lett.* **12**, 5048-5054 (2012).

[44] Song, R. *et al*. A rectification-free piezo-supercapacitor with a polyvinylidene fluoride separator and functionalized carbon cloth electrodes. *J. Mater. Chem. A* **3**, 14963-14970 (2015).

[45] Chodos, A. April 25, 1954: Bell Labs Demonstrates the First Practical Silicon Solar Cell. *APS News-This month in Physics history* (2009).

[46] Chapin, D. M., Fuller, C. & Pearson, G. A new silicon p-n junction photocell for converting solar radiation into electrical power. *J. Appl. Phys.* **25**, 676-677 (1954).

[47] Dimitrijev, S. in *Principles of semiconductor devices* (Oxford university press New York, 2012).

[48] Luque, A. & Hegedus, S. in *Handbook of photovoltaic science and engineering* (John Wiley & Sons, 2011).

[49] Carey, G. H. *et al*. Colloidal quantum dot solar cells. *Chem. Rev.* **115**, 12732-12763 (2015).

[50] Konstantatos, G. & Sargent, E. H. in *Colloidal quantum dot optoelectronics and photovoltaics* (Cambridge University Press, 2013).

[51] Lee, J. *et al*. Quantum-dot-sensitized solar cell with unprecedentedly high photocurrent. *Sci. Rep.* **3**, 1050 (2013).

[52] Hou, B. *et al*. Highly monodispersed PbS quantum dots for outstanding cascaded-junction solar cells. *ACS Energy Lett.* **1**, 834-839 (2016).

[53] Beard, M. C. Multiple exciton generation in semiconductor quantum dots. J. *Phys. Chem. Lett.* **2**, 1282-1288 (2011).

[54] Nozik, A. J. Multiple exciton generation in semiconductor quantum dots. *Chem. Phys. Lett.* **457**, 3-11 (2008).

[55] Yoon, W. *et al*. Enhanced open-circuit voltage of PbS nanocrystal quantum dot solar cells. *Sci. Rep.* **3**, 2225 (2013).

[56] Debnath, R., Bakr, O. & Sargent, E. H. Solution-processed colloidal quantum dot photovoltaics: A perspective. *Energy Environ. Sci.* **4**, 4870-4881 (2011).

[57] Pattantyus-Abraham, A. G. *et al*. Depleted-heterojunction colloidal quantum dot solar cells. *ACS Nano* **4**, 3374-3380 (2010).

[58] Lan, X. *et al*. Passivation using molecular halides increases quantum dot solar cell performance. *Adv. Mater.* **28**, 299-304 (2016).

[59] Lan, X. *et al*. 10.6% certified colloidal quantum dot solar cells via solvent-polarity-engineered halide passivation. *Nano Lett.* **16**, 4630-4634 (2016).

[60] McDonald, S. A. *et al*. Solution-processed PbS quantum dot infrared photodetectors and photovoltaics. *Nat. Mater*. **4**, 138 (2005).

[61] Sargent, E. H. Infrared photovoltaics made by solution processing. *Nat. Photon.* **3**, 325-331 (2009).

[62] Liu, M. *et al*. Hybrid organic–inorganic inks flatten the energy landscape in colloidal quantum dot solids. *Nat. Mater.* 16, 258-263 (2017).

[63] Shockley, W. & Queisser, H. J. Detailed balance limit of efficiency of p-n junction solar cells. *J. Appl. Phys.* **32**, 510-519 (1961).

[64] Kim, M. R. & Ma, D. Quantum-dot-based solar cells: recent advances, strategies, and challenges. J. *Phys. Chem. Lett.* **6**, 85-99 (2014).

[65] Tang, J. *et al*. Schottky quantum dot solar cells stable in air under solar illumination. *Adv. Mater.* **22**, 1398-1402 (2010).

[66] Tang, J. *et al*. Quantum junction solar cells. *Nano Lett.* **12**, 4889-4894 (2012).

[67] Chuang, C. H., Brown, P. R., Bulovic, V. & Bawendi, M. G. Improved performance and stability in quantum dot solar cells through band alignment engineering. *Nat. Mater.* **13**, 796-801 (2014).

[68] Lan, X., Masala, S. & Sargent, E. H. Charge-extraction strategies for colloidal quantum dot photovoltaics. *Nat. Mater.* **13**, 233 (2014).

[69] Kim, J. Y., Voznyy, O., Zhitomirsky, D. & Sargent, E. H. 25th Anniversary Article: Colloidal Quantum Dot Materials and Devices: A Quarter-Century of Advances. *Adv. Mater.* **25**, 4986-5010 (2013).

[70] Cao, Y., Stavrinadis, A., Lasanta, T., So, D. & Konstantatos, G. The role of surface passivation for efficient and photostable PbS quantum dot solar cells. *Nat. Energy* **1**, 16035 (2016).

[71] Michalet, X. *et al*. Quantum dots for live cells, in vivo imaging, and diagnostics. *Science* **307**, 538-544 (2005).

[72] Hou, B. *et al*. Red green blue emissive lead sulfide quantum dots: heterogeneous synthesis and applications. *J. Mater. Chem. C* **5**, 3692-3698 (2017).

[73] Madelung, O., Rössler, U. & Schulz, M. Non-Tetrahedrally Bonded Elements and Binary Compounds I, Springer, Berlin, Heidelberg, 1998.

[74] Kim, G. *et al*. High-efficiency colloidal quantum dot photovoltaics via robust self-assembled monolayers. *Nano Lett.* **15**, 7691-7696 (2015).

[75] Feng, W. *et al*. A layer-nanostructured assembly of PbS quantum dot/multiwalled carbon nanotube for a high-performance photoswitch. *Sci. Rep.* **4**, 3777 (2014).

[76] Tang, J. *et al.* Colloidal-quantum-dot photovoltaics using atomic-ligand passivation. *Nat. Mater.* **10**, 765-771 (2011).

[77] Kagan, C. R. *et al.* Charge transport in strongly coupled quantum dot solids. *Nat. Nanotechnol.* **10**, 1013-1026 (2015).

[78] Palmstrom, A. F. *et al.* Atomic layer deposition in nanostructured photovoltaics: tuning optical, electronic and surface properties. *Nanoscale* **7**, 12266-12283 (2015).

[79] Smith, B. B. *et al.* Theoretical studies of electronic state localization and wormholes in silicon quantum dot arrays. *Nano Lett.* **1**, 36-41 (2001).

[80] Mentzel, T. S. *et al.* Charge transport in PbSe nanocrystal arrays. *Phys. Rev. B* **77**, 075316 (2008).

[81] Sanchez, R. S. *et al*. Tunable light emission by exciplex state formation between hybrid halide perovskite and core/shell quantum dots: Implications in advanced LEDs and photovoltaics. *Sci. Adv.* **2**, e1501104 (2016).

[82] Moroz, P. *et al*. Suppressed carrier scattering in CdS-encapsulated PbS nanocrystal films. *ACS Nano* **7**, 6964-6977 (2013).

[83] Guo, X. *et al*. Polymer solar cells with enhanced fill factors. *Nat. Photon.* **7**, 825-833 (2013).

[84] Aqoma, H. *et al*. High-Efficiency Photovoltaic Devices using Trap-Controlled Quantum-Dot Ink prepared via Phase-Transfer Exchange. *Adv. Mater.* **29**, 1605756 (2017).

[85] Hong, J. *et al*. Enhanced charge carrier transport properties in colloidal quantum dot solar cells via organic and inorganic hybrid surface passivation. *J. Mater. Chem. A* **4**, 18769-18775 (2016).

[86] Kim, B. *et al*. High performance PbS quantum dot/graphene hybrid solar cell with efficient charge extraction. *ACS Appl. Mater. interfaces* **8**, 13902-13908 (2016).

[87] Diroll, B. T. *et al.* Spectrally-resolved dielectric functions of solution-cast quantum dot thin films. *Chem. Mater.* **27**, 6463-6469 (2015).

[88] Zhang, X. *et al.* Reduction of charge recombination in PbS colloidal quantum dot solar cells at the quantum dot/ZnO interface by inserting a MgZnO buffer layer. *J. Mater. Chem. A* **5**, 303-310 (2017).

[89] Kim, G. H. et al. Synergistic photocurrent addition in hybrid quantum dot: Bulk heterojunction solar cells. *Nano Energy* **13**, 491-499 (2015).

[90] Tang, J. & Sargent, E. H. Infrared colloidal quantum dots for photovoltaics: fundamentals and recent progress. *Adv. Mater.* **23**, 12-29 (2011).

[91] Yang, Z. *et al*. Colloidal quantum dot photovoltaics enhanced by perovskite shelling. *Nano Lett.* **15**, 7539-7543 (2015).

[92] Salmi, T., Bouzguenda, M., Gastli, A. & Masmoudi, A. Matlab/simulink based modeling of photovoltaic cell. *International Journal of Renewable Energy Research (IJRER)* **2**, 213-218 (2012).

[93] Tsai, H., Tu, C. & Su, Y. *Development of generalized photovoltaic model using MATLAB/SIMULINK* (Proceedings of the world congress on Engineering and computer science Ser. 2008, San Francisco, USA, 2008).

[94] Wang, Z. L. & Song, J. Piezoelectric nanogenerators based on zinc oxide nanowire arrays. *Science* **312**, 242-246 (2006).

[95] Wang, X., Song, J., Liu, J. & Wang, Z. L. Direct-current nanogenerator driven by ultrasonic waves. *Science* **316**, 102-105 (2007).

[96] Sohn, J. I. *et al*. Engineering of efficiency limiting free carriers and an interfacial energy barrier for an enhancing piezoelectric generation. *Energy Environ. Sci.* **6**, 97-104 (2013).

[97] Cha, S. *et al*. Porous PVDF as effective sonic wave driven nanogenerators. *Nano Lett.* **11**, 5142-5147 (2011).

[98] Agrawal, R., Peng, B. & Espinosa, H. D. Experimental-computational investigation of ZnO nanowires strength and fracture. *Nano Lett.* **9**, 4177-4183 (2009).

[99] Ni, H. & Li, X. Young's modulus of ZnO nanobelts measured using atomic force microscopy and nanoindentation techniques. *Nanotechnology* **17**, 3591 (2006).

[100] Zhu, G. *et al*. Toward large-scale energy harvesting by a nanoparticle-enhanced triboelectric nanogenerator. *Nano Lett.* **13**, 847-853 (2013).

[101] Lee, J. *et al*. Highly stretchable piezoelectric-pyroelectric hybrid nanogenerator. *Adv. Mater.* **26**, 765-769 (2014).

[102] Zhu, G. *et al*. A Shape-Adaptive Thin-Film-Based Approach for 50% High-Efficiency Energy Generation Through Micro-Grating Sliding Electrification. *Adv. Mater.* **26**, 3788-3796 (2014).

[103] Dagdeviren, C. *et al*. Conformal piezoelectric energy harvesting and storage from motions of the heart, lung, and diaphragm. *Proc. Natl. Acad. Sci. U. S. A.* **111**, 1927-1932 (2014).

[104] Zheng, Q. *et al*. In Vivo Powering of Pacemaker by Breathing-Driven Implanted Triboelectric Nanogenerator. *Adv. Mater.* **26**, 5851-5856 (2014).

[105] Tang, W. *et al*. Implantable self-powered low-level laser cure system for mouse embryonic osteoblasts' proliferation and differentiation. *ACS Nano* **9**, 7867-7873 (2015).

[106] Zheng, Q. *et al*. In vivo self-powered wireless cardiac monitoring via implantable triboelectric nanogenerator. *ACS Nano* **10**, 6510-6518 (2016).

[107] Hasegawa, R., Takahashi, Y., Chatani, Y. & Tadokoro, H. Crystal structures of three crystalline forms of poly (vinylidene fluoride). *Polym. J.* **3**, 600-610 (1972).

[108] Bachmann, M. & Lando, J. A reexamination of the crystal structure of phase II of poly (vinylidene fluoride). *Macromolecules* **14**, 40-46 (1981).

[109] Nalwa, H. S. in *Ferroelectric polymers: chemistry: physics, and applications* (CRC Press, 1995).

[110] Lovinger, A. J. Ferroelectric polymers. *Science* **220**, 1115-1121 (1983).

[111] Li, M. *et al*. Revisiting the δ-phase of poly (vinylidene fluoride) for solution-processed ferroelectric thin films. *Nat. Mater.* **12**, 433 (2013).

[112] Xia, F. *et al*. High electromechanical responses in a poly (vinylidene fluoride–trifluoroethylene–chlorofluoroethylene) terpolymer. *Adv. Mater.* **14**, 1574-1577 (2002).

[113] Hwang, S. K. *et al*. High Performance Multi-Level Non-Volatile Polymer Memory with Solution-Blended Ferroelectric Polymer/High-k Insulators for Low Voltage Operation. *Adv. Funct. Mater.* **23**, 5484-5493 (2013).

[114] DefaÿE. in *Integration of ferroelectric and piezoelectric thin films: concepts and applications for microsystems* (John Wiley & Sons, 2013).

[115] Furukawa, T. Ferroelectric properties of vinylidene fluoride copolymers. *Phase Transit.* **18**, 143-211 (1989).

[116] Mandal, D. Ultra-thin films of a ferroelectric copolymer: P (VDF-TrFE). *Master of Science in Physics, Fakultät für Mathematik, Naturwissenschaften und Informatik, Brandenburgische Technische Universität Cottbus, Germany* (2008).

[117] Ramadan, K. S., Sameoto, D. & Evoy, S. A review of piezoelectric polymers as functional materials for electromechanical transducers. *Smart Mater. Struct.* **23**, 033001 (2014).

[118] Bowen, C., Kim, H., Weaver, P. & Dunn, S. Piezoelectric and ferroelectric materials and structures for energy harvesting applications. *Energy Environm. Sci.* **7**, 25-44 (2014).

[119] Jean-Mistral, C., Basrour, S. & Chaillout, J. Comparison of electroactive polymers for energy scavenging applications. *Smart Mater. Struct.* **19**, 085012 (2010).

[120] Harrison, J. & Ounaies, Z. in *Piezoelectric polymers* (Wiley Online Library, 2002).

[121] Li, C. *et al*. Flexible dome and bump shape piezoelectric tactile sensors using PVDF-TrFE copolymer. *J. Microelectromech. Syst.* **17**, 334-341 (2008).

[122] Sharma, T., Je, S., Gill, B. & Zhang, J. X. Patterning piezoelectric thin film PVDF–TrFE based pressure sensor for catheter application. *Sens. Actuators A Phys.* **177**, 87-92 (2012).

[123] Lines, M. E. & Glass, A. M. in *Principles and applications of ferroelectrics and related materials* (Oxford university press, 1977).

[124] Ni, G. *et al*. Graphene–ferroelectric hybrid structure for flexible transparent electrodes. *ACS Nano* **6**, 3935-3942 (2012).

[125] Wang, X., Yang, B., Liu, J. & Yang, C. A transparent and biocompatible single-friction-surface triboelectric and piezoelectric generator and body movement sensor. *J. Mater. Chem. A* **5**, 1176-1183 (2017).

[126] Xia, W. *et al*. A crystal phase transition and its effect on the dielectric properties of a hydrogenated P (VDF-co-TrFE) with low TrFE molar content. *RSC Adv.* **5**, 107557-107565 (2015).

[127] Feng, T. *et al*. Temperature Control of P (VDF-TrFE) Copolymer Thin Films. *Integrated Ferroelectr.* **141**, 187-194 (2013).

[128] Li, W., Jiang, L., Zhu, Y. & Wang, J. Structure of P (VDF-TrFE)(80/20) copolymers under electron irradiation and recrystallization. *J. Appl. Polym. Sci.* **102**, 4258-4263 (2006).

[129] Duan, C. *et al*. Simulations of ferroelectric polymer film polarization: The role of dipole interactions. *Phys. Rev. B* **69**, 235106 (2004).

[130] Choi, J. *et al*. Photoemission band symmetries and dipole active modes of crystalline films of vinylidene fluoride (70%) with trifluoroethylene (30%) across the ferroelectric transition (s). *J. Phys. Condens. Mat.* **12**, 4735 (2000).

[131] Lallart, M., Ferroelectrics-Physical Effects. *INTECH* (2011).

[132] David J. Griffiths-Introduction to Electrodynamics-Prentice-Hall (1999)

[133] Lu, Y., Claude, J., Neese, B., Zhang, Q. & Wang, Q. A modular approach to ferroelectric polymers with chemically tunable curie temperatures and dielectric constants. *J. Am. Chem. Soc.* **128**, 8120-8121 (2006).

[134] Smith, O. L. *et al*. Enhanced permittivity and energy density in neat poly (vinylidene fluoride-trifluoroethylene-chlorotrifluoroethylene) terpolymer films through control of morphology. *ACS Appl. Mater. Interfaces* **6**, 9584-9589 (2014).

[135] Li, H., Tan, K., Hao, Z. & He, G. Preparation and crystallization behavior of poly (vinylidene fluoride-ter-chlorotrifluoroethylene-ter-trifluoroethylene). *J. Appl. Polym. Sci.* **122**, 3007-3015 (2011).

[136] Gong, H., Miao, B., Zhang, X., Lu, J. & Zhang, Z. High-field antiferroelectric-like behavior in uniaxially stretched poly (vinylidene fluoride-trifluoroethylene-chlorotrifluoroethylene)-grafted-poly (methyl methacrylate) films with high energy density. *RSC Adv.* **6**, 1589-1599 (2016).

[137] Li, Z., Wang, J., Wang, X., Yang, Q. & Zhang, Z. Ferro-and piezo-electric properties of a poly (vinyl fluoride) film with high ferro-to para-electric phase transition temperature. *RSC Adv.* **5**, 80950-80955 (2015).

[138] Klein, R. J., Xia, F., Zhang, Q. & Bauer, F. Influence of composition on relaxor ferroelectric and electromechanical properties of poly (vinylidene fluoride-trifluoroethylene-chlorofluoroethylene). *J. Appl. Phys.* **97**, 094105 (2005).

[139] Kim, J. *et al*. High-Performance Piezoelectric, Pyroelectric, and Triboelectric Nanogenerators Based on P (VDF-TrFE) with Controlled Crystallinity and Dipole Alignment. *Adv. Funct. Mater.* **27**, 1700702 (2017).

[140] Park, C., Ounaies, Z., Wise, K. E. & Harrison, J. S. In situ poling and imidization of amorphous piezoelectric polyimides. *Polymer* **45**, 5417-5425 (2004).

[141] Lee, J. *et al*. Control of skin potential by triboelectrification with ferroelectric polymers. *Adv. Mater.* **27**, 5553-5558 (2015).

[142] Li, B., Xu, C., Zhang, F., Zheng, J. & Xu, C. Self-polarized piezoelectric thin films: preparation, formation mechanism and application. *J. Mater. Chem. C* **3**, 8926-8931 (2015).

[143] Maji, S. *et al*. Self-oriented β-crystalline phase in the polyvinylidene fluoride ferroelectric and piezo-sensitive ultrathin Langmuir–Schaefer film. *Phys. Chem. Chem. Phys.* **17**, 8159-8165 (2015).

[144] Hwang, G. W. *et al*. Identifying and Eliminating Emissive Sub-bandgap States in Thin Films of PbS Nanocrystals. *Adv. Mater.* **27**, 4481-4486 (2015).

[145] Chuang, C. M. *et al*. Open-circuit voltage deficit, radiative sub-bandgap states, and prospects in quantum dot solar cells. *Nano Lett.* **15**, 3286-3294 (2015).

[146] Azmi, R., Oh, S. & Jang, S. High-efficiency colloidal quantum dot photovoltaic devices using chemically modified heterojunctions. *ACS Energy Lett.* **1**, 100-106 (2016).

[146] Wu, W. *et al*. Piezophototronic Effect in Single-Atomic-Layer MoS2 for Strain-Gated Flexible Optoelectronics. *Adv. Mater.* **28**, 8463-8468 (2016).

[147] Würfel, U. *et al*. How Molecules with Dipole Moments Enhance the Selectivity of Electrodes in Organic Solar Cells–A Combined Experimental and Theoretical Approach. *Adv. Energy Mater.* **6,** 1600594 (2016).

[148] Liu, S. *et al*. Strain modulation in graphene/ZnO nanorod film schottky junction for enhanced photosensing performance. *Adv. Funct. Mater.* **26**, 1347-1353 (2016).

[149] Liu, C. *et al*. Interface engineering on p-CuI/n-ZnO heterojunction for enhancing piezoelectric and piezo-phototronic performance. *Nano Energy* **26**, 417-424 (2016).

[150] Tarn, J. & Huang, L. Saint-Venant end effects in multilayered piezoelectric laminates. *Int. J. Solids Structures* **39**, 4979-4998 (2002).

[151] Omote, K., Ohigashi, H. & Koga, K. Temperature dependence of elastic, dielectric, and piezoelectric properties of "single crystalline''films of vinylidene fluoride trifluoroethylene copolymer. *J. Appl. Phys.* **81**, 2760-2769 (1997).

[152] Liu, M. *et al*. Double-sided junctions enable high-performance colloidal-quantum-dot photovoltaics. *Adv. Mater.* **28**, 4142-4148 (2016).

[153] Yuan, Y. *et al*. Efficiency enhancement in organic solar cells with ferroelectric polymers. *Nat. Mater.* **10**, 296-302 (2011).

[154] Nalwa, K. S. *et al*. Enhanced charge separation in organic photovoltaic films doped with ferroelectric dipoles. *Energy Environ. Sci.* **5**, 7042-7049 (2012).

[155] Zhao, D. *et al*. High-Efficiency Solution-Processed Planar Perovskite Solar Cells with a Polymer Hole Transport Layer. *Adv. Energy Mater.* **5,** 1401855 (2015).

[156] Aqoma, H. *et al*. Simultaneous Improvement of Charge Generation and Extraction in Colloidal Quantum Dot Photovoltaics Through Optical Management. *Adv. Funct. Mater.* **25**, 6241-6249 (2015).

[157] Bozyigit, D., Lin, W. M., Yazdani, N., Yarema, O. & Wood, V. A quantitative model for charge carrier transport, trapping and recombination in nanocrystal-based solar cells. *Nat. Commun.* **6**, 6180 (2015).

[158] Zi, Y. *et al*. Effective energy storage from a triboelectric nanogenerator. *Nat. Commun.* **7**, 10987 (2016).

[159] Niu, S., Wang, X., Yi, F., Zhou, Y. S. & Wang, Z. L. A universal self-charging system driven by random biomechanical energy for sustainable operation of mobile electronics. *Nat. Commun.* **6**, 8975 (2015).

[160] Zhang, B. et al. Rotating-Disk-Based Hybridized Electromagnetic–Triboelectric Nanogenerator for Sustainably Powering Wireless Traffic Volume Sensors. *ACS Nano* **10**, 6241-6247 (2016).

[161] Lee, Y. et al. Synergistic Effects of a Multifunctional Graphene Based Interlayer on Electrochemical Behavior and Structural Stability. *ACS Appl. Mater. Interfaces* **8**, 17651-17658 (2016).

[162] Nair, R. R. et al. Fine structure constant defines visual transparency of graphene. *Science* **320**, 1308 (2008)

[163] Cho, Y. *et al*. Enhanced Ferroelectric Property of P (VDF-TrFE-CTFE) Film Using Room-Temperature Crystallization for High-Performance Ferroelectric Device Applications. *Advanced Electronic Materials* **2**, 1600225 (2016).

[164] Cho, Y. *et al*. Enhanced energy harvesting based on surface morphology engineering of P (VDF-TrFE) film. *Nano Energy* **16**, 524-532 (2015).

[165] Li, X. *et al*. Large-area synthesis of high-quality and uniform graphene films on copper foils. *Science* **324**, 1312-1314 (2009).

[166] Nilsson, J. W. & Riedel, S. Electric circuits, vol. 8. (2009).

[167] Choi, J. *et al*. Chloride Passivation of ZnO Electrodes Improves Charge Extraction in Colloidal Quantum Dot Photovoltaics. *Adv. Mater.* **29**, 1702350 (2017).

[168] Ning, Z. *et al*. Quantum-dot-in-perovskite solids. *Nature* **523**, 324 (2015).

[169] Yan, Y. *et al*. Multiple exciton generation for photoelectrochemical hydrogen evolution reactions with quantum yields exceeding 100%. *Nat. Energy* **2**, 17052 (2017).

[170] Zhao, K., Yang, Y., Liu, X. & Wang, Z. L. Triboelectrification-Enabled Self-Charging Lithium-Ion Batteries. *Adv. Energy Mater.* DOI: 10.1002/aenm.201700103 (2017).

[171] Zheng, Q., Shi, B., Li, Z. & Wang, Z. L. Recent Progress on Piezoelectric and Triboelectric Energy Harvesters in Biomedical Systems. *Adv. Sci.* **4**, 1700029 (2017).

[172] Lee, K., Spendelow, J. S., Choe, Y., Fujimoto, C. & Kim, Y. S. An operationally flexible fuel cell based on quaternary ammonium-biphosphate ion pairs. *Nat. Energy* **1**, 16120 (2016).

[173] Choi, J. W. & Aurbach, D. Promise and reality of post-lithium-ion batteries with high energy densities. *Nat. Rev. Mater.* **1**, 16013 (2016).

[174] Liu, M. *et al*. Enhanced electrocatalytic CO2 reduction via field-induced reagent concentration. *Nature* **537**, 382-386 (2016).